Structural and functional characterization of the lysosomal amino acid transporter PQLC2

Layal Jamal

THESE DE DOCTORAT

NNT : 2024UPASL129

université PARIS-SACLAY

Structural and functional characterization of the lysosomal amino acid transporter PQLC2

Caractérisation structurelle et fonctionnelle du transporteur lysosomal d'acides aminés PQLC2

Thèse de doctorat de l'université Paris-Saclay

École doctorale n° 568 Signalisations et réseaux Intégratifs en biologie (Biosigne)
Spécialité de doctorat : Biologie moléculaire et cellulaire
Graduate School : Life Sciences and Health

Référent : Faculté de médecine

Thèse préparée dans la unité de recherche **Institut de Biologie Intégrative de la Cellule (I2BC) (Université Paris-Saclay, CEA, CNRS),** sous la direction de **José Luis VAZQUEZ-IBAR**, **Chargé de Recherche CNRS,**

Thèse soutenue à Paris-Saclay, le 16 décembre 2024, par

Layal JAMAL

Composition du Jury

Membres du jury avec voix délibérative

Agathe URVOAS Professeur Université, Université Paris-Saclay, Institut de Biologie Integrative de la Cellule UMR 9198	Présidente
Guillaume LEBON Chargé de Recherche CNRS, Université Montpellier, Institut de Génomique Fonctionnelle UMR 5203	Rapporteur & Examinateur
Ekaitz ERRASTI-MURUGARREN Assistant Professor, Université de Barcelona, Institut d'Investigació Biomèdica de Bellvitge	Rapporteur & Examinateur
Sophie COMBET PhD Directrice de Recherche, CEA/CNRS, Laboratoire Léon-Brillouin (LLB) UMR 12	Examinatrice

Acknowledgement

I would like to thank the Biosigne doctoral school for funding my thesis project, and the Proteins and Membrane Systems laboratory headed by Guillaume Lenoir and José Luis Vázquez-Ibar for hosting me in their laboratories over the past 3 years.

I would like to thank my thesis supervisor for the knowledge and expertise he generously shared with me during these years. Thank you for the open-mindedness that enabled me to experiment with new techniques and varied methods that enriched my skills. Thank you for your constant availability and presence during the various meetings and experiments.

I would like to express my deep gratitude to my monitoring committee: Marc Le Maire and Martin Picard for their ongoing support and valuable scientific and professional comments, which had a positive impact on my thesis project.

I would also like to thank the members of the jury for agreeing to act as examiner/rapporteur for my thesis, and for their presence at my defense.

I'm extremely grateful to Leandro Tabares for his advice and patience. Thank you for helping me to understand EPR and the various complicated approaches. Thank you for your time and availability, which enabled me to advance my research over the past year. Thank you for giving me the passion to learn more about biophysics.

I would also like to thank Sun Un for his valuable scientific comments during the meetings. Thank you for the positivity you spread in science.

I would like to thank our collaborator Bruno Gasnier for welcoming me to his laboratory (Laboratoire de Dynamique des Membranes at the Institut des Neurosciences Saints-Pères Paris, Université Paris Cité). I would also like to thank Claire Desnos, Corinne Sagné, Cécile Jouffret and Elodie Phommabouth for their generosity in welcoming me to their laboratory and providing me with all the necessary training.

I would also like to thank Laura Pieri and Ana Andreea Arteni, who helped me during my training in negative staining electron microscopy. Laura, thank you for your availability and your continuous help and encouragement during each session. Thank you for the skills you enabled me to acquire.

Special thanks go to our collaborators Igor Tascon Iban Ubarretxena from the BIOFISIKA Institute (UPV/EHU-CSIC) in the Basque country. Your feedbacks were extremely appreciated and invaluable for the progress of the project.

Words can't express my gratitude to my colleagues Philémon Von Gaudecker and Céline Ransy. Céline thank you for being a good role model in terms of discpline and responsibility especially for the lab security. Thank you for taking the time to look at my various drafts and giving me advice. Thank you for sharing your knowledge of Excel.

Thank you for encouraging me. Philemon, thank you for being a good friend. Thank you for discussing the various novels and comics we've read. Thank you for your passion and enthusiasm for research.

Special thanks to LPSM laboratory members Christine Jaxel, Thibaud Dieudonne, Véronica Beswick, Cédric Montigny and Guillaume Lenoir. Thank you for the laboratory meetings, for the various scientific feedbacks and for the end-of-year and birthday celebrations.

I would also like to thank Pascale Filoche, who was always available when I needed administrative documents and who kept our laboratory stock always filled.

Heitor Gobbi Sebinelli and Pauline Funke, thank you to be good friends. Heitor, it was great to share our thoughts on the football matches. Pauline, thank you for the home made deliciuous sweet you shared with me.

Not to forget our old colleagues and lab members that have impacted positively my journey, Kahina Slimani, Vignesh Diderot, Nesma Al Sayed and Axel Sidoli and Tiphene Frederico.

Finally, I would like to thank all my friends and family for supporting me over the past three years. I look forward to new challenges and new memories. I wish everyone I have mentioned or forgotten to mention all the best.

université PARIS-SACLAY

ÉCOLE DOCTORALE
Signalisation et réseaux intégratifs en biologie (BIOSIGNE)

Titre : Caractérisation structurelle et fonctionnelle du transporteur lysosomal d'acides aminés PQLC2

Mots clés : Protéine de transport membranaire - *Saccharomyces cerevisiae* - Membrane lysosomale - Signalisation mTORC1 - Mutation de consensus- Structure des protéines

Résumé : PQLC2, qui signifie protéine contenant des répétitions de boucle proline-glutamine 2, appartient à une famille de protéines de transport membranaires caractérisées par une topologie membranaire à sept hélices et deux motifs proline-glutamine. PQLC2 est localisé dans la membrane lysosomale des cellules mammifères, et des études utilisant du PQLC2 recombinant exprimé dans des ovocytes de *Xenopus* ont démontré que PQLC2 est un uniporteur qui transporte spécifiquement des acides aminés cationiques. Cependant, sa structure atomique en 3D n'a pas encore été déterminée. En plus de son rôle de transporteur, PQLC2 est également un récepteur membranaire. Lorsque la cellule est privée d'acides aminés cationiques, PQLC2 recrute à la surface du lysosome un complexe de trois protéines (appelé CSW) : les protéines GTPas-activatrices C9ORF72 et SMCR8, et WDR41, l'ancrage entre CSW et PQLC2. Le complexe CSW est important pour le bon fonctionnement des lysosomes. De plus, des mutations congénitales dans le gène codant pour C9ORF72 sont directement associées à deux maladies neurodégénératives.

Des essais de pull-down dans des extraits cellulaires indiquent que l'interaction d'un court motif peptidique de 10 acides aminés provenant d'une boucle saillante de WDR41 (boucle WDR41-7CD) avec PQLC2 est suffisante pour le recrutement lysosomique de CSW. Afin de caractériser cette interaction ainsi que le rôle fonctionnel de PQLC2, nous avons exprimé PQLC2 de mammifère dans la levure *Saccharomyces cerevisiae* et établi un protocole de purification de PQLC2 basé sur la reconnaissance entre des nanocorps anti-GFP et GFP fusionné à PQLC2. Pour améliorer la stabilité de PQLC2 purifié par détergent, nous avons introduit des mutations spécifiques le long de la séquence de la protéine en utilisant une approche de mutagenèse basée sur un consensus. La microscopie électronique à contraste négatif de PQLC2 purifié par détergent suggère que ce transporteur s'assemble sous forme d'homotrimère, comme les autres membres de la même famille de transporteurs à boucle PQ. Enfin, par spectroscopie de résonance paramagnétique électronique (RPE), nous avons évalué l'interaction directe entre PQLC2 et un peptide codant la boucle WDR41. Ces expériences ont révélé le rôle de certains résidus de la boucle WDR41 dans l'interaction PQLC2/boucle WDR41-7CD, ainsi que l'effet d'un substrat de PQLC2.

université PARIS-SACLAY

ÉCOLE DOCTORALE
Signalisation et réseaux intégratifs en biologie (BIOSIGNE)

Title : Structural and functional characterization of the lysosomal amino acid transporter PQLC2

Keywords : Membrane transport protein - *Saccharomyces cerevisiae* – Lysosomal membrane - mTORC1 signaling - Consensus mutation – Proteins structure

Abstract : PQLC2, which stands for proline-glutamine loop repeat-containing protein 2, belongs to a family of membrane transport proteins characterized by a seven-helix membrane topology and two proline-glutamine motifs. PQLC2 is localized in the lysosomal membrane of mammalian cells, and studies using recombinant PQLC2 expressed in *Xenopus* oocytes have demonstrated that PQLC2 is an uniporter that specifically transports cationic amino acids. However, its 3D atomic structure has not yet been determined. In addition to being a transporter, PQLC2 is also a membrane receptor. When the cell is deprived of cationic amino acids, PQLC2 recruits at the lysosome surface a complex of three proteins (called CSW): the GTPase-activating proteins C9ORF72 and SMCR8, and WDR41, the anchor between CSW and PQLC2. The CSW complex is important for normal lysosome function. In addition, congenital mutations in the gene encoding C9ORF72 are directly associated with two neurodegenerative diseases.

Pull-down assays in cell extracts indicate that the interaction of a short 10 amino acid peptide motif from a protruding loop of WDR41 (WDR41-7CD loop) with PQLC2 is sufficient for lysosomal recruitment of CSW. To characterize this interaction as well as the functional role of PQLC2, we expressed mammalian PQLC2 in the yeast *Saccharomyces cerevisiae*, and established a purification protocol of PQLC2 based on the recognition between anti-GFP nanobodies and GFP fused to PQLC2. To improve the stability of detergent-purified PQLC2, we introduced specific mutations along the protein sequence using a consensus-based mutagenesis approach. Negative-staining electron microscopy of detergent-purified PQLC2 suggests that this transporter assembles as a homotrimer, like other members of the same PQ-loop family of transporters. Finally, by electron paramagnetic resonance (EPR) spectroscopy, we assessed the direct interaction between PQLC2 and a peptide encoding the WDR41 loop. These experiments revealed the role of certain WDR41 loop residues in the PQLC2/WDR41-7CD loop interaction, as well as the effect of a PQLC2 substrate.

List of abbreviations

Ade : adenine

ADP : adenosine diphosphate

Arg : arginine

ALS : amyotrophic lateral sclerosis

Ampr : ampicillin

BCA : bicinchoninic acid

BSA : bovine serum albumin

CAN : CANavanine resistance

C9ORF72 : chromosome 9 open reading frame 72

CCD : charge coupled device

CHS : cholesteryl hemisuccinate

CSW : C9ORF72/SMCR8/WDR41

CTF : Contrast Transfer Function

kDa : kilodaltons

DDM : n-Dodecyl- β- maltopyranoside

DLS : Dynamic light scattering

DM : n-Decyl-β-D-maltopyranoside

DMSO : dimethyl sulphoxide

DNA : deoxyribonucleic acid

dNTP : deoxynucleoside triphosphates

DOPC : 1,2-Dioleoyl-sn-glycero-3-phosphocholine

DOPE : 1,2-dioleoyl-sn-glycero-3-phosphoethanolamine

DTE : dithioerythritol

DTT : dithiothreitol

EB : ethidium bromide

ECL : enhanced chemiluminescent

***E. coli* :** *Escherichia coli*

EDTA : ethylene diamine tetraacetic acid

FSEC : fluorescence-detection size-exclusion chromatography

FTD : frontotemporal dementia

GAL : GALactose metabolism

GAP : GTPase-activating proteins

GFP : green fluorescent protein

HEPES : N-(2-Hydroxyethyl) piperazine-N'-(2-ethanesulfonic acid)

HF : high fidility

His : histidine

HRP : horseradish peroxidase

Hrv : human rhinovirus

i.e : this means

IPTG : isopropyl β-D-1-thiogalactopyranoside

LAMPs : lysosomal-associated membrane proteins.

LB : Luria-Bertani broth

Leu : leucine

LMNG : lauryl maltose neopentyl glycol

Lys : lysine

µCi : microcurie

mTORC1 : mechanistic target of repamycin complex 1

MW : molecular weight

Nano-GFP : nanobodies targeting the GFP

NHS : N-hydroxysuccinimide

NMR : nuclear magnetic resonance

OD : optical density

ON : overnight

PAGE : polyacrylamide gel electrophoresis

PBS : phosphate-buffered saline

PCR : polymerase chain reaction

PEG : polyethylene glycol

Pi : inorganic phosphate

PIC : protease inhibitor cocktail

PIPES : 2,2'-(piperazine-1,4-diyl)bis(ethanesulfonic acid)

PL : proteoliposomes

PMSF : phenylmethylsulfonyl fluoride

PMT : photomultiplier tubes

PQLC2 : PQ-loop repeat containing protein 2

PES : polyethersulfone

PVDF : polyvinylidene difluoride

rpm : revolutions per minute

RT : room temperature

SAM : S-Adenosyl methionine

S. cerevisiae : *saccharomyces cerevisiae*

SDS : sodium dodecylsulfate

SLC38A9 : neutral amino acid transporter 9

SMCR8 : Smith–Magenis syndrome chromosomal region candidate gene 8

SNAREs : SNAP REceptors

SPH : sphingomyelin

SSD : salmon sperm DNA

Super Optimal Broth : SOB

TCEP : Tris(2-carboxyethyl)phosphine

TRP1 : TRyPtophan

2D : Two dimensions

2µ : 2-micrometer

Ura : uracil

V-ATPase : vacuolar-type ATPase

VHH : Variable Heavy domain of Heavy chain

WDR41 : WD repeat domain 41

WT : wild type

w/v : weight/volume

w/w : weight/weight

List of tables

List of figures

Table of contents

1 INTRODUCTION

1.1 PROPERTIES OF LYSOSOMES

Lysosomes were first discovered in 1955 during the study of insulin's mode of action, following the detection of a hydrolytic function in a biochemical fraction (De Duve, 2005). Subsequently, a series of studies identified the lysosome as a membrane-bound compartment dedicated to breakdown and recycling of complex cellular components (Klumperman & Raposo, 2014) (Farquhar et al., 1972). Lysosomes are present in all animal cells. Their size, shape and number vary according to species and cell type (Baba et al., 1994) (NOVIKOFF, A. et al., 1956). The main feature of the lysosome is its internal acidic pH (ranging from 4.5 to 5.5), optimal for the digestion role of luminal hydrolases (Mindell, 2012). This is is maintained thanks to the activity of the vacuolar-type proton pumping ATPase (V-ATPase) that pumps protons inside the lysosome against its gradient at the expenses of ATP hydrolysis (Forgac, 2007) (Ishida et al., 2013). This process builds a net positive charge inside the lumen of the lysosome that can be dissipated by K^+ efflux or Cl^- influx through ion channels and transporter (Mindell, 2012) (Lawrence & Zoncu, 2019) (**Figure 1**).

The primary cellular function of the lysosome is the degradation and recycling of macromolecules obtained by endocytosis, autophagy and other cellular trafficking pathways (Kaur & Debnath, 2015) (Sorkin & Von Zastrow, 2009) (Deretic & Levine, 2009). Damaged or misfolded proteins and other macromolecules like lipids, sugars or nucleotides from different cellular localization, including the plasma membrane, are transported to the lysosomal lumen, where they are digested (Conner & Schmid, 2003) (Di Fiore & Von Zastrow, 2014) (Kaur & Debnath, 2015). The final products of this digestion are transporter by lysosomal membrane transporters from the lumen to the cytosol, where they are reused in biosynthetic reactions (Gould & Lippincott-Schwartz, 2009) (Klumperman & Raposo, 2014) (Saftig & Klumperman, 2009). These functions underline the important role of lysosomes in maintaining normal cellular health (Platt,

2018) (Nixon, 2013) (Jeyakumar et al., 2005).

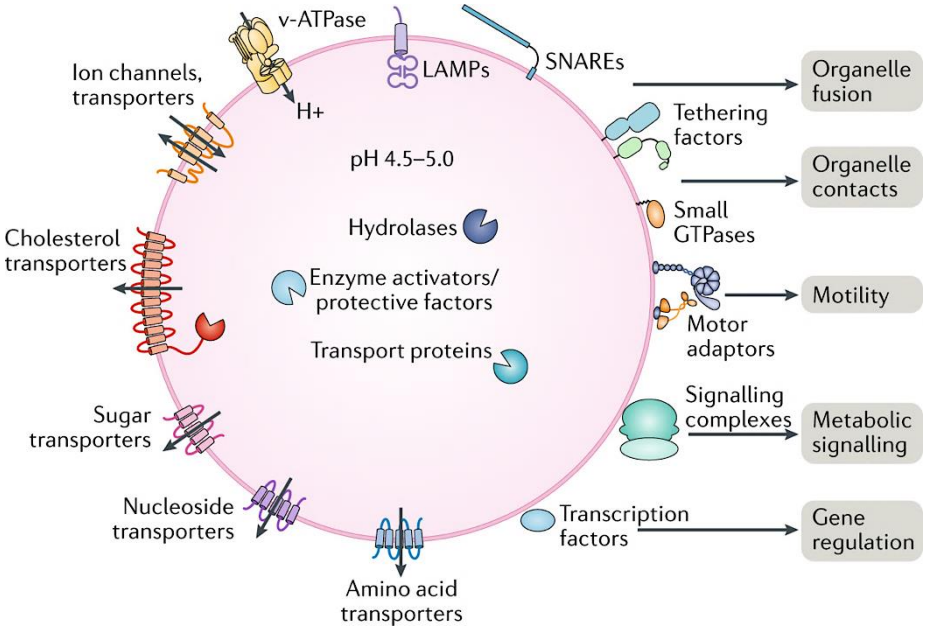

Figure 1. The lysosomal proteome. The lysosomal lumen has an acidic pH (between 4.5 and 5.5), which is maintained by the vacuolar-type ATPase (v-ATPase) pump and the K^+ efflux and/or Cl^- influx (Mindell, 2012). The lysosomal lumen contains hydrolases responsible for the degradation of various substrates, enzymatic activators and protective factors that contribute to degradation (Perera & Zoncu, 2016). The lysosomal membrane possesses a large battery of integral membrane proteins, including the v-type ATPase involved in lysosomal acidification, the lysosome-associated membrane proteins (LAMPs), different ion channels, and transporters of cholesterol, sugar and amino acids, and SNAP Receptors (SNAREs) that are involved in lysosome fusion with other organelles (Forgac, 2007). In addition, the cytosolic face of the lysosome plays important roles in different cellular functions throught association with proteins and protein complexes such as tethering factors, transcription factors, motor adapters and small GTPases (Saftig & Klumperman, 2009). Adapted from (Ballabio & Bonifacino, 2020).

To accomplish its different physiological roles, the lysosomal membrane includes the

highly glycosylated lysosome-associated membrane proteins (LAMPs) that protect the lysosomal membrane from degradation, ion channels that maintain ionic homeostasis, transporters of cholesterol and other lipids, solute transporters that carry sugars, nucleosides and amino acids, and SNAP receptors (SNARES) that mediate fusion of lysosomes with other organelles (Saftig & Klumperman, 2009).

In addition to their degradative and recycling role in autophagy, endocytosis and phagocytosis, new findings have demonstrated the role of the lysosome in cell signaling pathways mediated by the cytosolic region of the lysosome (Perera & Zoncu, 2016) (Chantranupong et al., 2015) (Settembre et al., 2012) (Sorkin & Von Zastrow, 2009). One of these pathways involves the multiple protein complex mTORC1 (mechanistic target of rapamycin complex 1), a critical controller in cellular growth, survival, metabolism, and development (Korolchuk et al., 2011). mTORC1 integrates signals such as cellular nutrient levels and triggers responses that stimulate anabolism or suppress catabolism (Aylett et al., 2016). The lysosomal membrane protein SNAT9/ SLC38A9 (neutral amino acid transporter 9) is able to sense the cell's amino acid content, leading to the recruitment and activation of mTORC1 at the lysosomal surface (Saxton & Sabatini, 2017) (Lei et al., 2021). SNAT9/ SLC38A9 has then a dual function as receptor and transporter, hence the term transceptor (Gasnier, 2021) (Rebsamen et al., 2015). (**Figure 2.** See next section).

Proteomic studies have identified 734 lysosomal membrane proteins, both lysosomal resident and proteins with secondary localization (Rudnik & Damme, 2021) (Della Valle et al., 2011) (Schröder et al., 2007) (Chapel et al., 2013). Among these 734 proteins, potential lysosomal transporters account for 46 proteins, including 27 plasma membrane proteins (Chapel et al., 2013), with potential roles on lysosomal-mediated cell signalling.

In summary, the lysosome is crucial for the digestion and recycling of macromolecules (Kaur & Debnath, 2015). However, it is also a signaling center, so any alteration in lysosomal function will almost likely lead to cellular damage (Jeyakumar et al., 2005)

(Nixon, 2013). Loss-of-function mutations in lysosomal transporters of lipids, amino acids and nucleotides are implicated in lysosomal storage diseases resulted from the accumulation of undigested or partially digested macromolecules in lysosomes (Platt et al., 2018) (Ballabio & Gieselmann, 2009). Furthermore, studies firmly establish the accumulation of autophagic substrates in lysosomal storage diseases, where they have also been found in common neurodegenerative diseases such as Alzheimer, Parkinson and Hungtinton (Ballabio & Gieselmann, 2009) (Rubinsztein, 2006).

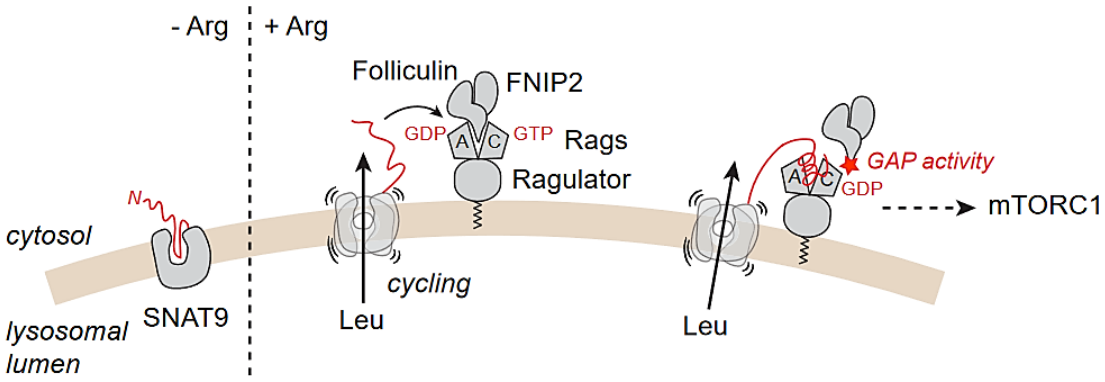

Figure 2. Amino acid sensing mechanism by the lysosomal membrane protein SNAT9 adapted from (Gasnier, 2021). SNAT9 detects intracellular lysosomal Arg (Jung et al., 2015). It exports Leu from the lysosomal lumen to the cytosol and activates heterodimeric Rag-GTPases, which are attached to the lysosomal membrane by Rags regulators. In their active form, Rag-GTPases recruit mTORC1 (Kim et al., 2008). N-terminal tale protruding from SNAT9 enables folliculin/FNIP2 detachment from Rag-GTPases, allowing them to be activated, and resulting in mTORC1 recruitment (Lei et al., 2021) (Sancak et al., 2008).

1.2 mTORC1 REGULATION BY AMINO ACIDS AND FUNCTION

The mTORC1 kinase is a master growth regulator that senses many environmental cues,

including amino acids (Shimobayashi & Hall, 2016). mTORC1 comprises three subunits: mTOR, a serine/threonine protein kinase, Raptor (regulatory protein associated with mTOR) and mLST8 (mammalian lethal with SEC13 protein 8) (Aylett et al., 2016). The mTORC1 downstream signaling network is primarily involved in cell growth, where downstream effectors play a major role in protein synthesis and mRNA translation, and repress catabolic processes such as autophagy (Hay & Sonenberg, 2004) (Battaglioni et al., 2022) (Schmelzle & Hall, 2000). Thus, dysregulation of mTORC1 is linked to cancer, aging and diabetes (G. Y. Liu & Sabatini, 2020) (Saxton & Sabatini, 2017) (Gibbons et al., 2009) (Guertin & Sabatini, 2007). Nutrient-dependent recruitment of mTORC1 to lysosomes is mediated by the Rag-GTPases (Kim et al., 2008) (Sancak et al., 2008) (Anandapadamanaban et al., 2019). These small GTPases are localized in lysosomes by interacting with the pentameric Ragulator/Lamtor complex (Sancak et al., 2010) (Cui et al., 2023) (**Figure 2**).

The different mechanisms of lysosomal amino acid sensing and communication with mTORC1 and other effectors are beginning to be deciphered (Bar-Peled & Sabatini, 2014). Rencent biochemical and structural data have revealed the role of the lysosomal amino acid transceptor SNAT9/SLC38A9 on mTORC1 activation at the lysosomal membrane (Ballabio & Bonifacino, 2020) (Rebsamen et al., 2015) (Jung et al., 2015) (Wolfson & Sabatini, 2017) (Castellano et al., 2017). SLC38A9 mediates the efflux of essential amino acids from lysosomes, such as leucine, in an arginine-regulated manner (Wyant et al., 2017) (S. Wang et al., 2015). Structural studies have shown that the N-terminus of SLC38A9 is inserted deep into the transporter, in the substrate-binding pocket where arginine would normally bind (Lei et al., 2021) (S. Wang et al., 2015). However, in a high luminal arginine state, the arginine substrate competes with this N-terminal region of SLC38A9, so that this region is released to interact with and activate the Rag-GTPases required for mTORC1 activation at the lysosomal surface (**Figure 2**) (Sancak et al., 2010) (Zoncu et al., 2011) (Lei et al., 2021).

1.3 THE CSW COMPLEX

Another less studied lysosomal-mediated signaling complex is mediated by a three protein complex: C9orf72 (chromosome 9 open reading frame 72), SMCR8 (Smith–Magenis syndrome chromosomal region candidate gene 8) and WDR41 (WD repeat domain 41), called CSW (Y. Wang et al., 2015) (Slager et al., 2003) (Sellier et al., 2016). The CSW is recruited to the lysosome under amino acid starvation rather than amino acid sufficiency (Amick et al., 2020) (Amick et al., 2016). KO studies in different model organisms have stablished that the CSW is important for normal lysosomal function as well as for mTORC1 regulation (Sullivan et al., 2016) (Amick et al., 2016) (Corrionero & Horvitz, 2018). Moreover, CSW's lysosome localization is associated with cellular processes like autophagy, lysosome biogenesis or down-regulation of Toll-like receptors (Heinz et al., 2020).

Numerous studies have been focused on the CSW complex, mainly due to the extended hexanucleotide (GGGGCC) repeat in the 5' non-coding region of the C9orf72 gene, which is the most common genetic cause of two neurodegenerative diseases: amyotrophic lateral sclerosis (ALS) and frontotemporal dementia (FTD) (DeJesus-Hernandez et al., 2011) (Majounie et al., 2012) (Su et al., 2020). Two potential mechanisms leading to ALS and FTD are proposed: (i) a gain of function due to the accumulation of toxic aggregates of RNA and dipeptide repeat proteins that poison the cell and (ii) a loss of function since the hexanucleotide repeat inhibits the transcription of full-length active C9orf72, thus reducing the production of functional C9orf72 (Boivin et al., 2020) (Renton et al., 2011) (Haeusler et al., 2014) (Pang & Hu, 2021). Further understanding of the function of the CWS complex, including its lysosomal membrane localization will enable us to better understand the pathogenicity of ALS and FTD and develop therapeutic approaches.

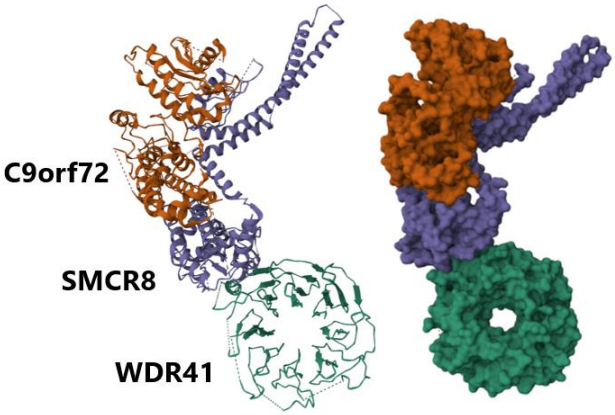

Figure 3. Cryo-EM structure of the CSW complex. PDB ID of CSW complex: 6V4U. WDR41 is shown in green, SMCR8 in purple and C9orf72 in brown (Su et al., 2020).

Recent cryo-EM studies (**Figure 3)** combined with in vitro functional data have revealed the molecular architecture and some functional insights of the CSW complex (Tang et al., 2020) (Su et al., 2020). These cryo-EM structures have revealed that SMCR8 and C9orf72 share a structural homology with the FLCN–FNIP2 complex (or folliculin complex), a GTPase-activating protein (GAP) complex that activate small GTPases from the Rag family (Tsun et al., 2013). On the other hand, the structure of WDR41 is composed by an eight-bladed β-propeller (Petit et al., 2013) (Meng & Ferguson, 2018) (Amick et al., 2016). The interaction between C9orf72 and SMCR8 is mediated by the longin and DENN (differentially expressed in normal and neoplastic cells) domains of the two proteins, structuraly similar to the FLCN–FNIP2 dimerization complex (**Figure 4**) (Shen et al., 2019) (D. Zhang et al., 2012) (Levine et al., 2013) (Yang et al., 2016). WDR41 binds to the DENN domain of SMCR8 and does not interact directly with C9orf72 (Su et al., 2020). Biochemical studies combined with site-directed mutagenesis showed that the CSW complex acts as GTPase activating proteins (GAP) for some small GTPases: Rab11A (Ras-related protein Rab-11A) and Rab8A (Ras-related protein Rab-8A) (Tang et al., 2020) (Corbier & Sellier, 2017). However, the relation beween the GAP activity of the CSW complex and the different pathologies associated with this complex still remains unclear.

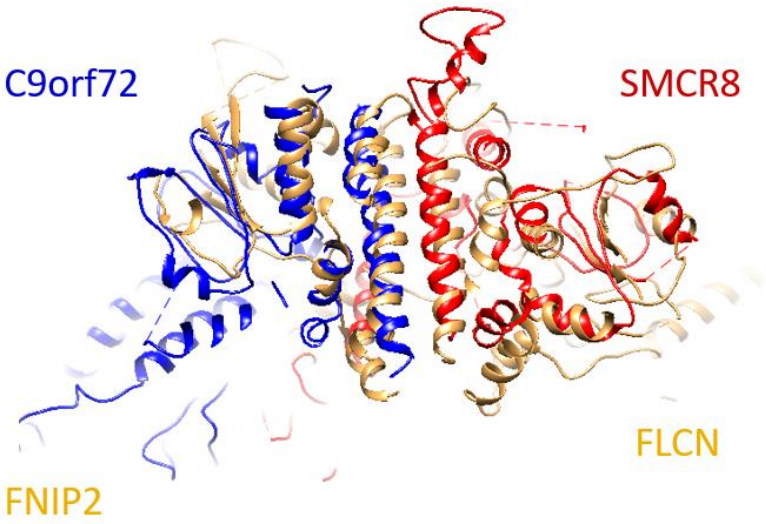

Figure 4. Structural comparison between C9orf72-SMCR8 and FLCN–FNIP2. Structural alignment of C9orf72/FNIP2 and SMCR8/FLCN. PDB ID of C9orf72-SMCR8 complex : 7O2W, PDB ID of FLCN–FNIP2 : 6ULG (Su et al., 2020) (Shen et al., 2019) (Nörpel et al., 2021).

Pull-down assays using cellular extracts have shown that upon amino acid starvation, the CSW complex is recruited at the cytoplasmic surface of lysosomes by the cationic amino acid transporter SLC66A1 (also called PQ-loop repeat-containing protein 2 or PQLC2) (Amick et al., 2016) (Amick et al., 2020) (Talaia et al., 2021) (**Figure 5**).

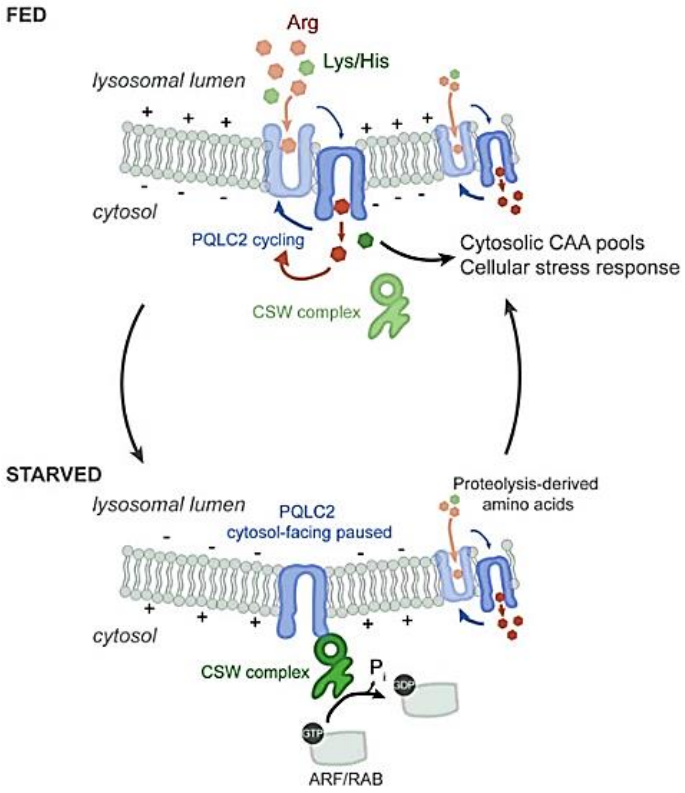

Figure 5. Mechanism of CSW lysosome recruitment by PQLC2. Under fed conditions, PQLC2 transports cationic amino acids from the lysosomal lumen to the cytosol. When the cell is starving in cationic amino acids, PQLC2 recruits the CSW at the lysosomal membrane (Amick et al., 2020) (Amick et al., 2016). Leray et al 2021 suggested a model in which, upon cationic amino acid starvation, the cytosolic open conformation of PQLC2 is stabilized promoting recruitment of the CSW complex via the interaction between PQLC2 and WDR41 (Leray et al., 2021). Refeeding or promoting proteolysis (autophagy) may increase the cysosolic pool of cationic amino acids cycling PQLC2 back to the lysosomal lumen for another round of transport Adapted from (Jain & Zoncu, 2021).

1.4 PQLC2: A LYSOSOMAL TRANSCEPTOR

Recent studies have shown that the lysosomal cationic amino acid transporter PQLC2 is the lysosomal receptor of the CSW complex (Jézégou et al., 2012) (Amick et al., 2020) (B. Liu et al., 2012). PQLC2, which is encoded by the SLC66A1 (solute carrier family 66 member 1) gene, belongs to proline-glutamine (PQ)-loop transporter family, whose members are characterized by a pair of highly conserved PQ-motifs (**Figure 6**) (Jézégou

et al., 2012). PQLC2 is predicted to have 7 transmembrane spanning domains (TM), with the N-terminal is facing the lysosomal lumen and the C-terminal end in the cytoplasmic space (**Figure 6**). High-resolution 3D structures of several members of the PQ-loop family have revealed that this family shares a similar architecture. The N-terminal (TMs 1–3), and the C-terminal (TMs 5–7) form two similar (repeats) triple helix bundles connected by the TM 4, that spans the membrane to link these two repeats, giving a 3+1+3 arrangement of TM helices (Lee et al., 2015) (Guo et al., 2022) (Löbel et al., 2022). PQ motifs in TMs 1 and 5 of PQLC2 are considered hinges that support the conformational changes required for substrate translocation. Indeed, previous studies have shown that mutations in PQ motifs block the transport activity of these transporters (Lee et al., 2015) (B. Liu et al., 2012).

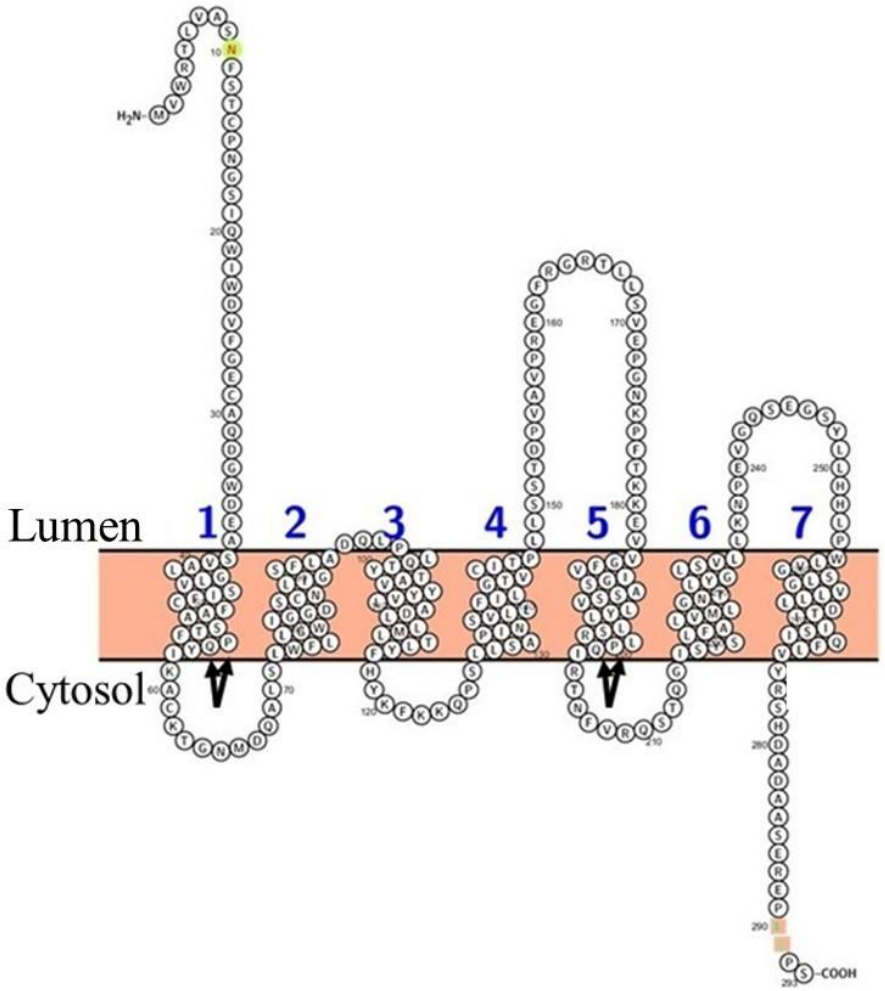

Figure 6. Predicted 2D topology of PQLC2. Visualization of the predicted 2D topology of PQLC2 generated by Protter web server (http://wlab.ethz.ch/protter) (Omasits et al., 2014). Positions of PQ motifs are indicated by arrows (in TMs 1 and 5). The 7 TM domains are indicated by numbers, the N-terminal region being located in the lumen, and the C-terminal region in the cytosol. The di-leucine lysosomal sorting motif (residues 290-291) situated at the C-terminal end is depicted in orange. Putative N-terminal N-glycosilation site (asparagine 10) is depicted in yellow.

The PQ-loop family comprises 5 members in humans. Interestingly, yeast homologues of human PQLC2 have been also identified (see phylogenetic tree in **Figure 7**) (Jézégou et al., 2012).

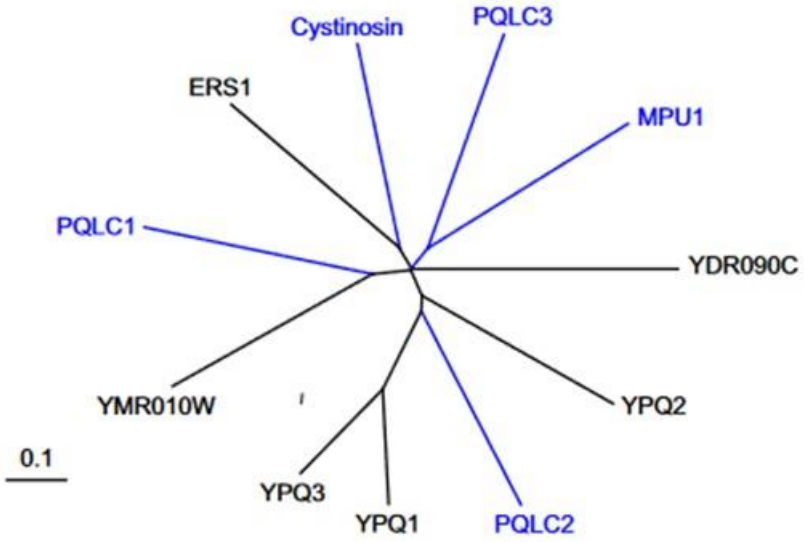

Figure 7. Phylogenetic tree of human (blue) and yeast (black) PQ-loop proteins. The figure shows the phylogenetic features aligned between members of the PQ proteins and their homologues in the yeast (Jézégou et al., 2012) (Fredriksson et al., 2008). The scale corresponds to a sequence divergence of 10%.

As commented earlier, several high resolution structures of PQ-loop transporters have described the architecture of these transporters and have helped to better understand their transport mechanism and physiological role (Lee et al., 2015) (Guo et al., 2022) (Löbel et al., 2022) (Jaehme et al., 2014). This includes two cryo-EM and crystallographic structures of cystinosin, the founder member of the PQ-loop transporter family (Guo et al., 2022) (Löbel et al., 2022). Cystinosin is a H^+-coupled lysosomal exporter of cysteine (Ruivo et al., 2012). Lysosomal cystine serves as the main reservoir for intracellular cysteine (Abu-Remaileh et al., 2017). A heredirary rare disease called cystinosis is caused by a loss of function of cystinosin resulting in the accumulation of cystine in the lysosomal lumen. Because cystine is poorly soluble, when accumulated in the lysosomal lumen, it tends to form crystals that result in cellular damage, causing dysfunction of several organs, including the kidney, eyes, thyroid or pancreas

(Elmonem et al., 2016) (Anikster et al., 1999) (Kalatzis, 2001). Cysteamine is considered the most effective treatment for cystinosis (Jézégou et al., 2012) (Gahl et al., 2002) (Pisoni, R. L. & Thoene, J. G., 1985). It reacts with cystines to form a cysteine-cysteamine mixed disulfide resembling lysine (Lys), which is indeed exported from the lysosomal lumen by PQLC2 (**Figures 8 and 9)** (Jézégou et al., 2012) (Butler & Zatz, 1984) (B. Liu et al., 2012).

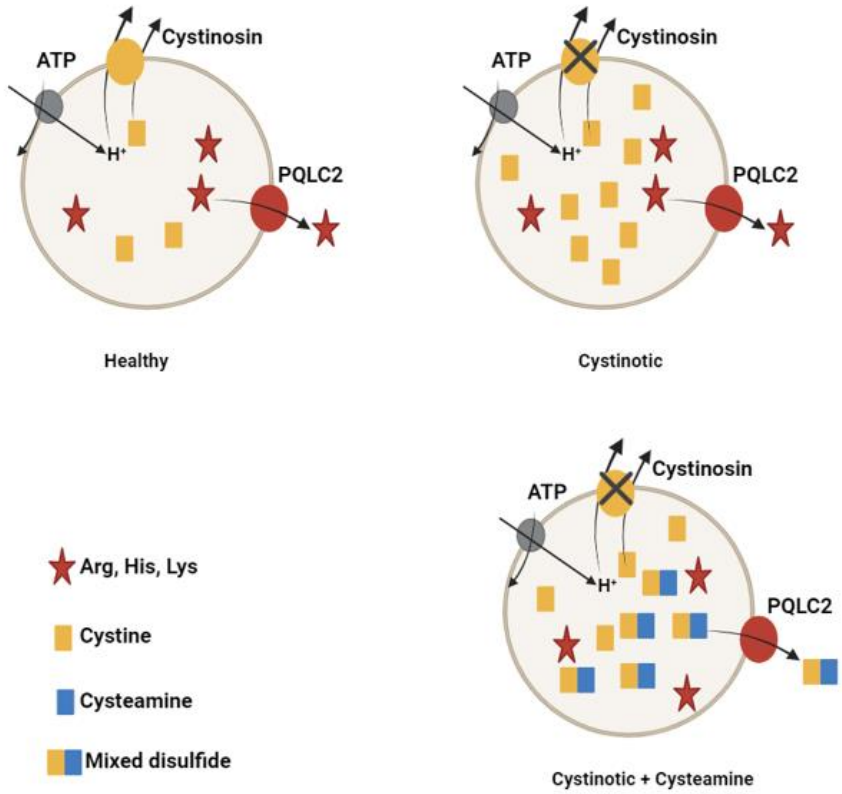

Figure 8. Schematic diagram showing the role of PQLC2 during the treatment of cystinosis by cysteamine, adapted from (Jézégou et al., 2012).

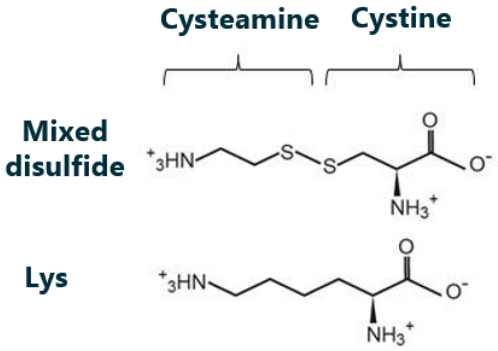

Figure 9. Chemical structures of lysine and the cysteine-cysteamine mixed disulfide.

The high resolution structures of both the human and the *Arabidopsis thaliana* cystinosin in both cytoplasmic and lumen-open states have the 3D fold already seen in previous structures of plant PQ-loop transporter (or Sweet transporter (Tao et al., 2015)) where the N-terminal TMs 1–3 and C-terminal TMs 5–7 form two similar triple helix bundles (THBs) that are connected by an inversion linker helix, TM4 (**Figure 10**) (Löbel et al., 2022) (Guo et al., 2022). A large solvent-accessible cavity opens on either the luminal or the cytoplasmic site (depending on the conformation), and it is at this central cavity where the substrate binding site is located (**Figure 11**) (Guo et al., 2022). Indeed, numerous cystinosin-causing mutations have been identified in these central cavity-lining residues consistent with their important functional role (Kalatzis, 2004).

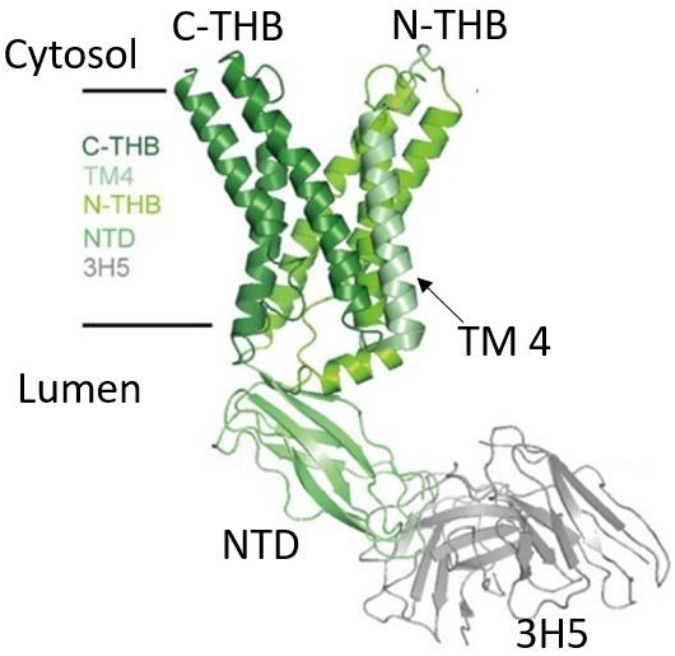

Figure 10. The Cryo-EM structure of cystinosin in cytosol-open state in complex with a Fab fragment (PDB ID : 8DKE)(Guo et al., 2022). The N-terminal TMs 1–3 and C-terminal TMs 5–7 form two similar triple helix bundles (THB) that are connected by an inversion linker helix, TM4. NTD stands for N-terminal domain and 3H5 stands for cystinosin-binding antibody 3H5 fragments (Fab^{3H5}).

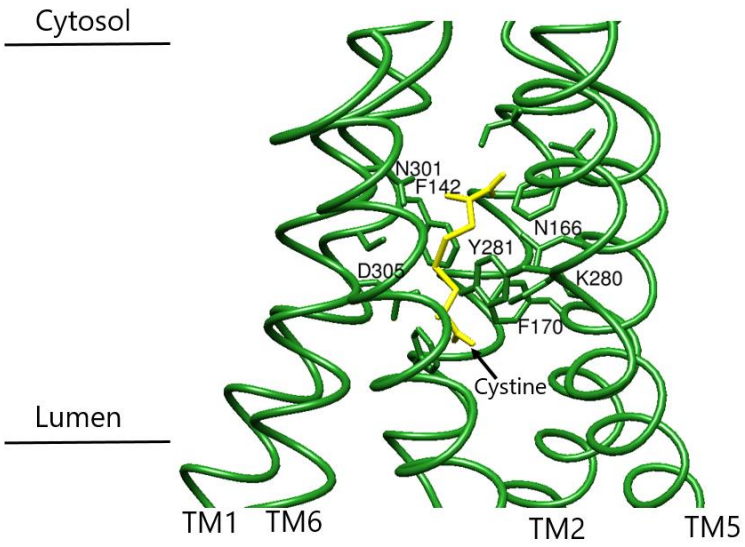

Figure 11. Cryo-EM structure of cystinosine bound to cysteine in a lumen-open conformation (PDB ID 8DKM) (Guo et al., 2022). Ribbon representation of the lumen-open conformation of cystinosine bound to cysteine with a zoomed-in view of cysteine (yellow) in the cystinosin binding pocket. Residues involved in cystine recognition at this binding pocket are numbered and depicted as sticks.

AlphaFold V2.0 is able to predict a 3D structural model of PQLC2 with a high confident score (pLDDT > 90) (**Figure 12**). Taking advantage of the recent high-resolution structures of cystinosin (Guo et al., 2022), the alignment of the AlphaFold V2.0 model of PQLC2 with the cystinosin cryo-EM cystoplasmic-open structure shows that TMs 1 and 3 and TMs 5 and 6 align very well. On the other hand, TM 4, which is the TM of the PQLC2 AlphaFold V2.0 model with lower confident score (70 > pLDDT > 50), does not align with the TM4 of cystinosin (**Figure 12**).

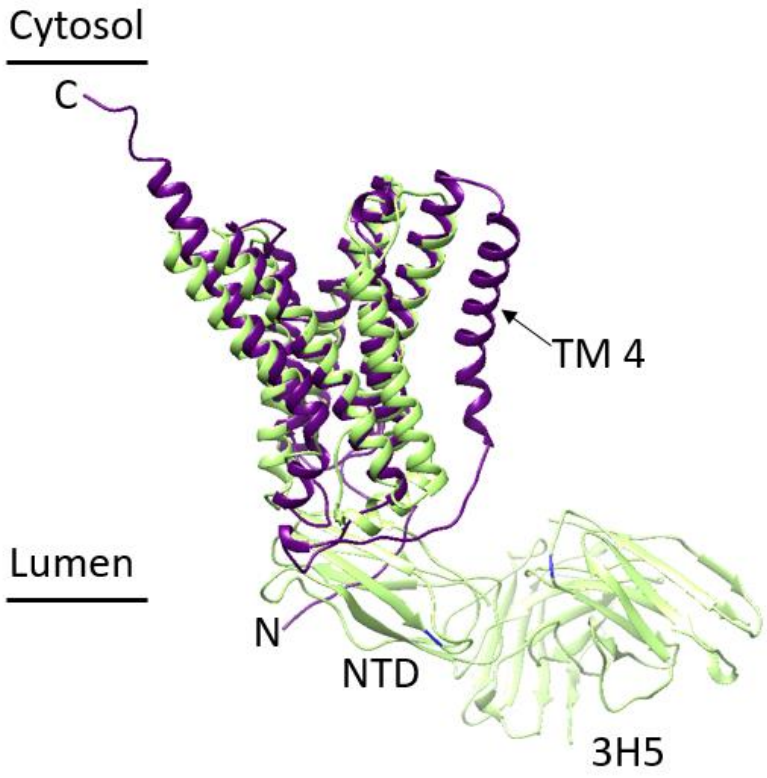

Figure 12. Overlay of the PQLC2 AlphaFold model V2.0 (purple) with the 3D structure of cystinosin (green). PDB ID of cystinosin Cryo-EM structure in the cytosol-open state : 8DKE (Guo et al., 2022).

A deep functional assessment of the transport activity of PQLC2 was possible by using recombinant PQLC2 expressed in *Xenopus laevis* oocytes by means of both, electrophysiological recordings and the uptake of radiolabeled substrates (Leray et al., 2021) (Jézégou et al., 2012). To be able to measure either PQLC2-evoqued currents or substrate uptake in oocytes, PQLC2 was redirected from the lysosomal membrane to the oocyte's plasma membrane by mutating the evolutionary-conserved dileucine-based lysosomal sorting motif situated a the C-terminal end (**Figure 7**). In this oocyte-based functional platform for PQLC2, the extracellular media mimicks the lysosomal lumen. Combining PQLC2-evoqued currents and the uptake of radiolabeled substrates, the authors showed that PQLC2 is an electrogenic transporter working as uniporter of cationic amino acids (Leray et al., 2021) (Jézégou et al., 2012) . Furthermore, using the

same approach, they found that PQLC2 is not coupled to protons, unlike other lysosomal transporters that are actively driven by the lysosomal pH gradient (Leray et al., 2021). Despite PQLC2-mediated substrate translocation is not coupled with protons, its transport activity is strongly pH-dependent. Maximal activity is found at external (equivalent to lysosomal luminal) acidic pH ~5.0 whereas no detectable activity was found at pH ≥7.0 Thus, PQLC2 catalyzes the lysosomal import or export of cationic amino acids (Lys, His, Arg) as a function of cationic amino acid gradient and the lysosomal membrane potential.

1.5 MOLECULAR DETERMINANTS OF PQLC2-CSW RECOGNITION

Recent studies have identified PQLC2 as the lysosomal membrane receptor of the CSW complex (Jézégou et al., 2012) (Amick et al., 2020). At endogenous expression levels, the interaction between WDR41 and PQLC2 is regulated by cationic amino acid availability (Amick et al., 2016) (Amick et al., 2020). That is, when the cell is depleted in cationic amino acids, the CSW complex interacts with PQLC2 at the cytoplasmic face of the lysosomal membrane. However, this interaction is reversible since refeeding the cell with these amino acids disrupts this interaction and the CSW complex is no longer localized at the lysosomal membrane. Furthermore, Shawn Ferguson's laboratory, demonstrated using pull-down assays and WDR41 KO cells that the interaction between PQLC2 and the CSW complex is mediated exclusively by WDR41 (Amick et al., 2020). Importantly, mutations in the PQ motifs of PQLC2 (P55L/P201L mutant) failed to recruit the CSW complex to lysosomes, suggesting that this interaction could be PQLC2-conformational dependent (Amick et al., 2020).

To better understand the molecular mechanism of PQLC2-CSW recognition, the laboratory of Shawn Ferguson investigated the molecular basis of PQLC2/WDR41 recognition required for PQLC2-CSW interaction (Talaia et al 2021). Since experimental cryo-EM structures of the CSW complex were not available at this moment, they built

a 3D model of WDR41 using homology modeling. The predicted model of WDR41 displays an eight bladed β-propeller with a prominent disordered loop formed at the bottom of blade 7, between β-strands C and D (7CD loop). Interestingly, in all current cryo-EM structures of WDR41 this 7CD loop is not visible due, perhaps, to its highly dynamics and lack of 3D structure.

In addition, they also built a 3D structural model of PQLC2 by homology modeling using the AtSWEET13 sugar transporter from *Arabidopsis thaliana* as template (Han et al., 2017). The resulting model of PQLC2 was very similar to the actual Alphafold V2.0 prediction (**Figure 12**), that is, made up of 7 TM domains where the N-terminal TMs 1–3 and C-terminal TMs 5–7 form two similar triple helix bundles (THBs) that are connected by an inversion linker helix, TM4, and similar to other structures of the PQ loop family (Han et al., 2017) (Guo et al., 2022) (Löbel et al., 2022). The predicted structures of PQLC2 and WDR41 were used for docking analysis using the GalaxyTongDoc webserver (Park et al., 2019). In the best ranking model, the 7CD loop (described in the previous paragraph) of WDR41 was inserted into the central cavity of PQLC2 (**Figure 13**) (Talaia et al., 2021).

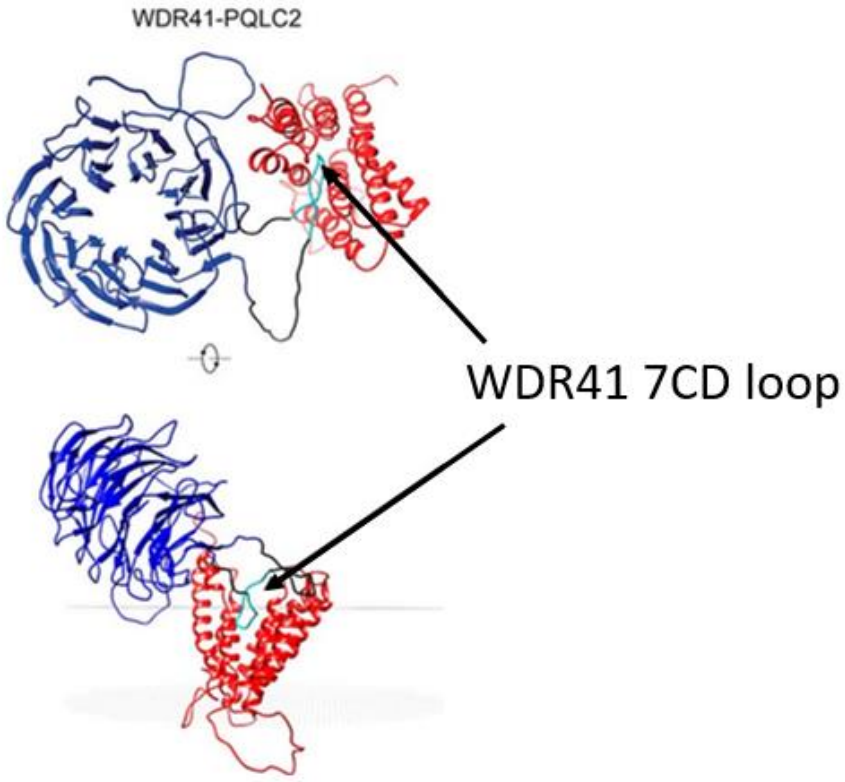

Figure 13. Docking model of WDR41 and PQLC2 (Talaia et al., 2021). The 7CD loop (light blue) of WDR41 (dark blue) inserts into the central cavity of PQLC2 (red).

Interestingly, in this docking model, the WDR41-7CD loop inserts into the cavity of PQLC2 in an analogous position to the substrate binding site of the plant PQ-loop transporter AtSWEET13 (PDB ID 5XPD) (Han et al., 2017) (Talaia et al., 2021).

To validate the proposed doking model of PQLC2-WDR41 interaction (**Figure 13**), Ferguson and colleagues carried out a series of pull-down experiments in mammalian cell cultures deprived in cationic amino acids using different mutated versions of the WDR41-7CD loop. Pull-down assays between the EGFP fused at the C-terminal end with different mutated and deleting versions of the WDR41-7CD loop, and PQLC2 allowed the identification of the minimal peptide motif within WDR41-7CD loop necessary for PQLC2 binding (turn motif in **Figure 14**) since the pull-down assays

showed that the "turn" sequence, but not the linker, was capable of interacting with PQLC2.

Figure 14. WDR41-7CD loop predicted to interact with PQLC2 (Talaia et al., 2021). In the turn region, the 10 amino acids (TGFFNMWGFG) represent the minimal linear peptide sequence able to interact with PQLC2.

Further deletions showed that 10 amino acids from 364 to 373 (TGFFNMWGFG) in the "turn" sequence were indeed sufficient for the interaction with PQLC2, and were designated as the TIP sequence (Talaia et al., 2021) (**Figures 14 and 15**). To corroborate the previous results they also performed pull-down assays with a a recombinant protein made up of GST fused to TIP sequence (the 10 amino acids) and PQLC2-FLAG. Moreover, site-directed mutagenesis of the WDR41-7CD loop in the full-lengh WDR41 mapped the key residues within the turn motif of WDR41-7CD loop crucial for PQLC2 binding (F366, F367, N368, M369 and W370) (**Figure 15**) (Talaia et al., 2021).

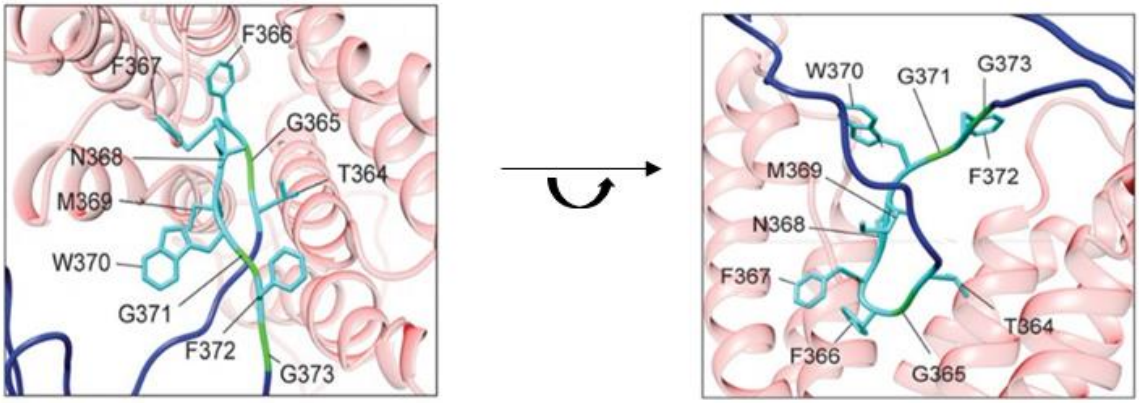

Figure 15. Docking model of the TIP sequence WDR41-7CD loop with PQLC2 (Talaia et al., 2021). The 10 amino acids within the WDR41-7CD loop (364-TGFFNMWGFG-373) inserts into the central cavity of PQLC2 (Talaia et al., 2021). The predicted structure of PQLC2 is shown in light red (front and side view), while the predicted TIP sequence of WDR41 is shown in light blue. The docking model was built by the GalaxyTongDoc webserver (Eswar et al., 2006) using predicted structures of WDR41 and PQLC2 made by homology modeling.

Furthermore, alanine replacement of highly conserved residues predicted to be at the central cavity of PQLC2 (F49, Y105, and Y195) inhibit the interaction with the WDR41 TIP sequence, suggesting their pivotal role on WDR41 recruitment (Talaia et al., 2021). **Figure 16** represents the predicted structural model of PQLC2 made by homology modeling uing AtSWEET13 from *Arabidopsis thaliana* as template (Talaia et al., 2021), and the predicted AlphaFold V2.0 model of PQLC2 showing a set of highly conserved aromatic residues predicted to align in the cavity of PQLC2. Interestingly, comparison of the two predicted models shows similar positions of the conserved residues in the central cavity, providing further insight into the AlphaFold V2.0 model of PQLC2.

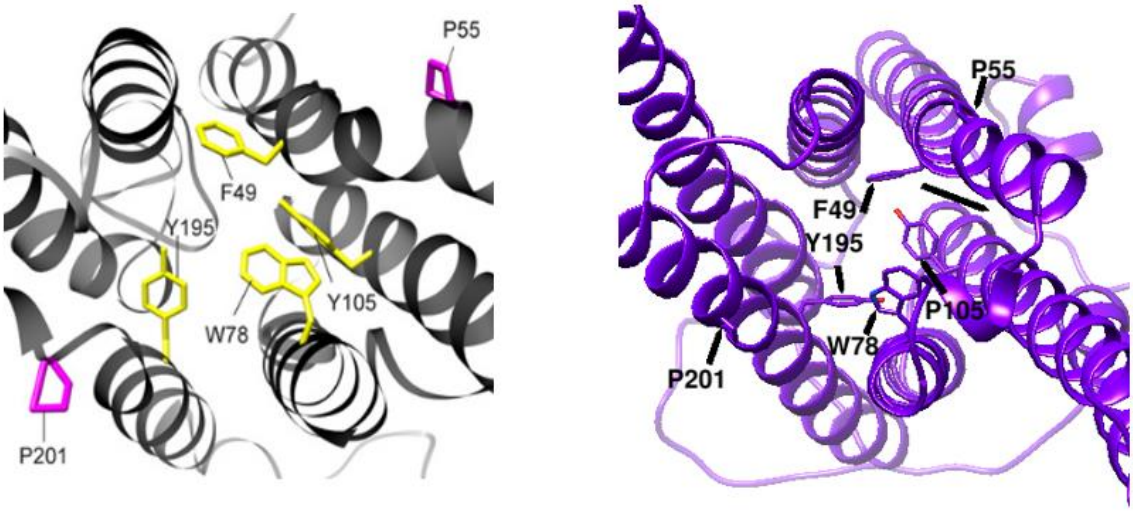

Figure 16. Predicted structural models of PQLC2. (left) homology model (Talaia et al., 2021) , (right) AlphaFold V2.0 model. Both models display a set of highly conserved aromatic residues (depicted as sticks) predicted to align in the central cavity of PQLC2: F49, W78, Y105, and Y195A, in addition to PQ-motif residues P55 and P201.

Previous studies have shown that the PQ motifs function as hinges of PQ-loop transporters, required to transit from inward to outward facing conformations necessary to translocate their substrates (Jézégou et al., 2012) (B. Liu et al., 2012) (Kawano-Kawada et al., 2019). Subtitutions of the proline residues of the PQ motif by leucines abolishes their transport activity. Notably, the same substitutions in PQLC2 (P55L/P201L) abolish the interaction of PQLC2 with WDR41 TIP sequence and the recruitment of CSW complex to the lysosomal surface (Amick et al., 2020) (Talaia et al., 2021). These results support a model wherein a specific conformational state within the alternating access transporter model mediates the WDR41 recruitment to the cytoplasmic surface of lysosomes and thus provides a potential mechanism for the transceptor properties of PQLC2 (Leray et al., 2021).

Functional characterization of PQLC2 expressed in *Xenopus* oocytes done by the team of Bruno Gasnier (U. Paris Cité) have suggested a model linking Arg recognition and transport by PQLC2 with its tranceptor role (Leray et al., 2021). This team discovered a

unique regulation of PQLC2 by Arg. In the “trans” compartment, which is the subtrate release side, the presence of Arg inhibits PQLC2 transport activity. To understand how the kinetic model works, they performed single-transporter simulations and examined the dwelling time of PQLC2 at specific step of the cycle (Leray et al., 2021). This has led to the putative model of the interaction between PQLC2 and the CSW complex (**Figure 17**). In the absence of amino acids, mTORC1 inactivation induces the lysosomal depolarization, after which the cytosol-facing conformation of PQLC2 is favored, helping the recruitment of the CSW complex to the lysosome surface. Subsequently, autophagy leads to an increase in amino acid content in the cytosol, the increase in Arg levels would shorten the cytosol-facing pauses of PQLC2, thus releasing the CSW complex. In conclusion, lysosomal depolarization and cytosolic Arg play an antagonistic role in regulating the duration of PQLC2 pauses in the cytosol-oriented conformation. Moreover, this putative model of interaction between PQLC2 and the CSW complex also opens the question wether this interaction can also be induced by mTORC1 inactivation that also results on lysosomal membrane depolarization.

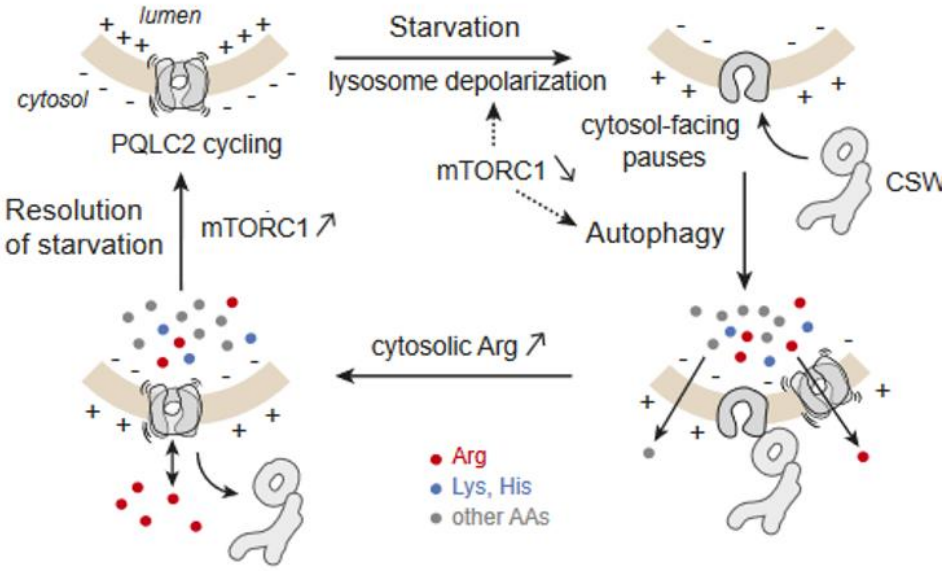

Figure 17. Putative model of the interaction between PQLC2 and the CSW complex, adapted from (Leray et al., 2021). This interaction is regulated by the presence of cationic amino acids (Arg, His, Lys). Lysosomal depolarization and cytosolic Arg may also play an antagonistic role in regulating the duration of PQLC2 pauses in the cytosol-facing conformation.

2 OBJECTIVES

In this project, we investigate the mammalian amino acid transceptor, PQ loop repeat-containing protein 2 (PQLC2, SLC66A1) (Gasnier, 2021). This protein is located in the lysosomal membrane of mammalian cells, where it plays two roles (Jézégou et al., 2012). Firstly, it exports cationic amino acids from the lysosomal lumen to the cytosol, and secondly, it acts as a receptor for a cytosolic protein complex known as the CSW complex (**Figure 18**) (Amick et al., 2020): the GTPase-activating proteins C9ORF72 and SMCR8, and WDR41, the anchor between CSW and PQLC2 (Tang et al., 2020). Lysosomal localization of the CSW complex is pivotal in normal lysosomal function and is linked with mTORC1 regulation, indicating that the CSW/PQLC2 interaction is likely involved in a new lysosomal-mediated cell signaling pathway. Moreover, congenital mutations in the gene encoding C9ORF72 causes familial forms of amyotrophic lateral sclerosis and frontotemporal dementia (Majounie et al., 2012) (Sullivan et al., 2016).

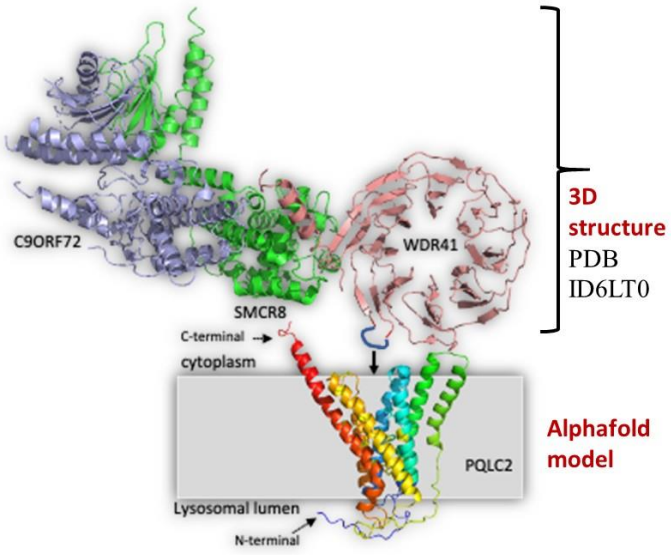

Figure 18: Scheme of CSW/PQLC2 interaction.

Combining predicting models with pull-down assays in cellular extracts, previous studies have concluded that a protruding loop in WDR41 (WDR41 loop) is sufficient and the main responsible for the recruitment of CSW by PQLC2 in a PQLC2-dependent conformational manner (Talaia et al., 2021) (Amick et al., 2020) (Gasnier, 2021) (**Figure 19**). It is worth mentioning that the WDR41 loop is not resolved in the cryo-EM structures recently obtained for WDR41, suggesting its flexibility (Tang et al., 2020) (Su et al., 2020).

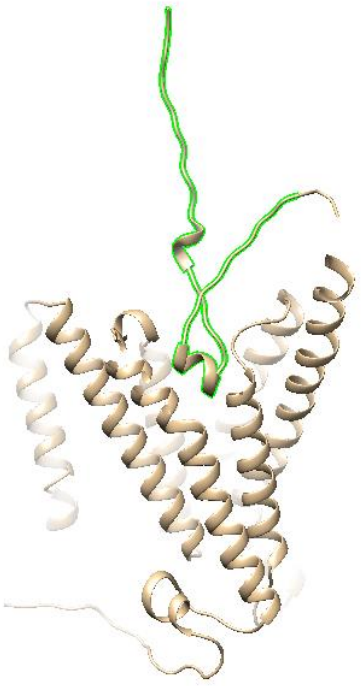

Figure 19. Alphafold modeling of WDR41 loop (green) and PQLC2 (brown) interaction.

The interaction of PQLC2 with the CSW complex has so far been studied in living cells and cell homogenates (Leray et al., 2021) (Amick et al., 2020) (Talaia et al., 2021). In both cases, the interaction of other proteins could not be excluded. **Therefore, *in vitro***

experiments with purified PQLC2 are crucial to gain insight into the molecular basis of the PQLC2 amino acid sensing mechanism.

Objectives of this Project:

1. **Obtaining a purified and stable PQLC2 in detergent micelles.** To date, no study has reported the purification of a mammalian PQLC2 from etiher endogenous or recombinant sources. Therefore the first objective is to establish a robust protocol for expressing and purifying PQLC2, enabling us to perform a variety of structural and functional characterization assays *in vitro*, and to investigate the functional and structural features of this transporter.
2. **Functional characterization of PQLC2 recontituted into liposomes.** This objective focuses on investigating the functional properties of yeast-produced PQLC2. We aim to establish a protocol for reconstituting the purified transporter into liposomes, allowing us to assess its transport activity using radiolabeled ligands.
3. ***In vitro* studies of PQLC2/WDR41 interaction using purified proteins.** In this objective, we will explore the *in vitro* interaction between purified PQLC2 and the WDR41-7CD loop using EPR spectroscopy to gain insights into their molecular interaction.

3 MATERIAL AND METHODS:

3.1 MATERIAL

3.1.1 Chemical products :

EcoRI, NotI, 1 kb DNA ladder, CutSmart® buffer and gel loading dye, purple (6X) were purchased from New England Biolabs. Luria-Bertani broth (LB) and Bovine Serum Albumin (BSA) media were purchased from CARL ROTH. Gibco ™ Peptone Bacto and Gibco™ Bacto™ Yeast Extract were purchased from Gibco. BD DIFCO™ Wort Agar, BD Difco™ Yeast Nitrogen Base (without Amino Acids and with Ammonium Sulfate) and Gibco™ Difco™ Casamino Acids were purchased from BD. Ethylene diamine tetraacetic acid (EDTA)-free SIGMAFAST ™ Protease Inhibitor Cocktail (PIC), phenylmethylsulfonyl fluoride (PMSF), isopropyl β-D-1-thiogalactopyranoside (IPTG), Bicinchoninic acid (BCA), copper (II) sulfate solution, ethidium bromide (EB), salmon sperm DNA (SSD), TALON® Superflow, 7-Diethylamino-3-(4′-maleimidylphenyl)-4-methylcoumarin (CPM), cholesteryl hemisuccinate (CHS), 3-Maleimido-2,2,5,5-tetramethyl-1-pyrrolidinyloxy (3-Maleimido-PROXYL) and valinomycin were purchased from Sigma - Aldrich. Goat anti-mouse IgG- horseradish peroxidase (HRP) and goat anti-rabbit IgG-HRP conjugated secondary antibodies, Dual Xtra and All blue Precision Plus Protein™ Prestained Standards, Bio-Beads™, 4-15% Mini-PROTEAN® Precast gels, 16.5% Mini-PROTEAN® Tris-Tricine gels and 30% Acrylamide/Bis Solution (29:1) were purchased from Bio-Rad. n-Dodecyl- β- maltopyranoside (DDM), N-decyl- β -maltoside (DM) and lauryl maltose neopentyl glycol (LMNG) were purshased from Anatrace. The rabbit anti-PQLC2 primary antibody targeting the cytoplasmic loop (1-8) was generously provided by Bruno Gasnier's team (Laboratoire de Dynamique des Membranes at the Institut des Neurosciences Saints-Pères Paris, Université Paris Cité). Tris(2-carboxyethyl)phosphine (TCEP) was purchased from Alfa Aesar. ECL Select™ Western Blotting Detection kit was purchased from GE healthcare. 1,2-Dioleoyl-sn-glycero-3-phosphocholine (DOPC) and 1,2-dioleoyl-sn-glycero-3-phosphoethanolamine (DOPE) were purchased from Avanti Polar Lipids. TALON® metal affinity resins were purchased from Clontech. N-

hydroxysuccinimide (NHS)-Activated Sepharose 4 Fast Flow resins were purchased from Cytiva. Hrv-3C protease was purchased from ACROBiosystems. XL1-Blue competent cells and Quikchange II kit were purchased from Agilent Technologies. NucleoSpin Plasmid kit (NoLid) was purchased from Macherey-Nagel. L-Arginine was purchased from PerkinElmer, L-Histidine and L-Lysine were purchased from Moravek Inc. The synthetic peptides encoding WDR41-7CD loop with Cysteines (**Table 6**) were purchased from Genecust. WDR41-7CD loop coupled to Cy3 was purchased from Genscript.

3.1.2 Equipments and other matherials:

Planetary Mono Mill PULVERISETTE 6 (Fritsch). NanoDrop™ and Pierce™ Strong Cation Exchange columns (Thermo Fisher). ÄKTA purifying chromatography system and Superose 6 increase 10/300 GL column were purchased from GE Healthcare (now Cytiva). GelAir Cellophane support, ChemiDoc imaging systems and affinty purification column (Poly-Prep® Chromatography Columns) (Bio-Rad). Immobilon®-P polyvinylidene difluoride membranes (PVDF), MF-Millipore™ membrane filters, GD/X Whatman® syringe filters and Sterile 500 mL Steritop Quick Release (0.22 µM pore size made of fast-flow polyethersulfone (PES)) were purchased from Merck. Gel-doc imagine system CCD camera (Syngene). Vivaspin® 20 concentrators were purchased from Sartorius Stedium Biotech. Vibra-Cell™ 75041 sonicator (Avantor). ELEXYS spectrometer (Bruker). Tri-Carb® liquid scintillation Counter (PerkinElmer). Fluorescence detector (FP-4025) (JASCO). Zetasizer (Malvern Panalytical). BioTek Epoch 2 Absorbance Plate Reader (BioTek Instruments).

3.1.3 Biological products

3.1.3.1 Bacterial strains

3.1.3.1.1 XL1-Blue *Escherichia coli* (*E. coli*) strain

XL1-Blue *E. coli* strain was used for DNA cloning, amplification and site-directed mutagenesis. The genotype of this strain is *recA1 endA1 gyrA96 thi-1 hsdR17 supE44 relA1 lac [F proAB lacIqZΔM15 Tn10* (*Tetr*)]. This strain lacks endonucleases (endA), which improves the quality of the DNA generated, and is recombination-deficient (recA), which improves the stability of the inserted DNA. The hsdR mutation inhibits endonuclease cleavage of cloned DNA. The *lacIqZΔM15* gene allows blue-white screening of recombinant plasmids. This strain is resistant to tetracycline.

3.1.3.1.2 BL21 *E. coli* strain

BL2-Gold (DE3) *E. coli* strain was used for the expression of nanoGFP. The genotype of this strain is *F– ompT HSDSB* (rB^{-}, mB^{-}) *gal dcm* (*DE3*). This strain carries the lamda DE3 prophage that expresses T7 RNA polymerase under the control of a lacUV5 promoter. The promoter is induced by the addition of IPTG.

3.1.3.2 Yeast strain *S. cerevisiae*

The various proteins were expressed in *S. cerevisiae* strain W3031b Gal4-2 (*α, leu2, his3, trp1: TRP1-GAL10-GAL4, ura3, ade2*$^{-1}$, *can*^{r}, *cir*$^{+}$) (Lenoir et al., 2002) (**Table 1**). This *S. cerevisiae* strain is auxotrophic for two amino acids: leucine (leu) and histidine (his) and for the two nitrogenous bases adenine (ade) and uracil (ura). These substances must therefore be added to the yeast culture. The *S. cerevisiae* strain initially contained a single copy of the Gal4 transcription factor, which interacts with the Gal10/Cyc1 hybrid promoter, resulting in low expression of the target gene. A second copy of the Gal4 gene was therefore introduced by homologous recombination into the genome of strain W3031b Gal4-2 to increase PQLC2 expression (Schultz et al., 1987). After glucose

depletion and addition of galactose, suppression of Gal80 is lifted (Johnston, 1999), enabling production of the Gal4 transcription factor, which interacts with and induces the Gal10/Cyc1 promoter (**Figure 20**).

Table 1. Gene symbols and interpretation of W3031b Gal4-2 (*α, leu2, his3, trp1: TRP1-GAL10-GAL4, ura3, ade2^{-1}, can^{r}, cir^{+}*). Adapted from: *Saccharomyces* Genome Database, Sherman, F., 1998 and Jidenko MH., 2005.

Gene symbol	Interpretation
A	Reproduction type of strain
leu2 *his3* *ura3* *ade2^{-1}*	Auxotrophic strain for leucine, histidine, uracil and adenine
trp1: TRP1-GAL10-GAL4	Insertion of genes coding for TRyPtophan (TRP1) and GALactose (GAL) metabolism under the control of the GAL10 promoter. *TRP1* and *GAL4* are both functional
can^{r}	Strain resistant to CANavanine
cir^{+}	*2-micrometer* (*2μ*) circle DNA

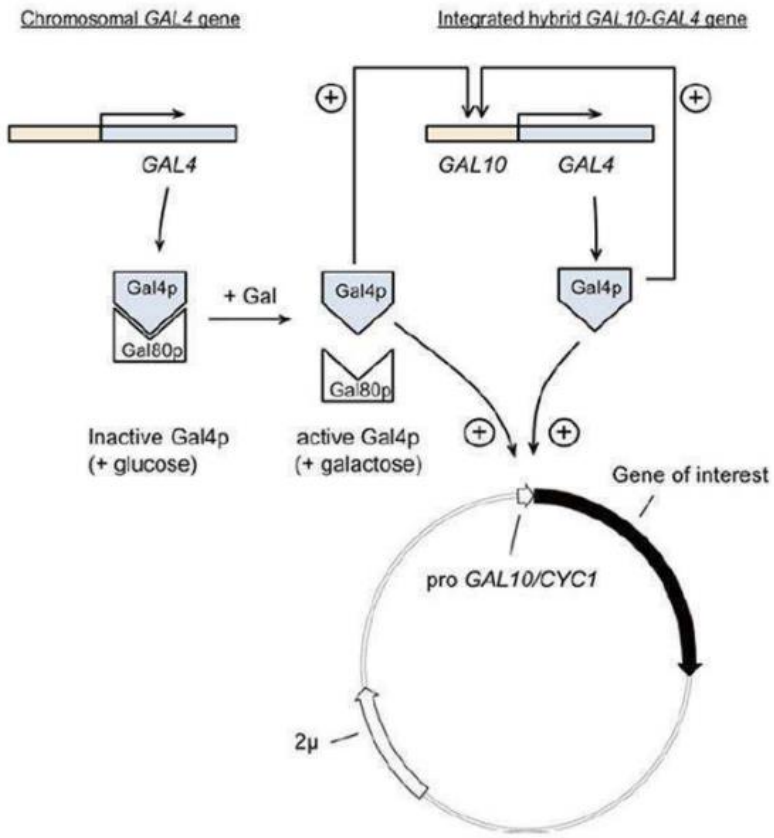

Figure 20. Induction of PQLC2 expression *in S. cerevisiae*, adapted from (Azouaoui et al., 2016). An additional copy of the *GAL4* gene is present in the W3031b Gal4-2 strain. *Gal4* is under the control of *GAL10* promoter. In the presence of glucose, Gal80p represses the Gal4 protein. Then, in the presence of galactose and in the absence of glucose, the interaction between Gal4p and Gal80p is disrupted and Gal4p activates GAL promoters (Bhat & Murthy, 2001)**.**

3.1.4 Buffers and culture media

3.1.4.1 Buffers:

TB buffer : 10 mM 2,2'-(piperazine-1,4-diyl)bis(ethanesulfonic acid) (PIPES), 15 mM $CaCl_2$, 250 mM KCl, 55 mM $MnCl_2$.

BCA working solution : 49 volumes of BCA, 1 volume of copper (II) sulfate, 2 % sodium dodecylsulfate (SDS).

Loading buffer (2X) for SDS-PAGE: 100 mM Tris-HCl (pH=6.8), 1.4 M β-mercaptoethanol, 5% (w/v) SDS, 1 mM EDTA, 9 M urea and 0.01% (w/v) bromophenol blue.

Loading buffer (2X) for Native PAGE : 200 mM Tris-HCl (pH=6.8), 40% (v/v) glycerol, 0.04% (w/v) coomassie brilliant blue R-250, 2% β-mercaptoethanol or 100 mM dithiothreitol (DTT) (added freshly).

SDS-PAGE running buffer (1X) : 2.5 mM Tris, 0.025 M glycine, 0.01% SDS.

Native PAGE running buffer (1X) : 100 mM Tris, 100 mM Tricine.

Coomassie blue staining solution: 0.1% (w/v) coomassie brilliant blue R-250, 40% (v/v) methanol and 10% (v/v) acetic acid.

Destaining buffer : 40% H_2O, 10% acetic acid, 50% methanol.

Fixation buffer : 10% (v/v) ethanol, 10% (v/v) acetic acid and 5% (v/v) glycerol.

Transfer buffer : 27.6 mM Tris, 192 mM glycine, 10% (v/v) methanol.

Blocking buffer : 5% of milk (fat free) phosphate-buffered saline (PBS)/Tween® 20.

PBS/Tween® 20 : PBS, 0.02% TWEEN.

For the filtration of the following stock solutions and buffer, Whatman® GD/X 0.22 µM syringe filters were used.

10% DDM/2% CHS stock solution : 200 mM Tris (pH=8), 10% (w/v) DDM, 2% (w/v) CHS.

5% LMNG/1% CHS stock solution : 100 mM Tris (pH=8), 5 % (w/v) LMNG, 1% (w/v) CHS.

PLATE buffer : 40% polyethylene glycol (PEG) 4000, 100 mM lithium acetate, 10 mM Tris-HCl pH 7.5 and 1 mM EDTA.

For the filtration of the following buffers, Sterile Sterile 500 mL Steritop Quick Release filters (0.22 µM pore size made of fast-flow polyethersulfone (PES)) were used.

PBS (10X) : 27 mM KCl, 1.4 M NaCl, 0.13 M Na_2HPO_4 and 18 mM KH_2PO_4 (pH=7.4).

TEKS buffer : 50 mM Tris-HCl (pH=7.5), 1 mM EDTA, 0.1 M KCl and 0.6 M sorbitol.

TES buffer : 50 mM Tris-HCl (pH=7.5), 1 mM EDTA and 0.6 M sorbitol.

HEPES sucrose buffer : 20 mM HEPES-Tris (pH=7.4), 0.3 M sucrose, 150 mM NaCl.

Lysis buffer : PBS pH 8, 0.5 M NaCl, 5 mM imidazole, EDTA-free PIC (1X), 1 mM PMSF, 10 mM $MgCl_2$ and 10 µg DNAase.

FSEC buffer : 20 mM Tris-HCl (pH=7.8), 150 mM NaCl, 10% (v/v) glycerol, 0.02% DDM. The buffer was then degassed.

Washing buffer 1 for affinity purification : 20 mM Tris-HCl (pH=7.8), 150 mM NaCl, 10% (v/v) glycerol, 0.02% DDM.

Elution buffer for affinity purification : 20 mM Tris-HCl (pH=7.8), 300 mM NaCl, 10% (v/v) glycerol, 0.02% DDM, 1 mM EDTA, 1 mM DTT.

FSEC exchange buffer : 20 mM Tris-HCl (pH=7.8), 150 mM NaCl, 10% (v/v) glycerol, 0.015% LMNG. The buffer was then degassed.

Reconstitution buffer : 10 mM HEPES-KOH (pH=7.5), 100 mM K_2SO_4, 2 mM $MgSO_4$, +/- cold L-arg.

Transport buffer 1 : 10 mM MES (pH=5), 100 mM Na_2SO_4, 50 µM cold L- arg or L-Lys, 0.5 or 1 µCi [^{3}H] L-arg or L-Lys.

Stop buffer 1 : 10 mM HEPES (pH=7.4), 100 mM K_2SO_4, 10 mM L-arg or L-lys.

Transport buffer 2 : 10 mM Tris-HEPES (pH=7.4), 0.5 mM EDTA, 1 Mm $MgSO_4$, 1 % (v/v) glycerol, 10 µM cold L-arg, 0.5 µCi [^{3}H] L-arg.

Stop buffer 2 : 10 mM HEPES (pH=6.8), 5 mM L-arg.

Resuspension buffer 1 : 20 mM Tris-HCl pH=7.6, 150 mM NaCl, 5 % (v/v) glycerol, PIC (1X), DNase, 0.5 mM EDTA.

Resuspension buffer 2 : 20 mM Tris-HCl (pH=7.6), 200 mM NaCl and 10% (v/v) glycerol.

Column buffer : 20 mM Tris-HCl (pH=7.8), 200 mM NaCl, 10% (v/v) glycerol, 0.01% (v/v) DDM.

TD buffer : 20 mM Tris-HCl (pH=7.6), 150 mM NaCl (+/- L-arg).

3.1.4.2 Culture media:

3.1.4.2.1 *E. coli* culture media :

SOB media : 2 % (w/v) Gibco ™ Peptone Bacto, 0.5% (w/v) Gibco™ Bacto™ Yeast Extract, 10 mM NaCl, 2.5 mM KCl, 10 mM $MgCl_2$, 10 mM $MgSO_4$. For the filtration of buffer, Whatman® GD/X 0.45 µM syringe filters were used (Gietz & Schiestl, 2007).

LB media : 8.5 mM NaCl, 0.5 % (w/v) Tryptone, 0.1 % (w/v) Gibco™ Bacto™ Yeast Extract. For the plates : +/- 2 % (w/v) agar.

3.1.4.2.2 *S. cerevisiae* culture media:

All compounds except ethanol, glucose, adenine and uracil were mixed and then autoclaved. After autoclaving, ethanol, glucose, adenine and uracil were added just

prior to culture.

YPGE2X rich medium : 2% (w/v) Gibco ™ Peptone Bacto, 2% (w/v) Gibco™ Bacto™ Yeast Extract, 1% (w/v) glucose and 2.7% (w/v) ethanol.

S6A/S6AU minimal medium : 0.1% (w/v) Gibco™ Difco™ Casamino Acids, 0.7% (w/v) BD Difco™ Yeast Nitrogen Base (without Amino Acids and with Ammonium Sulfate), 2% (w/v) glucose, 20 µg/mL adenine, +/- 20 µg/mL uracil. For the plates : +/- 2 % (w/v) agar.

3.2 METHODS

3.2.1 Expression vector

3.2.1.1 pYeDP60 : expression vector in the *S. cerevisiae*

The pYeDP60 vector used in our laboratory was originally provided by Denis Pompon (Pompon et al., 1996). This vector can be cloned in *E. coli* as it possesses a bacterial origin of replication (*Ori*), and an Amp^R ampicillin resistance gene which allows plasmid selection during cloning and amplification (**Figure 21**). This vector also possesses features required for expression and selection in yeast. *2µ* is the yeast origin of replication, and *ADE2* and *URA3* are auxotrophic selection markers for ade and ura respectively. The vector also includes the following features for gene expression: Gal10/Cyc1 hybrid promoter (Guarente et al., 1982), phosphoglycerate kinase terminator, PQLC2 fused to a green fluorescent protein (GFP) and Hrv-3C protease cleavage site.

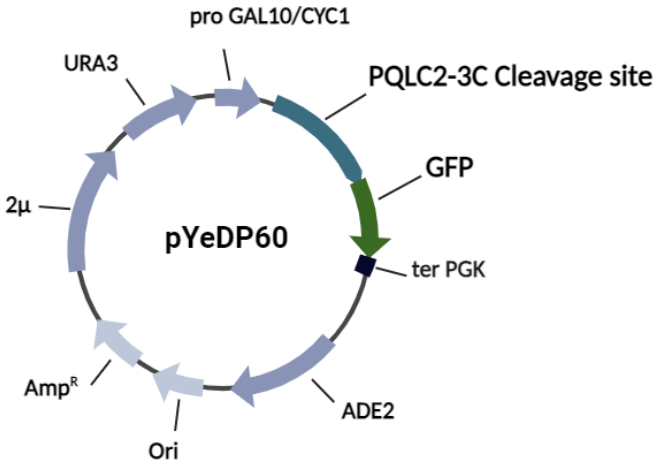

Figure 21. Map of the pYeDP60 plasmid containing PQLC2 gene (Azouaoui et al., 2014a) (Veen et al., 2021). **Amplification in *E. coli* :** *Ori*: bacterial origin of replication; *Amp*^{R}: ampicillin resistance gene. **Amplification and selection in yeast :** *2µ*: yeast origin of replication; *ADE2*: auxotrophic selection marker for ade, *URA3*: auxotrophic selection marker for uracil. **For expression :** GAL10/CYC1 promoter: Gal10/Cyc1 hybrid promoter; ter PGK: phosphoglycerate kinase terminator. GFP: green fluorescent protein; 3C Cleavage site : Hrv-3C protease cleavage site.

3.2.2 Cloning strategy

3.2.2.1 Construction of the expression vector pYeDP60 PQLC2

The cDNA sequence encoding PQLC2 was amplified by PCR from pOX(+) vector (Jézégou et al., 2012), generously provided by Bruno Gasnier's team (Laboratoire de Dynamique des Membranes at the Institut des Neurosciences Saints-Pères Paris, Université Paris Cité), and inserted between the EcoRI/NotI sites of pYeDP60. The cDNAs encoding the different versions of PQLC2, including the consensus one (thereafter refered as csPQLC2), were synthetized by Genscript and inserted into the pYeDP60 vector between the EcoRI and NotI restriction sites (Lamy et al., 2021).

3.2.2.2 Introduction of superfolder GFP

The introduction of superfolder GFP (referred as GFP) was carried out as previously described (Lamy et al., 2021). To introduce GFP at the C-terminus of PQLC2, a PCR DNA fragments encoding the GFP with the 3C-protease recognition sequence at the extreme 5' and a stop codon at the extreme 3' was introduced between the NotI and XmaI sites of the pYeDP60-PQLC2 vector to finally generate pYeDP60-PQLC2-3C-GFP.

3.2.3 Preparation of super competent XL1-blue cells

Standard protocol described by (Gietz & Schiestl, 2007) was followed for the preparation of super-competent bacteria.

XL1 blue *E. coli* cells were incubated in 5 ml of Luria broth (LB) medium supplemented with 50 µg/ml tetracycline, ON at 37°C with shaking at 200 rpm. 200 µL of the previous culture was incubated with 100 ml of SOB medium at 18°C with shaking at 200 rpm. After approximately 48 h, once the optical density (OD_{600}) reached ~0.6, the culture was placed on ice for 10 min, then the cells were centrifuged (5 min at 1,000 x g, 4°C). The pellet was then resuspended in 32 ml cold TB buffer. The pH of this buffer was adjusted to 6.7 with KOH prior de addition of $MnCl_2$. The resuspended pellet was placed on ice for 10 min then centrifuged (5 min at 1,000 x g, 4°C). The supernedant was discarded and the pellet was resuspended in 8 mL of TB buffer supplemented with 7% of dimethyl sulphoxide (DMSO), and placed on ice for 10 min. 200 µL aliquotes were flash frozen in liquid nitrogen and stored at -80°C.

3.2.4 Site-directed mutagenesis of PQLC2 (Contruction of consensus PQLC2 F49A)

The cDNA encoding consensus PQLC2 P55L/P201L was synthetized by Genscript and cloned into the pYde60 vector as described in section 2.1. Contruction of consensus

PQLC2 F49A was done by site-directed mutagenesis using Quikchange II kit (**Figure 22**) (see **Table 2** for the primers). pYeDP60-csPQLC2-3C-GFP was used as a template for the PCR (see **Table 3** for the PCR reaction protocol). After the PCR reaction, the methylated template cDNA was digested with DpnI. Aproximately 50 ng of the digested PCR product was transformed by heat shock in *E. coli* XL1-Blue super competent cells and plated in LB-agar plates containing 100 µg/mL ampicillin and incubated ON at 37°C. Individual bacterial colonies were picked and cultivated in 4 mL LB ampicillin. Plasmid DNA was isolated using NucleoSpin Plasmid kit and mutations were confirmed by DNA sequencing.

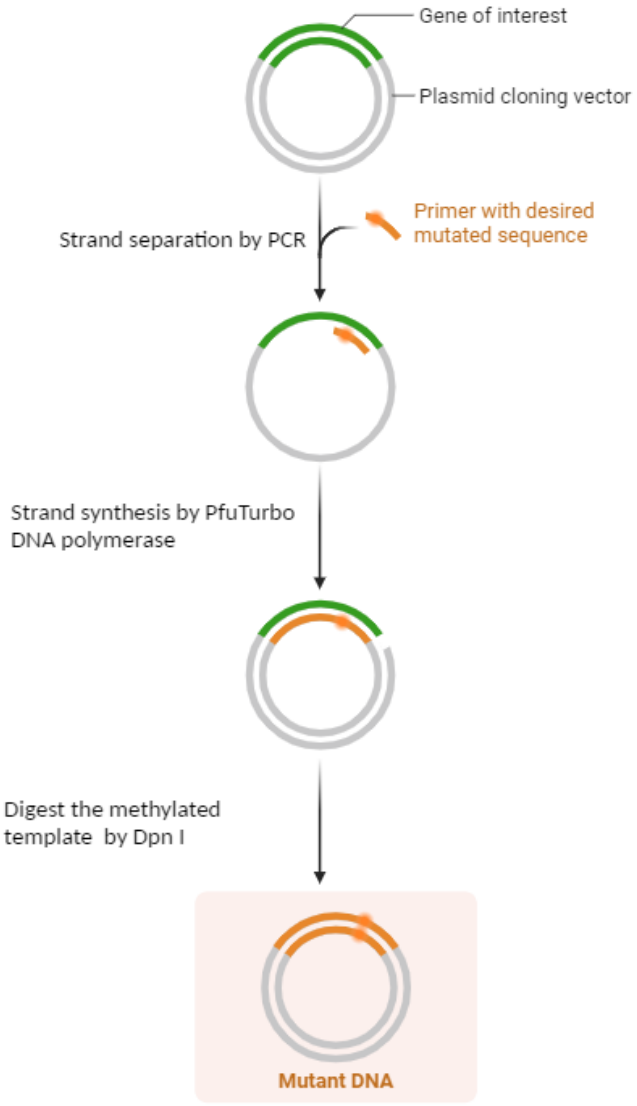

Figure 22. Schematic diagram of site-directed mutagenesis using Quickchange strategy. PQLC2 consensus F49A was constructed by site-directed mutagenesis. Synthesis of mutant strands by PCR using primers with the desired mutation site. Digestion of the template containing methylated sites by DpnI.

Table 2. PQLC2 mutant generated with the associated primers used for the PCR reaction.

Mutants	Primers
F49A	Forward : CTGGGCTTGATTTCCATTTTATGCGCTGCTGCGTCTACCTTTC Reverse : GAAAGGTACGCAGCAGCGCATAAAATGGAAATCAAGCCCAG

Table 3. PCR cycle parameters used for site-directed mutagenesis.

Steps	Temeprature	Time	Cycles
Initial denaturation	95°C	30 sec	1
Denaturation	95°C	30 sec	12-18
Annealing	60°C	1 min	
Extension	68°C	1 min/kb of plasmid length =12 kb	

3.2.5 Transformation of super competent XL1-blue cells

Heat shock chemical transformation was performed as follows. After 30 min incubation on ice with the cDNA, the competent cells were heated at 42°C for 25 sec and placed on ice for 2 min. Then, 800 µL of LB medium was added and the cells were incubated for 1 hour at 37°C, shaking at 220 rpm. After pelleting, transformed bacteria were resuspended in a small volume of LB, plated in LB-agar plates containing 100 µg/mL ampicillin and incubated ON at 37°C. Individual bacterial colonies were picked and cultivated in 4 mL of LB ampicillin for mini-prep plasmid DNA isolation. Plasmid DNA was isolated using NucleoSpin Plasmid kit. To confirm that the transformation of supercompetent cells and the isolation of plasmid DNA have been carried out successfully, 1 µg of plasmid DNA was mixed with 1 µg of EcoRI-HF and NotI-HF in CutSmart® (10 x) buffer. Digestion was carried out at 37°C for 1h. The samples were

analyzed on a 1 % agarose gel with electrophoresis at 60V. The agarose gel was stained with EB for 10-15 minutes, then washed with $MgSO_4$ for 10-15 minutes. Samples were sent to Eurofins for whole plasmid sequencing to verify the constructs.

3.2.6 Yeast transformation

The lithium acetate method was used to transform yeast (Zheng et al., 2005) (Gietz & Schiestl, 2007). Briefly, 5 mL of S6AU medium supplemented with 2 % (w/v) glucose, 20 µg/mL adenine and 20 µg/mL uracil was inoculated with one yeast colony for 24 h at 28°C with shaking at 180 rpm. 2 mL of the above culture was centrifuged (5 min at 5,000 x g), and 50 µL of 2 mg/mL salmon sperm DNA (SSD), previously denatured at 100°C for 5 min and cooled down on ice, plus ~1 µg of the plasmid DNA was added to the yeast pellet. After vortexing, 500 µL of plate buffer (40 % (w/v) PEG 4,000, 100 mM lithium acetate, 10 mM Tris-HCl pH=7.5, 1 mM EDTA and 1 M DTT was added. The mixture was vortexed and incubated O/N at room temperature. The following day, the cell suspension was centrifuged at 5,000 x g for 4 min and the pellet was resuspended with a small volume of selective medium. The resuspended pellet was plated on a selective S6A agar plate (with 20 µg/mL adenine and without uracil) and incubated for 3-5 days at 28°C.

3.2.7 Protein expression

3.2.7.1 In small-scale cultures

5 mL S6A medium was inoculated with freshly transformed yeast colonies and left for 24h at 28°C with shaking at 180 rpm. An appropriate amount of this preculture was added to 20 mL YPGE2X medium to achieve an OD_{600} of 0.05, and incubated for 36 h at 28°C with shaking at 180 rpm until reaching a cell density of OD_{600} between 3 and 5. Cultures were then centrifuged in sterile tubes (10 min at 4,000 x g, 4°C), and the pellet resuspended in 20 ml of YPE2X medium supplemented with 2% (w/v) galactose

to induce protein expression. After 13 h incubation at 18°C with shaking at 180 rpm, another 2 % (w/v) of galactose was added. After 5 h of the second induction, cells were recovered after centrifugation (10 min at 4,000 x g, 4°C), resuspended in 2 mL of TEKS buffer per gram of pellet and incubated at 4°C for 15 min. Finally, the cell pellet was recovered again after centrifugation (10 min at 4,000 x g, 4°C), flash-frozen with liquid nitrogen, and stored at -80°C.

3.2.7.2 In large-scale cultures

500 mL of YPGE2X medium was inoculated with an appropriate volume of preculture to achieve an OD_{600} of 0.05 and incubated for 36 h at 28°C with shaking at 130 rpm. After 36 h, the flasks were placed on ice for 20-30 min in order to drop the temperature, and protein expression was induced by addition of 2% (w/v) of galactose. After 13h of induction at 18°C with shaking at 130 rpm, a second induction with another 2% (w/v) of galactose was performed and the cultures were left for a further 5h at 18°C with shaking at 130 rpm. The cell pellet obtained after centrifugation (10 min at 4,000 x g, 4°C), was washed with milli-Q® H_2O. Finally, cell pellets were resuspended in 2 mL of TEKS buffer per gram of cell pellet and incubated at 4°C for 15 min. Cell pellets were recovered after centrifugation, flash-frozen with liquid nitrogen, and stored at -80°C.

3.2.8 Membrane preparation

3.2.8.1 From small-scale cultures

Cell pellets obtained from small-scale culture were resuspended in 1 mL TES buffer per gram of cell pellet supplemented with EDTA-free PIC (1X) and 1 mM PMSF. Cells were transferred to 2 mL eppendorfs and an equal volume of glass beads (0.5 mm diameter) was added. The cells were then broken by vortexing the eppendorf for 20 min at 4°C. Beads and non-broken cells were pelleted after centrifugation was performed (5 min at 1,000 x g, 4°C). The beads were washed and centrifuged again. Total membranes

were obtaining after ultracentrifugating the supernatants (1h at 145,000 x g, 4°C). Finally, membranes were resuspended in 0.2 mL of HEPES-sucrose buffer per gram of cell pellet, flash-frozen in liquid nitrogen and stored at -80 °C.

3.2.8.2 From large-scale cultures

Cell pellets were thawed and resuspended in 1 mL TES buffer per gram of pellet, supplemented with EDTA-free PIC (1X), and 1 mM PMSF. Cells were then broken using glass beads (0.5 mm diameter) in a Planetary Mono Mill PULVERISETTE 6. The system to grind the samples was set as follows : 450 rpm during 3 min, pause for 30 sec, then 450 rpm during 3 min in the reverse sense. The broken crude extract was recovered and the beads were washed with 1.5 mL of ice-cold TES buffer per gram of cell-pellet. The pH of the crude extract was maintained at 7.5 to avoid endogenous proteolysis from vacuolar proteases. Cell debris, unbroken cells and glass beads (designated as P1) were removed by centrifugation (20 min at 1,000 x g, 4 °C) (**Figure 23**). The resulting supernatant (designated as S1) was subjected to a second centrifugation (20 min at 1,000 x g, 4°C) to obtain the second pellet (designated as P2) containing the heavy membranes. The supernatant (designated as S2) was subjected to ultracentrifugation (1h, 125,000 x g, 4°C). The resulting pellet (designated as P3), containing light membranes, was resuspended in 0.2 mL HEPES-sucrose buffer per gram of cell pellet. Resuspended P2 and P3 membranes were flash-frozen in liquid nitrogen and stored at -80 °C.

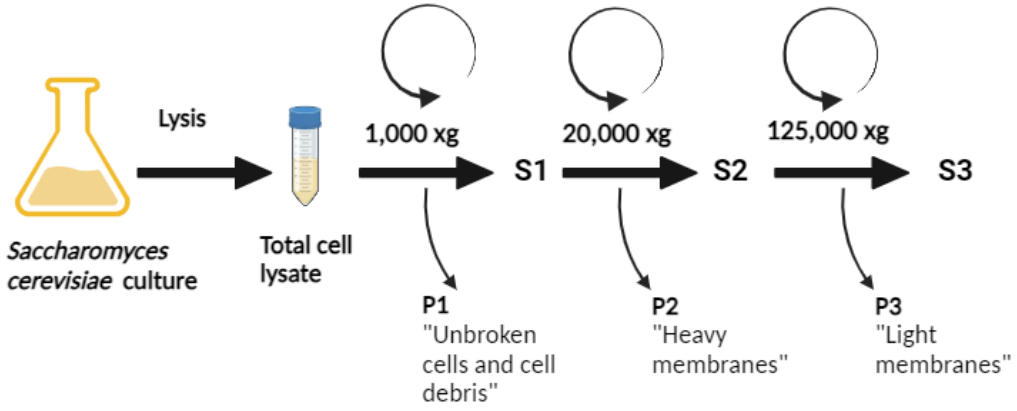

Figure 23. Preparation of the *S. cerevisiae* membranes. The total cell lysate obtained from the *S. cerevisiae* cultures were subjected to an initial low-speed centrifugation to remove unbroken cells and cell debris. Next, the first supernatant (S1) was subjected to a second medium-speed centrifugation to obtain the heavy membranes (P2). Next, the second supernatant (S2) was subjected to high concentration to obtain the light membranes (P3) and the third supernatant (S3).

3.2.9 Measurement of the total protein concentration in membranes and purified proteins

Total protein concentration of P3 membranes was measured by the BiCinchoninic acid Assay (BCA) and the concentration of purified protein was measured at absorbance of 280 nm using a Thermo Fisher Scientific™ NanoDrop™. The BCA assay is a variant of the Biuret reaction in which, under basic conditions, peptide bonds in proteins reduce $Cu2^{+}$ to Cu^{+} (**Figure 24**). Two molecules of BCA then interact with Cu^{+} to form a violet-coloured BCA-Cu complex, which strongly absorbs light at a wavelength of 562 nm (Smith et al., 1985). The calibration curve consisted on a serial dilution (2-1-0.5-0.25-0.125-0.0625 mg/mL) of bovine serum albumin (BSA) in milli-Q® H_2O. For samples P2 and P3, a 1/40 dilution was carried out. On a 96-well microplate, 10 µL of each standard dilution of BSA and blank (milli-Q® H_2O) were added. Then, 10 µL and 5 µL of membrane samples were added. Next, 200 µl of BCA working solution was added to each well. Each data point was done in triplicate. The microplate was incubated for 30 minutes at 37°C with shaking at 150 rpm. Absorbance was measured

at 562 nm using the BioTek Epoch 2 microplate Reader. The protein concentration of the sample was determined according to the standard curve of known concentrations of BSA.

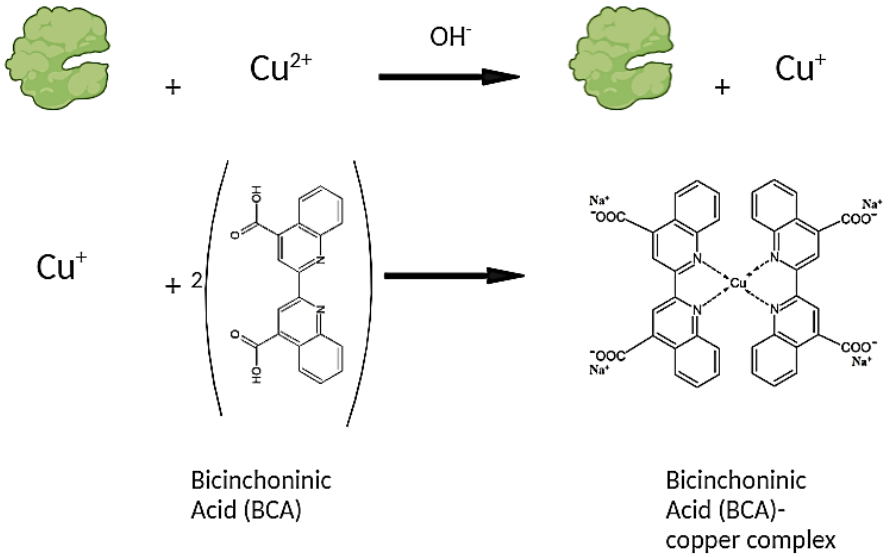

Figure 24. The BCA assay consists of two reactions. Firstly, the peptides in the proteins reduce Cu^{2+} to Cu^{+}. The amount of Cu^{2+} reduced is proportional to the total amount of protein in the sample. Secondly, 2 molecules of BCA react with Cu^{+} to form a violet BCA-Cu^{+} complex with an absorbance of 562 nm, Adapted from (Smith et al., 1985).

3.2.10 Fluorescent confocal microscopy

1 mL of a small-scale fresh yeast culture, was centrifuged (5 min at 2,000 x g) and washed twice with 1 mL PBS (pH=7.4). Cells were then resuspended in 1 mL PBS (pH=7.4). A square is cut in a piece of parafilm and this piece is put on a glass slide (**Figure 25**). The parafilm serves as frame to cast the agarose pads (1 % (w/v) agarose in milli-Q® H_2O). The 2 µl of induced *S. cerevisiae* cells were deposited on the top of the pad. Then a coverslip was placed on the top of the pad and sealed with nail polish. Fluorescent images were taken with a Leica TCS SP8 multiphoton (MP). The microscopy is equipped with a HC PL APO 63x/1.40 OIL objective, at excitation and emission

wavelengths of 488 and 580 nm, respectively. Images acquisition and processing were carried out using LasX and FijiJ softwares, respectively. Fluorescent confocal microscopy was performed at the Light Microscopy Facility (I2BC).

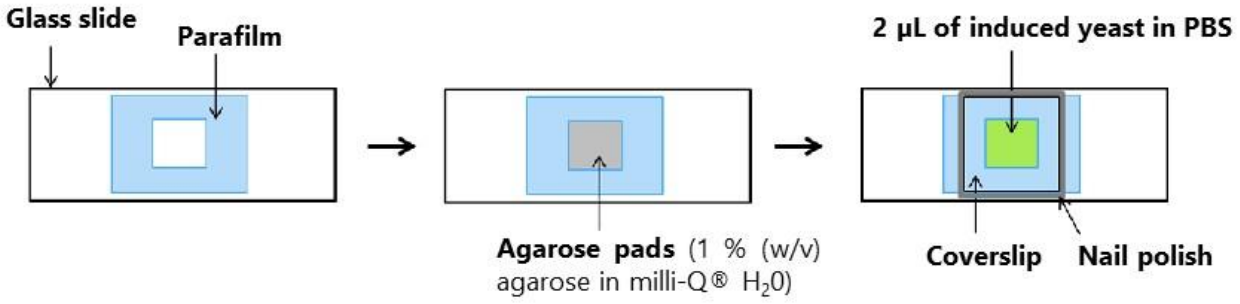

Figure 25. Scheme of the assembly of the slide containing *S. cerevisiae* cells for confocal microscopy analysis, adapted from (*Anaïs Lamy., et al., 2018*).

3.2.11 Expression and purification of GFP-targeted nanobodies (nanoGFP)

Nanobodies are the trademark of of the antigent binding fragment VHH derived from the single-domain (heavy chain) of camelid antibodies (**Figure 26**). His-tagged anti-GFP nanobodies (nanoGFP) were produced in *E. coli* for subsequent use in the affinity purification of PQLC2. Competent BL21-DE3 *E. coli* cells were transformed with pOPINE-nanoGFP-His vector (Addgene reference #49172; Kubala et al., 2010). 10 ml of transformed cells were incubated O/N at 37°C. in LB media supplemented with 100 µg/mL of ampicillin. 500 mL LB with ampiciline was inoculated with 4 mL of the preculture and incubated at 37°C with shaking at 180 rpm. When the OD reached ~0.6, the culture was placed on ice for 30 min. Protein expression was induced with 1 mM IPTG, incubating the cells for 20-24h at 20°C with shaking at 150 rpm. The cell pellet was recovered after centrifugation (10 min at 6,000 x g, 4°C), flash-frozen in liquid nitrogen and stored at -80 °C. Purification of nanoGFP was carried out as follows. The bacterial pellet corresponding to 500 mL culture was resuspended in 10 mL lysis buffer

and incubated for 1h at 4°C on a rotary shaker. Cells were broken by sonication using Vibra-Cell™ 75041 sonicator (6 cycles of 1 min: 10 sec on and 10 sec off, amplitude 40%, keeping cells always on ice). Cell debris and non-broken cells were removed by centrifugation (20 min at 2,000 x g, 4°C), and the supernatant incubated for 1h at 4°C with 1 mL of TALON® metal affinity beads previously equilibrated with 10 column volumes (CV) of lysis buffer. After incubation, the beads were washed in three steps: 20 mL lysis buffer, 10 mL lysis buffer with 20 mM imidazole, and 10 mL lysis buffer with 30 mM imidazole. The nanoGFP was eluted in 2 steps by adding 5 mL of lysis buffer and 150 mM imidazole followed by 5 mL of lysis buffer and 300 mM imidazole. The two fractions were combined, and concentrated using a 5 KDa Vivaspin® 20 concentrator. Concentrated nanoGFP were dialyzed O/N at 4°C againts 1 L of PBS to remove imidazole. Dialized nanoGFP was stored at -20°C after supplementing with 20% (v/v) glycerol.

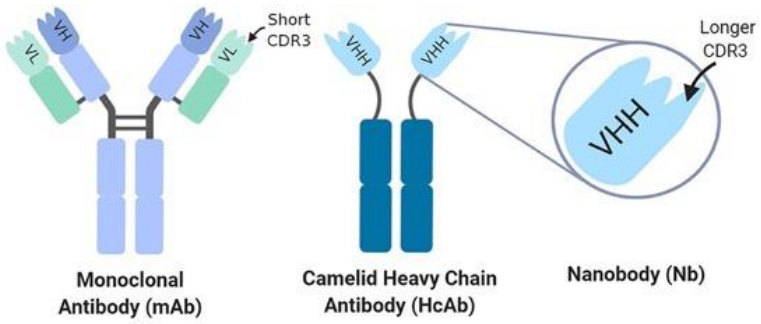

Figure 26. Comparation between standard (left) and camelid (right) antibodies. Nanobodies are the variable domain (VHH) of heavy-chain-only antibodies, characteristic of the Camelidae family. The molecular weight of nanobodies is around 15 kDa**.** The detailed description of nanobody generation is described in this review (Jin et al., 2023, p. 4,5,6).

3.2.12 Coupling purified nanoGFP to agarose beads

Coupling of purified nanoGFP to N-hydroxysuccinimide (NHS)-Activated Sepharose 4 Fast Flow agarose beads was carried out as previously described (Lamy et al., 2021) (Rothbauer et al., 2008a). The ratio of NHS-Activated Sepharose 4 Fast Flow resin to purified nanoGFP was recommended at 1/0.5 (v/v); that is, 1 mL NHS-Activated Sepharose 4 Fast Flow resin per mg purified nano-GFP. 1 mL of NHS-Activated Sepharose 4 Fast Flow resin was added to a plastic column and washed excessively with milli-Q® H_2O to remove all traces of isopropanol. The resin was washed with 10 CV of HCl and equilibrated with another 10 CV of PBS (pH=7.5). Thereafter, 1 mg of nanoGFP was added to the 1 mL resin and incubated at 4°C O/N under gentle rotation. The volume of the nanoGFP added was kept always between 0.5 to 0.7 mL in order to comply with volume ratio nanoGFP/resin of the reaction. The next morning, the flow-through was discarded and the non-reacted sites of the resin were blocked by incubation with 10 CV of 0.1 M Tris-HCl (pH=8.5) for 4 h at 4°C with gentle rotation. The flow-through was discarded and the resin was subjected to 3 successive wash cycles as follow: 3 CV of 0.1 M Tris-HCl, 0.5 M NaCl (pH=8.5) and 3 CV of 0.1 M acetate buffer, 0.5 M NaCl (pH=5.0). Finaly the resulting GFP-Trap beads were stored at 4°C, ready for use for up to 2 weeks in PBS.

3.2.13 Detergent screening and fluorescence-detection size-exclusion chromatography

P3 membranes at a final protein concentration of 5 mg/mL were solubilized for 1h and at 4°C in 1% of either, DDM, DM, NG or LMNG, supplemented with 0.2 % (w/v) cholesteryl hemisuccinate (CHS). In all cases, buffer composition was as follows: 20 mM Tris-HCl pH 7.5, 150 mM NaCl, 10 % (v/v) glycerol, 5 mM MgCl2, EDTA-free PIC (1X), 1 mM PMSF. After solubilization, samples were ultracentrifuged (1h at 145,000 x g, 4°C), and 400 µL of the detergent-solubilized supernatant was injected into a Superose 6 increase 10/300 GL column equilibrated with 20 mM Tris pH 7.5, 150 mM NaCl, 10 % (v/v) glycerol and 0.02 % (w/v) DDM. Fluorescence-detection size-exclusion

chromatography (FSEC) experiments were performed in an ÄKTA purifying chromatography system connected to a fluorescence detector (Jasco FP-4025). GFP fluorescence was measured using excitation and emission wavelengths of 470 and 510 nm, respectively. UNICORN software was used to monitor and record the chromatograms.

3.2.14 Purification of PQLC2 by affinity chromatography using nanoGFP traps.

20 ml of P2 or P3 membranes expressing PQLC2-GFP at a final total protein concentration of 5 mg/mL were solubilized for 1h in 1% (w/v) DDM/ 0.2% (w/v) CHS, 20 mM Tris-HCl pH=7.5, 150 mM NaCl, 10 % (v/v) glycerol, 5 mM $MgCl_2$, EDTA-free PIC (1X) and 1 mM PMSF. The insoluble fraction was removed by ultracentrifugation (1h at 145,000 x g, 4°C). The DDM-solubilized supernatant was incubated for 2h at 4°C with GFP-Trap beads (see **Figure 27** for the flow chart of purification using nanoGFP trap beads). (Lamy et al., 2021) previously equilibrated with 5 CV of column buffer. After incubation, the flowthrough was collected and the beads were washed with 20 CV of column buffer followed by 3 CV of eluting buffer. To elute PQLC2, the beads were incubated O/N at 4°C with 2 CV of eluting buffer supplemented with 40 units (40 µg) of Hrv-3C protease. The eluted fraction was recovered and concentrated by centrifugation using Vivaspin® 20 100 kDa concentrator and analysed by SDS-PAGE and Coomassie blue staining.

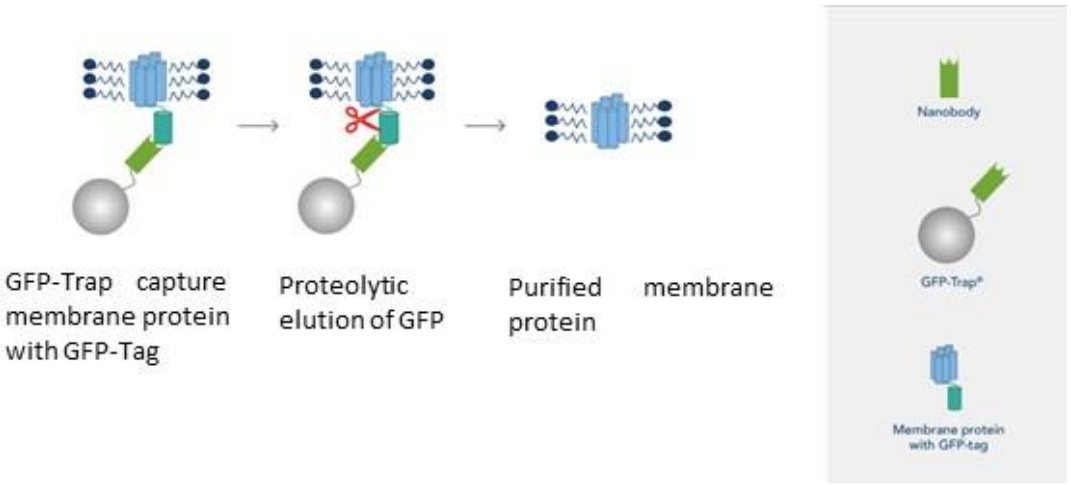

Figure 27. Flow chart of purification using nanoGFP trap beads, adapted from GFP-Trap®, ChromoTek.

3.2.15 Protein detection by SDS-PAGE and western Blot

For protein detection, samples were then subjected to electrophoresis on 4-15% precast Mini-PROTEAN® gels (Laemmli, 1970). Membranes containing a defined total protein concentration or purified protein samples were mixed with loading buffer (2X) and incubated for 10 min at 30°C (Soulié et al., 1996). Migration in SDS-PAGE was performed to a constant voltage of 150 volts. For Coomassie Blue staining, the gels were incubated for 1h at room temperature in the Coomassie blue staining solution, followed by several washing steps using a destaining buffer. The gels were then dried with fixation buffer using GelAir Cellophane support. For western blot assays, proteins from the SDS-PAGE gel were transferred into PVDF membrane (1h/ 100 V). The membranes were then blocked in blocking solution for 1h at room temperature. PQLC2 was detected using two strategies (**Table 4**). GFP-tagged PQLC2 were detected with a mouse anti-GFP antibody. PQLC2 was also detected using rabbit anti-PQLC2 antibody targeting the cytoplasmic loop between TMs 5 and 6. Primary antibodies were detected after incubation with either, anti-mouse or anti-rabbit Horseradish peroxidase (HRP) secondary antibody (see **Table 4** for full description). The ECL Select™ Western Blotting Detection kit was used for western blot revelation and luminescence was

detected by a CCD camera using GeneSnap software for image acquisition. All blue Precision Plus Protein™ Prestained Standard (Bio-Rad) was the molecular weight marker used in all experiments.

Table 4. Target and dilution factor of the different antibodies used in the Western blot assay.

Target	Primary antibody	Dilution of primary antibody	Secondary antibody	Dilution of secondary antibody
GFP	Mouse anti-GFP antibody	1:1000	Goat anti-mouse IgG-HRP antibody	1:3000
PQLC2 cytoplasmic loop (1-8)	Rabbit anti-PQLC2 antibody	1:1000	Goat anti-rabbit IgG-HRP antibody	1:3000

3.2.16 Protein detection by Native PAGE

For Native PAGE, samples were subjected to electrophoresis on 4-15 % Mini-PROTEAN® Precast gels or 16.5 % Mini-PROTEAN® Tris-Tricine gels under native conditions. Samples were mixed with Native loading buffer (2X) without heating the samples. Migration in native PAGE running buffer (1X) was set at a constant voltage of 100 volts at 4°C. Dual Xtra Precision Plus Protein™ standard (Bio-Rad) was the molecular wieght marker used. Gels were incubated for 1 h at room temperature in Coomassie Blue staining solution, followed by several washing steps using a destaining buffer. The gels were then dried with fixation buffer using GelAir Cellophane support. The fluorescence of Cy3 coupled to the N-terminus of WDR41-7CD peptide was detected using the ChemiDoc (Bio-Rad) imaging system.

3.2.17 Thermostability assays

3.2.17.1 17.1. Thermostability of purified PQLC2 using CPM

The protein/dye mixture is heated to thermally denature the protein, exposing the embedded cysteines of the protein and allowing them to react with the CPM (**Figure 28**) (Sampson et al., 2021). A 10 mM stock solution of CPM in DMSO was diluted up to 200 µM in the reaction buffer (working solution), and kept on on ice during 10 min protected by aluminium foil to prevent photobleaching. An appropriate volume of the CPM working solution (10 µM final concentration) was mixed with 1 µM of purified PQLC2 and transferred to a Quartz fluorometer cuvette. The sample was equillabrated for 5 min at 20°C before starting the experiment. CPM fluorescence was then recorded between 20 and 75 °C at interaval of 5 °C using a Horiba Fluorolog Spectrofluorimeter. The excitation and emission wavelengths of CPM are 387 nm and 463 nm, respectively.

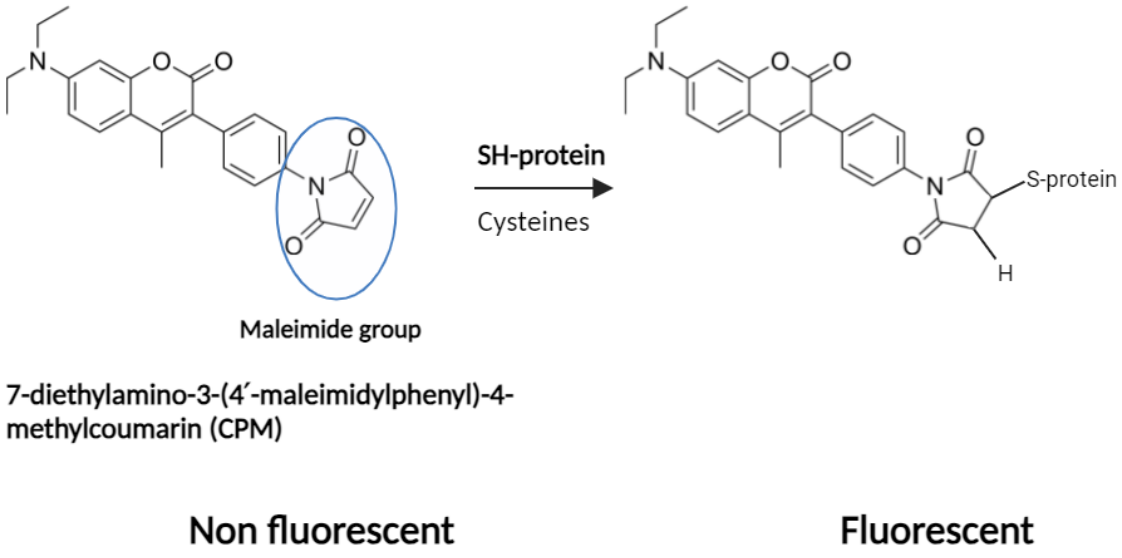

Figure 28. CPM reaction to cysteine. The CPM dye on the right contains a maleimide group which reacts with the thiol group of the protein to form a fluorescent complex.

3.2.17.2 17.2. Thermostability of GFP-PQLC2 using FSECm

P3 membranes of PQLC2 (LL/AA) or consensus with a final protein concentration of 5 mg/mL were solubilized with 1 % (w/v) of DDM supplemented with 0.2 % (w/v) CHS, at 4°C. After solubilization, samples were incubated at different temperatures; 4°C, 45°C and 70°C for 1h followed by ultracentrifugation (30 min at 145,000 x g, 4°C), and 400 µL of detergent-solubilized supernatant was injected into a Superose 6 increase 10/300 GL column equilibrated with 20 mM Tris pH 7.5, 150 mM NaCl, 10 % (v/v) glycerol and 0.02 % (w/v) DDM. FSEC was performed as previously described.

3.2.18 Quantification of PQLC2-GFP in membranes using GFP fluorescence

The principle of protein quantification is based on the GFP tag fused to the C-terminus of PQLC2, where the amount of protein in the P2 and P3 membranes of PQLC2 is quantified using purified GFP as reference.

To obtain purified GFP to build the calibration curve, the cDNA encoding a superfolder GFP tagged with the His tag at the C-terminal end was inserted into the pTTQ18 plasmid. *E. coli* BL21 cells were transformed with this plasmid and GFP expression was induced for 12h at 37°C, after adding 0.5 mM IPTG to the bacterial culture after reaching OD_{600} ~0.6. The GFP was purified by affinity chromatography using TALON® Superflow following an identical protocol as for the nanoGFP (see section **material and methods**). The purified GFP is the same version as the GFP fused to the C-terminus of PQLC2.

P2 and P3 membranes of PQLC2 were solubilized in 0.6 % or 0.9 % (w/v) DDM in protein quantification buffer (10 % (v/v) glycerol, 0.15 M NaCl, 0.1% (w/v) DDM, 0.02 M Tris-HCl (pH=7.8)). The calibration curve consists of a serial dilution of increasing amounts of purified GFP (0 ng, 5.2 ng, 10.4 ng, 20.9, 31.3 ng, 52.2 ng, 83.5 ng, 125.3 ng). Samples were deposit in a 96-well microplate (Thermo Scientific™ Nunc MicroWell polymer-based) and GFP fluorescent was quantified in a TECAN GENios fluorescence plate

reader. The excitation and emission wavelengths were 485 nm and 535 nm, respectively.

3.2.19 Negative staining electron microscopy (NS-EM)

Purified PQLC2 in DDM obtained by affinty chromatography was concentrated and then injected in a Superose 6 increase 10/300 GL column (GE, Healthcare) equilibrated with 20 mM Tris pH 7.5, 150 mM NaCl, 10% (v/v) glycerol and 0.015% (w/v) LMNG. Eluted fractions of PQLC2 were collected and used for NS-EM without further concentration. A total of 3 µL of purified PQLC2 (~0.1 mg/mL) was added on the top of an incandescent-discharged carbon-coated copper grids and stained twice with 3 µL of 2% uranyl formate solution. Micrographs were taken using a Tecnai Spirit transmission electron microscope (FEI) operating at 100 kV. Imaging was carried out at 4400 magnification with a Gatan K2 camera (pixel size of 1.26 Å). The experiments were carried out in the cryo-electron microscopy facility at I2BC (Gif-sur-Yvette).

3.2.19.1 2D classification of NE-EM

We used Cryosparc (v4.6) to analyze NS-EM micrographs of PQLC2 (see **Table 5** for Cryosparc parameters). To obtain 2D classes we employed three different strategies while selecting the particles. First, we used a Manual picking. In this strategy, 1,289 particles were manually selected from 107 micrographs, with a specific box size of around 8 nm. The contrast transfer function (CTF) was automatically estimated for each particle in the different micrographs. After 2D classification, 12 were selected, 38 were excluded. The total amount particles considered for the selectes classes was around 733 (57 %). In a second strategy, 95,409 particles were selected by blob picking of determined box size (16 nm). As in the previous method, the CTF was automatically estimated for each particle in the different micrographs and a 2D classification was then performed. 10 classifications were selected, and 40 were excluded, (i.e. around

732 particles selected (58 %)). In the third strategy, 13828 particles were selected according to an inserted template (Template picking), obtained from manual picking particles of around 8 nm. The particles were inspected manually and the CTF was automatically estimated for each particle in the different micrographs. The 2D classification was then performed and 20 classes were selected (i.e. around 12216 particles selected).

Table 5. NS-EM and Cryosparc parameters.

Data collection and processing	**Parameter value**
Voltage (kV)	100
Pixel size (Å)	1.26 Å
Spherical aberration (mm)	2.2
Electron exposure (e-/Å2/frame)	40
Box size (nm)	16

3.2.20 Site-directed spin-labeling (SDSL) of WDR41-7CD loop

Both, single and double cysteines-containning WDR41-7CD loop peptides were labeled with a nitroxide-based spin labels for subsequent EPR experiments (**Figure 29, Table 6**). 20 µM of synthetic WDR41-7CD loop peptide (Eurofins) in 25 mM MES (pH=7.5) was incubated for 10 min with TCEP to ensure that all cystine-thiol groups were reduced before labeling. Then, 1 mM 3-Maleimido-PROXYL was incubated with the peptide solution for 1 h at RT. To clean up free 3-Maleimido-PROXYL we used Pierce™ Strong Cation Exchange columns.

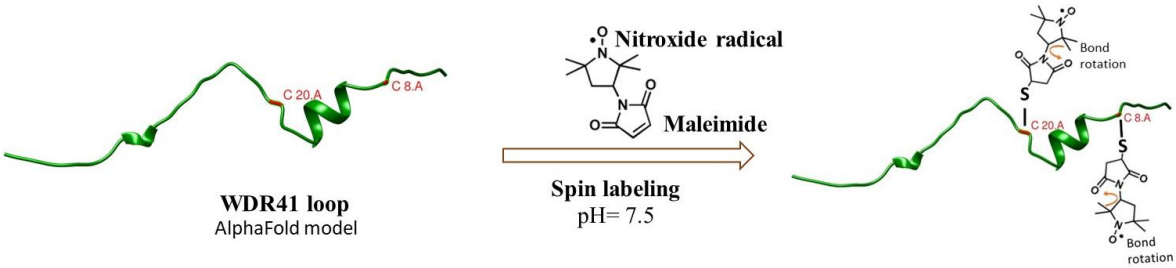

Figure 29. Site-directed spin-labeling (SDSL) of WDR41-7CD loop. The synthetic WDR41-7CD loop peptide containing cysteines residues in defined postions was incubated with 3-Maleimido-PROXYL in order to introduce the nitroxide-based spin label at suitable positions within the WDR41-7CD loop peptide (right).

Table 6. Different WDR41-7CD loop peptides used in the EPR experiments. One and two cysteines residues (in red) were introduced at different positions for spin-labeling. WDR41-7CD loop amino acids found to be essential for PQLC2 binding are highlighted in gray (Talaia et al., 2021). Mutations introduced into the essential site of WDR41-7CD loop are in bold.

Peptide name	Sequence	Label
CD1 - G22C	KQQLAAEPVPTGFFNMWGFGR**C**NKQANQPVKKQEENVTT	Single label
CD2 - G20C	KQQLAAEPVPTGFFNMWGF**C**RVNKQANQPVKKQEENVTT	Single label
CD3 - A6C and V22C	KQQLA**C**EPVPTGFFNMWGFGR**C**NKQANQPVKKQEENVTT	Double label
CD4 - P8C and V20C	KQQLAAE**C**VPTGFFNMWGF**C**RVNKQANQPVKKQEENVTT	Double label
CD5 - P8C, F14A and V20C	KQQLAAE**C**VPTG**A**FNMWGF**C**RVNKQANQPVKKQEENVTT	Double label
CD6 - P8C, F13A, W17A and V20C	KQQLAAE**C**VPTG**A**FNM**A**GF**C**RVNKQANQPVKKQEENVTT	Double label
CD7 - A6C	KQQLA**C**EPVPTGFFNMWGFGRVNKQANQPVKKQEENVTT	Single label
CD8 - P8C	KQQLAAE**C**VPTGFFNMWGFGRVNKQANQPVKKQEENVTT	Single label
CD9 - P8C, F13A and F17A	KQQLAAE**C**VPTG**A**FNM**A**GFGRVNKQANQPVKKQEENVTT	Single label

3.2.21 Electron paramagnetic resonance (EPR) spectroscopy measurements and data analysis.

The sample was loaded into capillary tubes at a final volume of 16 µL per experiment.

Several EPR measurements were carried out: (i) WDR41-7CD loop peptides (31 µM), (ii) PQLC2 (35 µM) with labeled WDR41-7CD loop peptide at a molar ratio of 1 : 0.9 (PQLC2/peptide), (iii) a competition experiment with unlabeled WDR41-7CD loop peptide at a molar ratio of 1 : 0.9 : 5 (PQLC2/labeled peptide/unlabeled peptide), (iv) addition of 100 mM L-Arg at a molar ratio of 1 : 0.9 (PQLC2/labeled peptide).

EPR spectra obtained on a Bruker Elexys500 X-band spectrometer in unsaturated condition at 293 K with 1 G frequency modulation. The spectra were simulated on Matlab using the easyspin toolbox (Stoll & Schweiger, 2006).

3.2.22 Reconstitution of PQLC2 into liposomes

PQLC2 was reconstituted in liposomes containing a phospholipid mixture of DOPC/ DOPE of 4 : 1 (w:w) (see the scheme of the protocol in **Figure 30**). Lipids were solubilized in chloroform in a round-bottom flask. Chloroform was them evaporated in a rotary evaporator to form a thin layer of dry phospholipids. To remove all traces of the organic solvent, the flask was placed in the vacuum for a few hours. The DOPC/DOPE lipid layer was then resuspended in 2 ml of reconstitution buffer to obtain a final lipid concentration of 10 mg/mL of multilamellar vesicles (MLV). The MLV were then subjected to five cycles freezing in liquid nitrogen and thawing (30 sec in liquid nitrogen, 2 min in water bath). Unilamelar vesicles (ULV) were obtained after extruding the MLVs ten times through 400 nm polycarbonate filters a using using Avanti Mini Extruder (Avanti research). Samples were then diluted up of 4 mg/mL of lipids. To partially destabilize the lipid bilayer, liposomes were solubilized with Triton X-100 in a 1 : 15 (w /w) ratio (lipids to detergents) after O/N incubation at room temperature and under gentle rotation. Purified, detergent-solubilized PQLC2 was added to detergent-destabilized liposomes at a protein/lipid ratio of 1 : 10 (w/w) and incubated for 1h at 4°C under gentle rotation. Triton X-100 was then removed by incubation with polystyrene beads Bio-Beads™ at a ratio of 1 : 30 (w/w) detergent/biobeads respectively for 3h at 4°C with gentle rotation. The Bio-Beads™ were previously

activated as follows: 1h incubation in methanol which was repeated twice, then ON incubation with ethanol at room temperature. Then, the Bio-Beads™ were washed thoroughly before use. After removal of the detergent, ultracentrifugation was performed (30 min at 145,000 x g, 4°C). The pellet was resuspended in one-third of the initial volume of reconstitution buffer without amino acids. Liposomes (protein-free or empty) were prepared in a similar way, but without incubation with PQLC2. Both proteoliposomes and liposomes were freshly prepared before the transport experiment.

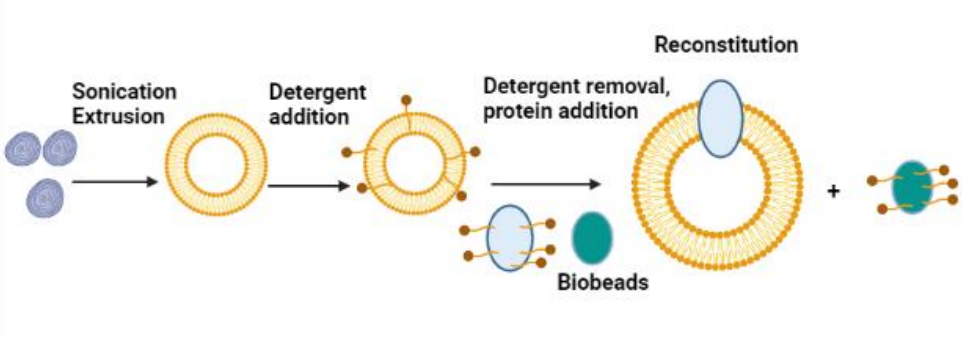

Figure 30. Schematic representation of reconstitution of purified PQLC2 into liposomes. Multilamellar vesicles (MLV) were extruded in order to form unilamellar vesicles (ULV). Detergent was added to the ULV to partially distabilize the lipid bilayer before mixing with the detergent-purified PQLC2. Finally, Bio-Beads™ were added to remove the detergent.

3.2.23 Dynamic light scattering (DLS) measurements.

DLS was performed to evaluate the proteoliposome and liposome size distribution. 50 µL of either protein-free or PQLC2-reconstituted liposomes at a lipid concentration of 4 mg/mL in reconstituion buffer were analyzed using a Zetasizer DLS at room temperature. Data processing was carried out using Excel or Nano v3.30 software supplied with the equipment. Measurements were carried out automatically in triplicate.

3.2.24 Density-based separation of proteoliposomes by glycerol gradient

To assess reconstitution efficiency and determine whether the protein has been incorporated into the liposomes, proteoliposomes were loaded onto a glycerol gradient (Verchère et al., 2014).

The glycerol gradient was prepared in glass test tubes with increasing concentrations of glycerol (5 %, 10 %, 20 %, 30 %, 40 %, 50 % (v/v)) along with 0.05 % (v/v) Triton. The glycerol gradient was placed at 37°C for 1h, then 100 µL of proteoliposomes and liposomes (4 mg/mL) were carefully loaded onto the top of the gradient. The gradient was then ultracentrifuged (O/N at 100,000 x g, 4°C) with minimal acceleration and deceleration rates. Carefully the various gradient fractions were collected and analyzed by Western blot.

Aggregated proteins are found at the bottom of the tube. Proteoliposomes and liposomes are found at sucrose interfaces corresponding to their intrinsic density. Empty liposomes are collected higher up the gradient than proteoliposomes.

3.2.25 Transport assay of PQLC2 in proteoliposomes

Freshly-prepared proteoliposomes in reconstituting buffer at a lipid concentration of 4 mg/mL were incubated with 10 µM valinomycin on ice. Valinomycin is a potassium-selective ionophore that enables potassium to pass from one side of the membrane when a K^+ gradient is stablish across the membrne (**Figure 31**) by simply diluting the proteoliposomes in a K^+-free buffer a transient membrane potential (negative in the interior) is created. The uptake assay was initiated by adding 20 µL of proteoliposomes to 180 µL of transport buffer 1 (**Figure 32**). The mixture was vortexed and incubated at room temperature. At specific time periods (1, 2, 5, 10 and 30 min) the uptake was stopped by adding 1 mL of ice-cold stop buffer 1, followed by rapid filtration through nitrocellulose membrane filters (MF-Millipore™) with a pore size of 0.22 µm. The filters were washed with 2 mL of ice-cold stop buffer 1 and subsequently transferred into a

liquid scintillation vial. The trapped radioactive substrate in the proteoliposomes was measured using a Tri-Carb® liquid scintillation analyzer. Measurements were taken in triplicate for each data point.

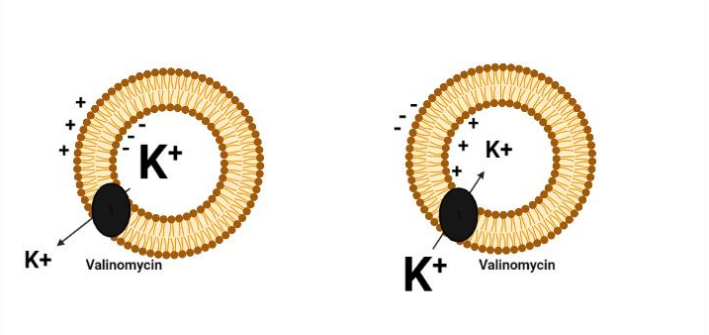

Figure 31. Generation of a transient membrane potential in liposomes. When valinomycin-containing liposomes are exposed to a K^+ concentration gradient across the membrane there is a rapid flux of K^+ ions down the concentration gradient, generating a transient transmembrane potential.

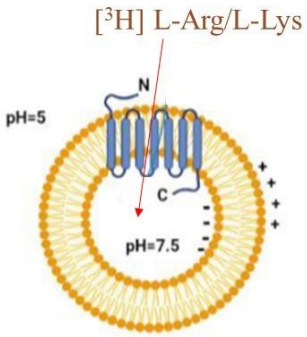

Figure 32. Schematic representation of the transport assay of PQLC2 reconstituted in liposomes. The pH outside the proteoliposome is acidic (pH=5), mimicking the lysosomal lumen, and the pH inside is neutral (pH=7.5), mimicking the lysosomal cytosol. PQLC2 is represented by 7 transmembrane domains, with the N-terminus oriented towards the cytosol and the C-terminus towards the lumen. The accumulation of radioactively-labelled L-Arg (^{3}[H]-Arg$^+$) or ^{3}[H]-Lys$^+$ transported by PQLC2 from the cytosol to the lumen is monitored.

3.2.26 Expression and purification of arginine/agmatine antiporter (AdiC)

3.2.26.1 Expression

Competent BL21-DE3 *E. coli* cells were transformed with pTTQ18-His6-AdiC (Kowalczyk et al., 2011) (Casagrande et al., 2008) and incubated O/N in LB culture with 100 µg/mL ampicillin at 37°C. 500 mL LB was inoculated with 4 mL of the preculture and incubated at 37°C with shaking at 180 rpm. When cell density reached an OD_{600} ~ 0.6, the culture was placed on ice for 30 min. Protein expression was induced with 0.5 mM IPTG, incubating the cells O/N at 37°C with shaking at 180 rpm. The cell pellet was recovered after centrifugation (10 min at 6,000 x g, 4°C), flash-frozen in liquid nitrogen and stored at -80 °C.

3.2.26.2 Membrane preparation

Bacterial cell pellets were resuspended in 1 ml resuspension buffer 1 per 0.2 grams of cell pellet. Cells were lysed using a French pressure cell press at 1500 psi. Unbroken cells and cell debris were removed by centrifugation (20 min at 13,000 x g, 4°C). Membranes were recovered after the supernatant ultracentrifugation (1h at 45,000 x g, 4°C). The supernatant was removed and the membrane pellet resuspended in 1 ml of resuspension buffer 2 per gram of cell pellet. The resuspended pellet was homogenized and flash-frozen in liquid nitrogen and stored at -80°C.

3.2.26.3 Purification

AdiC membranes with a final protein concentration of 5 mg/mL were solubilized for 1h in 1% (v/v) DDM 20 mM Tris-HCl pH=7.5, 150 mM NaCl, 10 % (v/v) glycerol, 5 mM $MgCl_2$, EDTA-free PIC (1X) and 1 mM PMSF. The insoluble fraction was removed by ultracentrifugation (1h at 145,000 x g, 4°C) and the supernatant was incubated for 2h at 4°C with 1.5 mL of TALON® metal affinity beads previously equilibrated with column buffer (20 mM Tris-HCl pH=7.8, 200 mM NaCl, 10 % (v/v) glycerol, 0.01 % (v/v) DDM)

supplemented with 5mM imidazole. After incubation, the column was washed first with 20 CV of column buffer with 5 mM of imidazole followed by 20 CV of column buffer with 20 mM imidazole. AdiC was eluted twice with 10 CV of column buffer containing 200 mM imidazole. The eluted fraction was recovered and concentrated by centrifugation using Vivaspin® 20 100 kDa concentrator and analysed by SDS-PAGE and Coomassie blue staining.

3.2.27 Reconstitution

Total *E. coli* lipids were mixed with chloroform to a final concentration of 40 mg/mL in a round-bottomed flask (Kowalczyk et al., 2011) (Reig et al., 2007). The organic solvent was removed in a rotary evaporator (Reig et al., 2007) to obtain a thin layer of lipids. The round-bottomed flask was then placed O/N in a vacuum bell jar to remove all traces of solvent. The lipids were resuspended in TD buffer (20 mM Tris-HCl (pH=7.6), 150 mM NaCl, 4 mM L-Arg or no L-Arg) with the help of ultrasonic water bath to obtain a final lipid concentration of 40 mg/mL. MLV were then subjected to five cycles of freezing and thawing (30 sec in liquid nitrogen, 2 min in water bath). ULV were obtained after extruding the MLVs ten times throught 400 nm polycarbonate filters a using Avanti Mini Extruder (Avanti research). To partially destabilize the lipid bilayer, liposomes were solubilized with Triton X-100 at lipid/detergen ratio of 1 : 15 (w /w) and incubated O/N at 4°C under gentle rotation. Purified AdIC was mixed with the detergent-destabilized liposomes at a protein to lipid ratio of 1 : 100 (w/w). The detergents were then removed after 3h incubation with Bio-Beads™ at a ratio of 1 : 30 detergent/biobeads. The proteoliposomes were subjected to ultracentrifugation (1h at 45,000 x g, 4°C). The pellet was resuspended in one-third of the initial volume of TD buffer without amino acids.

3.2.28 Transport assay of AdIC in proteoliposomes

The uptake of L-Arg in proteoliposomes was initiated by adding 20 µl of proteoliposomes to 180 µl of transport buffer 2. The mixture was incubated at room temperature. At specific time periods (1, 2, 5, 10 and 30 min) the reaction was stopped by the addition of 1 mL ice-cold Stop Buffer 2 followed by rapid filtration through nitrocellulose membrane filters (MF-Millipore™) with a pore size of 0.22 µm. The filters were washed with 2 mL of ice-cold stop buffer 1 and subsequently transferred into a liquid scintillation vial. The trapped radioactive substrate in the proteoliposomes was measured using a Tri-Carb® liquid scintillation analyzer.

4 RESULTS

4.1 MAMMALIAN PQLC2 (LL/AA), EXPRESSED IN *S. CEREVISIAE*, IS LOCALIZED IN ENCLOSED VACUOLE-LIKE ORGANELLES

One of the limiting steps in the structural and functional characterization of membrane proteins is their production (normally as recombinant) and purification in sufficient quantity and quality (Junge et al., 2008) (Pandey et al., 2016) (S. M. Smith, 2011). Membrane proteins are considered difficult targets for structural and functional studies due to their hydrophobic nature (Carpenter et al., 2008). As they are embedded in a lipid bilayer, they need to be extracted from the membranes by detergents prior their purification (Helenius & Simons, 1975) (Banerjee et al., 1995). Protein instability after detergent extraction is a common issue of many membrane proteins, particularly the eukaryotic ones, hindering subsequent functional studies (Lin & Guidotti, 2009). Consequently, most lysosomal transporters (dozens in yeast and hundreds in humans) remain uncharacterized (Xiong & Zhu, 2016) (Xu & Ren, 2015).

So far, PQLC2 has never been purified from either a recombinant host or directly from isolated lysosomes. We decided to use the yeast *S. cerevisiae* as a host to produce recombinantly a mammalian PQLC2. *S. cerevisiae* is a well-characterized system successfully used to express eukaryotic membrane proteins (Carlesso et al., 2022) (Winkelmann et al., 2020) (Pedersen et al., 2013) (Mazhab-Jafari et al., 2016). This system present many advantages, including its low cost and high protein yield production (Nielsen, 2013). Another important factor is that our laboratory has extensive experience in the expression of membrane proteins in *S. cerevisiae*, enabling functional and structural characterization (Lamy et al., 2021) (Lenoir et al., 2002). We commonly use the *S. cerevisiae* W3031b Gal4-2 strain that possesses two copies of the Gal4-2 transcription factor to reinforce the expression level of the targeted protein (Azouaoui et al., 2014b) (see section **material and methods**). We cloned the gene encoding the rat ortholog of PQLC2 into the pYeDP60 vector and introduced a

superfolder GFP at the C-terminal end of the transporter. Moreover, we engineered a Hrv-3C protease recognition sequence between the GFP and the C-terminal end of PQLC2. One common strategy to assess the transport activity of lysosomal membrane transporters consists on mutating the lysosomal sorting motif resulting in the redirection of the protein to the cytoplasmic membrane where cell-based transport assays can be easily conducted (Kalatzis, 2001) (Jézégou et al., 2012) (Morin et al., 2004). A previous study using recombinant rat PQLC2 expressed in *Xenopus* oocytes showed that the mutation of its lysosomal sorting motif, the di-leucine motif located at the C-terminal region of PQLC2, by alanine (L290A/L292A or LL/AA) results in the reorientation of the GFP tagged PQLC2 from the lysosomal membrane to the plasma membrane (Leray et al., 2021). To verify this, we cloned the two versions of rat PQLC2 (wild type and LL/AA) into the pYeDP60 vector and expressed them in *S. cerevisiae*.

To study the localization of PQLC2 expressed in yeast, we performed a small-scale culture expressing PQLC2 (LL/AA) or wild type PQLC2, and observed the yeast cells under a fluorescence confocal microscope taking advantage of the GFP fused to PQLC2. The fluorescent images (**Figure 33. A)** revealed that PQLC2 is localized in the membrane of an intracellular organelle that resemble the yeast vacuole, the analogue of the mammalian lysosome (Matile & Wiemken, 1967) (Wiederhold et al., 2009). These results are in agreement with a previous work (Jézégou et al., 2012). Interestingly, the membrane localization of PQLC2-GFP does not change regardless the presence or absence of the di-leucine-based lysosomal sorting motif (**Figure 15. A**, upper panel compared to lower panel).

Next, after expressing PQLC2 (LL/AA) in large-scale cultures, we harvested the P2 and P3 membranes corresponding to the light and heavy membranes respectively (see section **material and methods**). Western blot analysis of P3 membrane fraction showed that PQLC2 (LL/AA)-GFP is present at around 50 kDa (**Figure 33. B**). For the following experiments of protein purification, we used P3 membranes expressing PQLC2 (LL/AA), as previous studies have shown that well-folded and functional over-

expressed proteins are more likely to be present in P3 membranes (Jacquot et al., 2012) (Lamy et al., 2021).

A.

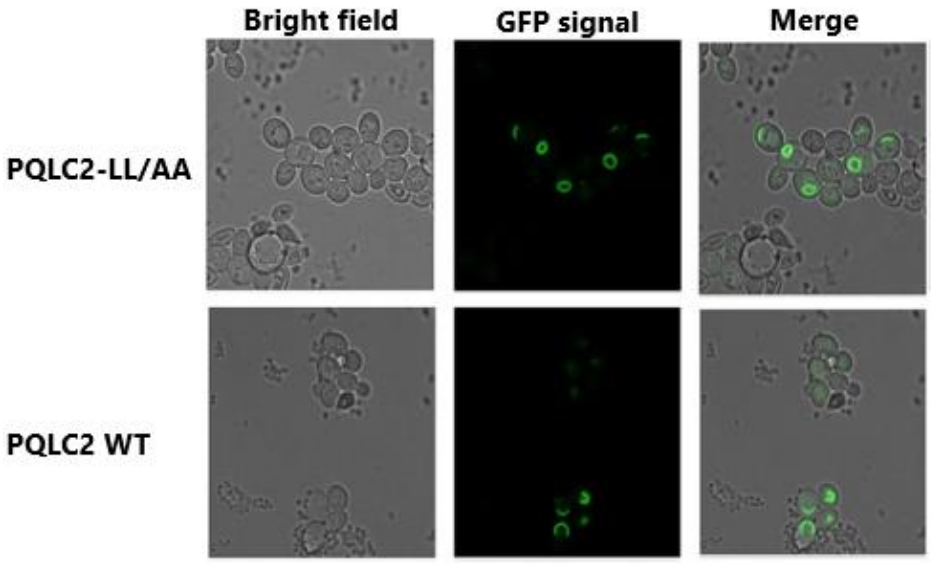

B.

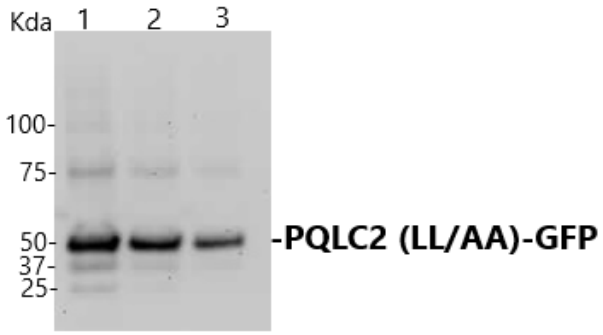

Figure 33. Expression of rat PQLC2 in *S. cerevisiae* strain W3031b Gal4-2. A. Fluorescent confocal microscopy images of *S. cerevisiae* cells expressing two versions of PQLC2-GFP. The images show that both, PQLC2 (LL/AA) and PQLC2 WT are located in enclosed vacuole-like organelles. Images on left: bright field, middle: GFP fluorescence and right: merge. **B.** Western blot analysis of PQLC2 (LL/AA) obtained from P3 membranes. Lane 1 : 5 µg (lane 1), 2 µg (lane 2), and 1 µg (lane 3) of total protein were loaded into the SDS-PAGE gels. GFP- tagged PQLC2 (LL/AA) was detected with a primary mouse anti-GFP antibody. Theoretical mass PQLC2-GFP = 58,5 kDa . PQLC2-GFP is detected at around 50 kDa.

4.2 SOLUBILIZATION SCREENING OF PQLC2 (LL/AA)-GFP IN VARIOUS DETERGENTS

The extraction from the membrane and isolation of membrane proteins in a stable and correctly folded form is a critical step for subsequent purification and functional or structural characterization (Pandey et al., 2016) (Errasti-Murugarren et al., 2021). Detergents are commonly used to solubilize membrane proteins and extract them from the membrane while keeping their native state (Seddon et al., 2004) (Anandan & Vrielink, 2016). The hydrophobic part of the membrane protein is incorporated into the detergent micelles, stabilizing them in solution (Lenoir et al., 2018).

SEC coupled with fluorescence detection (FSEC or Fluorescence Size-Exclusion Chromatography) has been used throughout the years to study the stability of GFP-tagged membrane proteins in detergent (Kawate & Gouaux, 2006) (Kunji et al., 2008). FSEC permits an accurate evaluation of the degree of monodispersity in detergent of non-purified GFP-tagged membrane proteins by simply analyzing the shape and retention time of the chromatograms using the GFP fluorescence as readout (Rodríguez-Banqueri et al., 2016) (Lamy et al., 2021). We therefore analyzed by FSEC the monodispersity in solution of PQLC2 (LL/AA)-GFP solubilized with four different detergents (DDM, DM, LMNG and n-nonyl-β-D-glucoside), each supplemented by a cholesterol derivative, cholesteryl hemisuccinate (CHS).

The main elution peak corresponding to PQLC2 (LL/AA)-GFP was found in the expected region (**Figure 34. A, B and C**) ranging between 13.9 mL and 15 mL in either, DDM/CHS, LMNG/CHS and DM/CHS. The shape of the peak is fairly symmetrical, indicating good homogeneity in these three detergents, containing a small proportion of aggregated material eluting in the empty volume of the column (void volume) at around 8 mL.

On the other hand, the FSEC profile of PQLC2 (LL/AA)-GFP with n-nonyl-β-D-glucoside/CHS is broad and asymmetrical with an increased proportion of aggregated materials in the void volume (**Figure 34. D)**, indicating that the solubilized protein in

micelles is not completely homogeneous. Given that the micelle's size and shape depend on the chemical nature of the detergent (determined by the alkyl chain length and head group) (**Figure 35**). As expected, the elution peak corresponding to PQLC2 (LL/AA) is slightly displaced upon solubilization with different detergents (Oliver et al., 2013) (**Figure 34**).

The apparent molecular weight at which PQLC2 (LL/AA)-GFP is eluted from the gel-filtration column (~400 kDa) is substantially higher than the theoretical molecular weight of PQLC2 (LL/AA)-GFP, which is around 60 kDa (**Figure 33. B**). Detergent-solubilized membrane proteins tend to elute in gel filtration at higher molecular weights, as expected, due to the presence of the detergent/lipid belt surrounding the hydrophobic fraction of the protein, which significantly increases its hydrodynamic ratio (Chaptal et al., 2017). In addition, as some members of the PQ loop family are known to assemble into homooligomers (Tao et al., 2015) , these chromatograms may also suggest that detergent-solubilized PQLC2 (LL/AA)-GFP is perhaps also a homooligomer. Overall, by comparing both the fluorescence intensity of the main elution peak and the shape of the chromatograms, we concluded that DDM is the detergent with better solubilization efficiency of PQLC2 (LL/AA)-GFP from membranes, in terms of protein yield and homogeneity.

We also tested the effect of cholesteryl hemisuccinate (CHS) on the solubilization efficiency of PQLC2 (LL/AA)-GFP with DDM. Several studies have shown that CHS can play an important role on stabilizing membrane proteins after detergent solubilization by mimicking its interactions with cholesterol in the cell membranes (Sonoda et al., 2010) (Lamy et al., 2021). Mammalian lysosomal membranes contain cholesterol (Rudnik & Damme, 2021). However, *S. cerevisiae* do not contain cholesterol but ergosterol, its structural analogue (Jordá & Puig, 2020). Nevertheless, Western blot analysis of PQLC2 (LL/AA)-GFP membranes solubilized with DDM showed that the presence of CHS does not affect the solubilization efficiency of PQLC2 (LL/AA)-GFP (results not shown).

A.

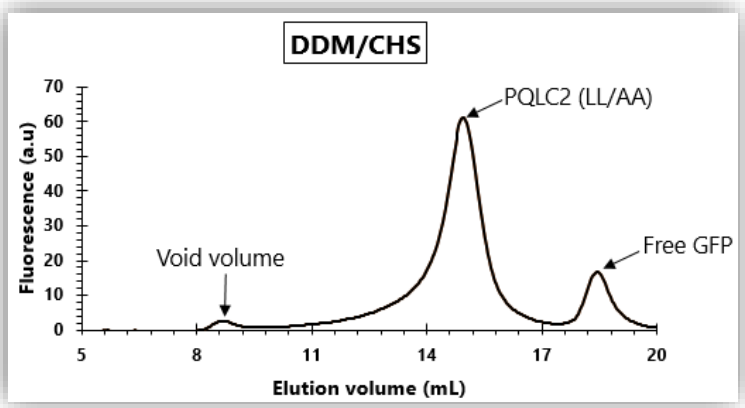
DDM/CHS
PQLC2 (LL/AA)
Void volume
Free GFP
Fluorescence (a.u)
Elution volume (mL)

B.

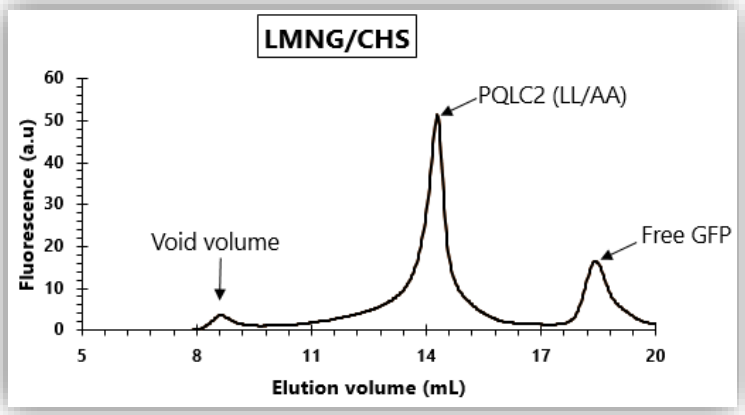
LMNG/CHS
PQLC2 (LL/AA)
Void volume
Free GFP
Fluorescence (a.u)
Elution volume (mL)

C.

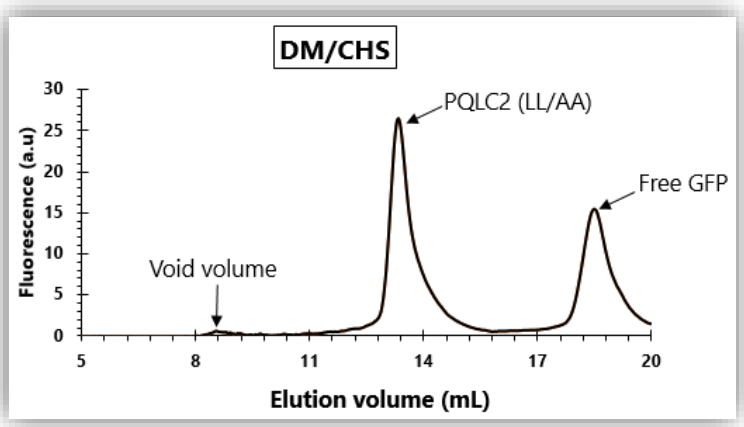
DM/CHS
PQLC2 (LL/AA)
Void volume
Free GFP
Fluorescence (a.u)
Elution volume (mL)

D.

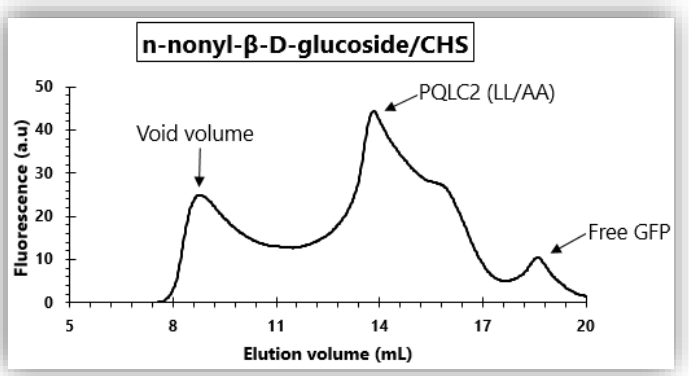

Figure 34. FSEC chromatograms of PQLC2 (LL/AA) solubilized in various detergents. PQLC2 (LL/AA) P3 membranes containing 5 mg/mL of total protein concentration were solubilized with 2% (w/v) of the following detergents : DDM (*A*), DM (*B),* LMNG (C) or n-nonyl-β-D-glucoside (D) (supplemented with 0.4 % (w/v) CHS) for 1h at 4°C. Next, the insoluble fraction was removed by ultracentrifugation and 400 µL of the detergent-solubilized supernatant was loaded onto a superose 6 increase 10/300 GL column equilibrated with FSEC buffer. GFP fluorescence was measured using excitation and emission wavelengths of 470 and 510 nm, respectively. Void volume, PQLC2 (LL/AA) and free-GFP peaks are indicated by arrows.

A.

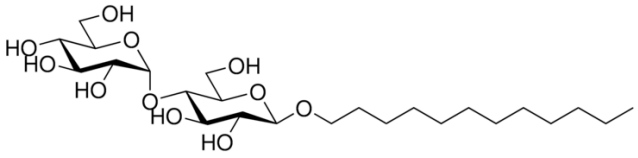

B.

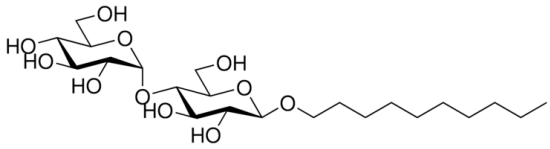

C.

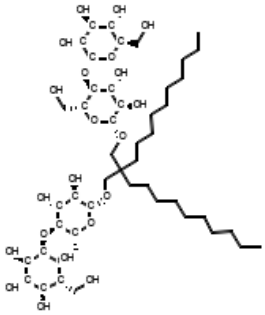

D.

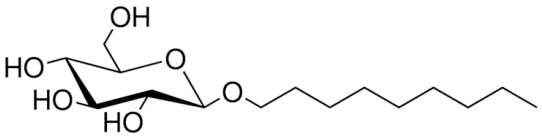

Figure 35. Chemical structures (A) DDM, (B) DM, (C) LMNG and (D) n-nonyl-β-D-glucoside.

4.3 ESTABLISHING A PURIFICATION PROTOCOL OF PQLC2

Tagging the C-terminal region of PQLC2 with the superfolder GFP enables several procedures : (i) membrane localization of PQLC2 in yeast cells by confocal microscopy (Straight et al., 1996), (**Figure 15**) (ii) evaluation of stability and monodispersity by FSEC after detergent solubilization (Kawate & Gouaux, 2006) (**Figure 16**), and, (iii) purification of PQLC2 using anti-GFP nanobodies (nanoGFP) covalently coupled to agarose beads (Lamy et al., 2021) (Rothbauer et al., 2008) (Z. Zhang et al., 2020) (Whicher & MacKinnon, 2016) (Jojoa-Cruz et al., 2018). NanoGFP, specifically recognizes the GFP with a binding affinity in the nanomolar range (Kubala et al., 2010)

(Jin et al., 2023). NanoGFP has been used in the literature to relocate GFP-tagged proteins to different cellular sites (Estes et al., 2000) (Bellaïche et al., 2001) (Beach et al., 1999). In our laboratory, we have establish a robust protocol based on the specific and strong recognition between the nanoGFP and the GFP for the purification of membrane transport proteins tagged with the GFP (Lamy et al., 2021). The nanoGFP are expressed in the bacteria *E. coli* and purified using a his-tag affinity chromatography (see section **material and methods**). The different fractions obtained during purification were analysed by SDS-PAGE (**Figure 36. A**). SEC of purified nanoGFP shows a single elution peak at around 13 kDa, indicating that it can be produced and purified as a stable monomer (**Figure 36. B)** (Rothbauer et al., 2008).

To characterize the nanoGFP, we tested the capacity of the purified nanoGFP to bind purifed superfolder GFP, as previously described (Rothbauer et al., 2008). Equimolar amounts of both proteins were mixed, incubated for about 20 min at 4°C and subjected to gel-filtration. Comparing the FSEC of this mixture and GFP alone, shows that nanoGFP and GFP assemble into a stable complex with a corresponding molecular mass of 43 kDa (**Figure 37**), in agreement with the sum of the molecular mass of both proteins.

A.

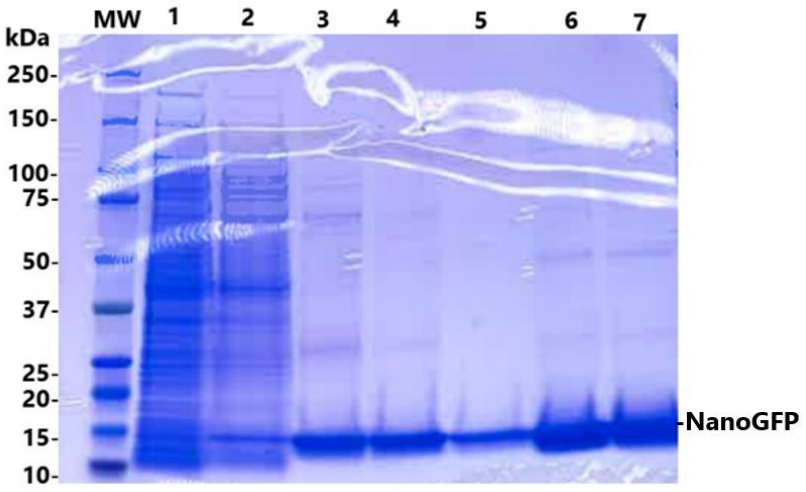

B.

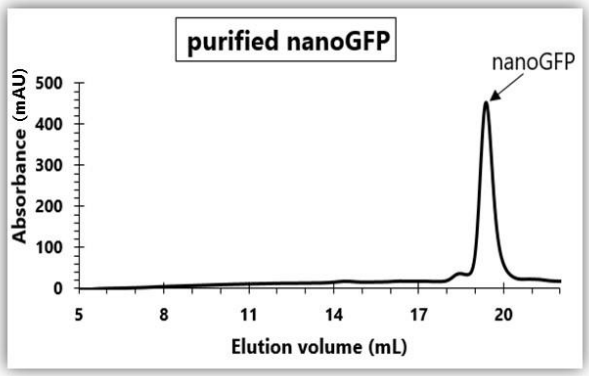

Figure 36. Purification and gel-filtration analysis of nanoGFP. (**A**) The different fractions obtained during nanoGFP purification were analysed by SDS-PAGE followed by Coomassie blue staining. 10 µL of each purification fraction was loaded onto 4-15% precast Mini-PROTEAN® gels. Proteins were stained with Coomassie blue. Lane 1 : supernatant before incubation with TALON® beads; lane 2 : flow through lane 3, 4 and 5 : the three washes of the beads. Imidazole elution at 150 mM (lane 6), and 300 mM (lane 7) . NanoGFP was detected at around 14 kDa, corresponding to the theoretical mass. (**B**) purified nanoGFP was injected into a Superose 6 increase 10/300 GL column. The arrow indicates the elution of nanoGFP. NanoGFP elution elutes from the column in peak fractions corresponding to an apparent molecular mass of ~ 15 kDa.

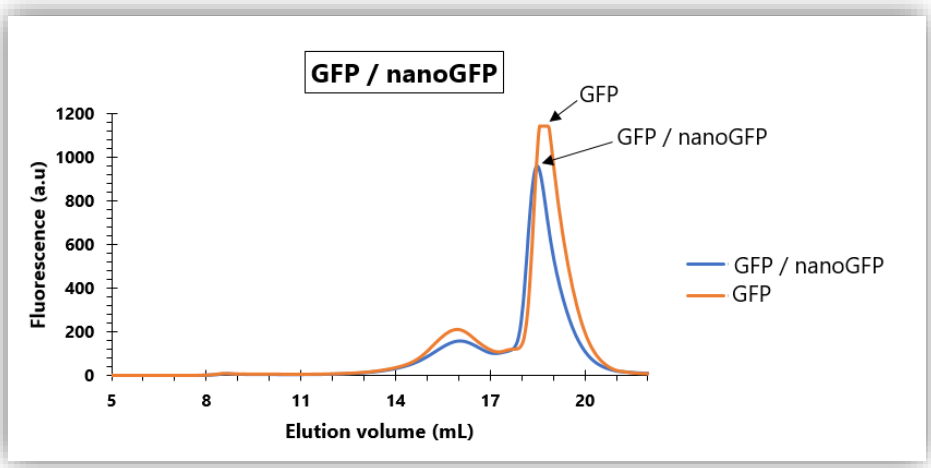

Figure 37. The binding capacity of the complex GFP/nanoGFP. Purified GFP was mixed with nanoGFP in stoichiometric amounts and subjected to FSEC in a Superose 6 increase 10/300 GL column. The chromatogram of the complex GFP/nanoGFP (blue) was superimposed with the chromatogram of purified GFP (orange). Arrows indicate the elution peaks of either, GFP alone and the complex GFP/nanoGFP.

In order to prepare the affinity column to purify PQLC2-GFP, the nanoGFP were covalently coupled to agarose beads following the protocol seen in material and methods (Rothbauer et al., 2008) to obtain what we call the home-made GFP-Trap beads.

4.4 Affinity purification of PQLC2 (LL/AA and WT) using GFP-Trap affinity chromatography

Solubilized P3 membranes containing PQLC2 (LL/AA)-GFP in 2% (w/v) DDM/CHS were incubated with the GFP-Trap beads, and after a column washing step, PQLC2 (LL/AA) was eluted by incubating the beads with hrv-3C protease O/N at 4°C, which cleaves between the C-terminal end of the transporter and the GFP, releasing only PQLC2 into the solution. The eluted purified PQLC2 (LL/AA) was loaded into SDS-PAGE and after a Coomassie blue staining a single band was detected around 25 kDa (**Figure 38. A, left panel**). The theoretical molecular weight of PQLC2 (LL/AA) is ~32 kDa, however membrane proteins often run a bit faster in SDS-PAGE gels (Rath et al., 2009). Indeed,

Western blot analysis using two anti-PQLC2 primary antibodies targeting either the cytoplasmic loop between TMs 5 and 6 and the C-terminal end confirmed that this band correspond to PQLC2 (LL/AA) (**Figure 38. A, right panel**). In addition, the analysis by mass spectrometry of this electrophoretic band after chymotrypsin digestion confirmed the identity of the protein as well as our success in expressing and purifying the rat PQLC2 (LL/AA) using *S. cerevisiae* as heterologous host (**Figure 38. B**). In P2 and P3 membranes, PQLC2 (LL/AA)-GFP represents around 2% of all membrane and membrane-associated proteins. After recovery of the yeast membranes, the yield of our affinity purification is estimated to be 1.5 mg of purified PQLC2 (LL/AA) per liter of culture.

A.

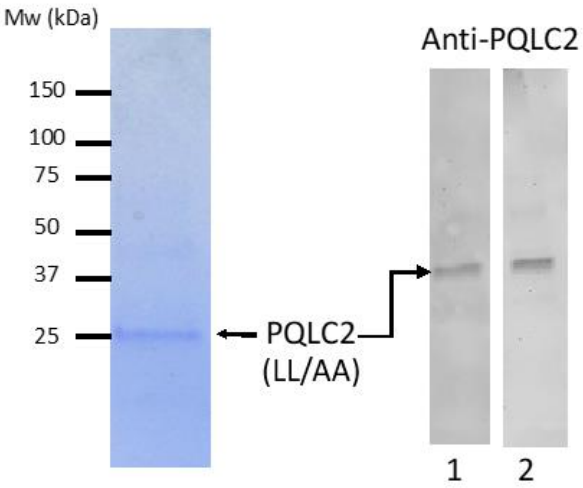

B.

```
  1 MVWRTLVASN FSTCPNGSIQ WIWDVFGECA QDGWDEASVA LGLVSIFCFA
 51 ASTFPQYIKA CKTGNMDQAL SLWFLLGWIG GDSCNLIGSF LADQLPLQTY
101 TAVYYVLADL LMLTLYFHYK FKKQPSLLSA PINSVLLFIL GTVCITPLLS
151 STDPVAVPRE GFRGRTLLSV EPGNKPFTKK EVVGFVIGSA SSVLYLLSRL
201 PQIRTNFVRQ STQGISYSLF ALVMLGNTLY GLSVLLKNPE VGQSEGSYLL
251 HHLPWLVGSL GVLLLDTIIS IQFLVYRSHD ADAASEREPL LPS
```

Figure 38. Characterization and identification of purified PQLC2 (LL/AA) in SDS-PAGE. (**A**) The eluted fraction was concentrated and then loaded into SDS-PAGE gel, followed by Coomassie blue staining (left). Western blot analysis of 1 µg of purified PQLC2 (LL/AA) using rabbit anti-PQLC2 antibodies targeting either, the cytoplasmic loop between TMs 5 and 6 (1), or the C-terminal end (2) of PQLC2. PQLC2 was detected at around 25 kDa. (**B**) Mass spectrometry data obtained from the PQLC2 electrophoretic band digested with chymotrypsin. The PQLC2 peptides identified by mass spectrometry are displayed in red, and correspond to 68% of the entire protein sequence.

Although our PQLC2 (LL/AA) purification protocol yielded a relatively pure protein in reasonable quantities, we encountered problems with protein stability in DDM when the eluted fractions from the affinity chromatography were subjected to concentration prior characterization by size-exclusion chromatography. **Figure 39** shows one of the

most severe examples of the SEC profile of purified PQLC2 (LL/AA) after concentration up to 2-3 mg/ml before injection. The SEC profile shows multiple and asymmetric peaks, where Coomassie-stanning SDS-PAGE of different fractions along the chromatogram indicates the presence of PQLC2 (LL/AA) at around 15 mL.

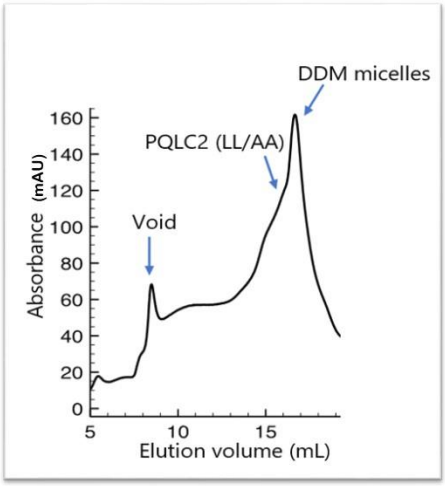

Figure 39. SEC chromatogram of purified PQLC2 (LL/AA). After affinity purification in DDM/CHS, the elution fraction was concentrated, ultracentrifuged, and injected into a Superose 6 increase 10/300 GL column equilibrated with SEC buffer (arrows indicate the void volume, DDM micelles and PQLC2 (LL/AA)).

To assess whether the di-leucine mutations at the C-terminal end of PQLC2 (LL/AA) caused the protein's instability, we purified PQLC2 (WT) using the same protocol. The FSEC chromatogram of PQLC2 (WT) solubilized in DDM/CHS shows that PQLC2 (WT)-GFP elutes as a slightly asymmetric peak displaced by 1 mL compared with PQLC2 (LL/AA)-GFP (**Figure 34. A and Figure 40. A**). Interestingly, the eluted purified PQLC2 (WT) was loaded into SDS-PAGE gel and after a Coomassie blue staining a single band was detected at around 50 kDa despite the protein sample buffer contains a reducing agent (**Figure 40. B**). As for PQLC2 (LL/AA), our PQLC2 (WT) purification protocol also yielded a reasonable quantity of relatively pure protein. However, in our hands, PQLC2 (WT) was even less stable than PQLC2 (LL/AA) after affinity purification since the protein

started to precipitate during concentration and, therefore, we were unable to perform SEC of this sample.

A.

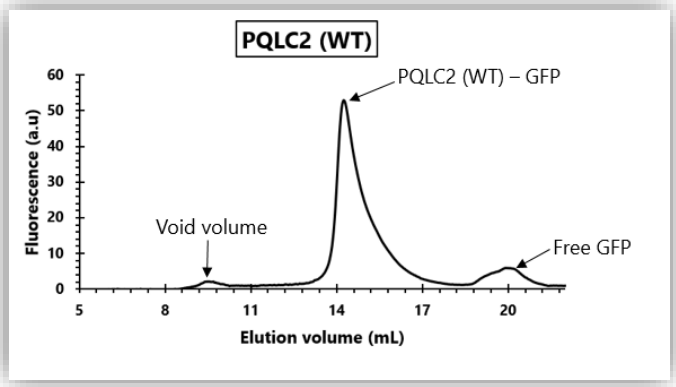

B.

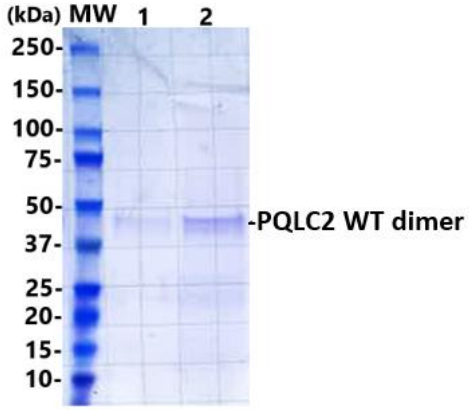

Figure 40. FSEC chromatogram of PQLC2 (WT)-GFP and SDS-PAGE of purified PQLC2 WT. (**A**) FSEC chromatograms of PQLC2 (WT)-GFP solubilized in DDM/CHS. PQLC2 (WT)-GFP P3 membranes containing 5 mg/mL of total protein concentration were solubilized with 2% (w/v) of DDM (supplemented with 0.4 % (w/v) CHS) for 1h at 4°C. Next, the insoluble fraction was removed by ultracentrifugation and 400 µL of the detergent-solubilized supernatant was loaded onto a Superose 6 increase 10/300 GL column equilibrated with FSEC buffer. GFP fluorescence was measured using excitation and emission wavelengths of 470 and 510 nm, respectively. Void volume, PQLC2 (WT) and free-GFP peaks are indicated by arrows. (**B**) The eluted fraction from affinity purification of PQLC2 (WT) was concentrated and then loaded into SDS-PAGE gel, followed by Coomassie blue staining. PQLC2 WT (dimer) was detected at around 50 kDa.

4.5 ENGINEERING STABILITY IN PURIFIED PQLC2 (LL/AA)

4.5.1 N-terminal deletions of PQLC2 (LL/AA)

To increase protein stability after purification, we decided to use protein-engineering tools. Protein engineering is a powerful approach for improving the stability of membrane transporters (Rodríguez-Banqueri et al., 2016) (Rawlings, 2018). After analyzing the Alphafold V2.0 model of PQLC2 (**Figure 41. A**), we noted that the N-terminal region of PQLC2 is a highly charged region predicted to be disordered. Following a similar strategy used by Gonen and collaborators to obtain the crystal structure of the lysosomal amino acid transporter SLC38A9 we removed the first 11 or 29 amino acids from the N-terminal region of PQLC2 (LL/AA), leading to Δ11 or Δ29 PQLC2 (LL/AA), (**Figure 41. A**) (Lei et al., 2018). As previously done with the previous versions of PQLC2, we assessed the monodispersity of detergent-solubilized Δ11 or Δ29 PQLC2 (LL/AA) by FSEC. Δ11 PQLC2 (LL/AA)-GFP shows a fairly symmetrical peak around 14.5 mL (**Figure 41. B, left panel**). On the other hand, Δ29 PQLC2 (LL/AA)-GFP has a large void volume and an asymmetrical peak that elutes around 12 mL, clearly indicating the poor stability of this mutant in detergent micelles (**Figure 41. B, right panel**). Based on these results, we proceeded to the purification of Δ11 PQLC2 (LL/AA). Based on these FSEC experiments, it seems that the N-terminal region of PQLC2, at least from residues 11 to 29 plays some role in maintaining the stability of PQLC2 (LL/AA) in detergent micelles.

A.

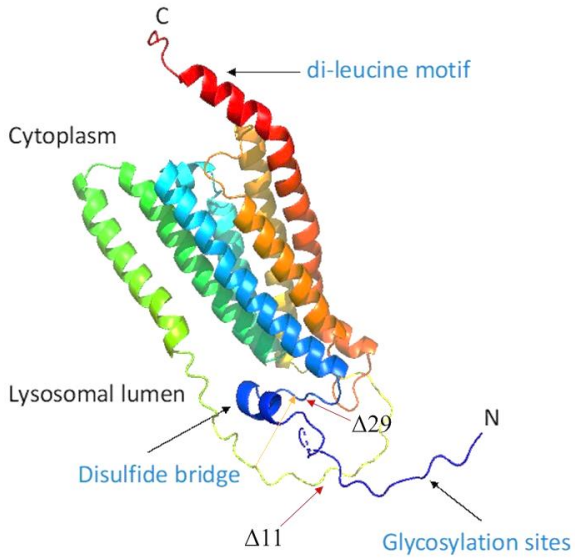

B.

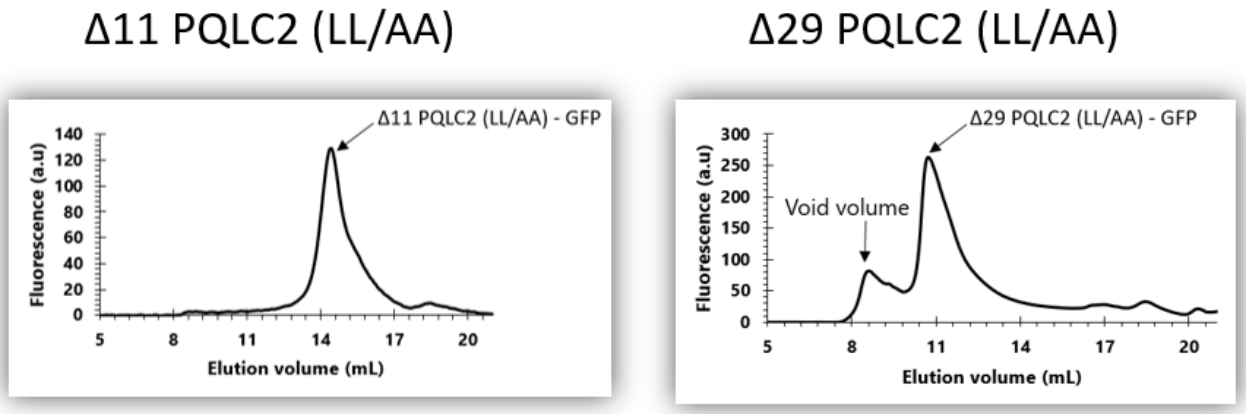

Figure 41. FSEC for Δ11 PQLC2 (LL/AA) and Δ29 PQLC2 (LL/AA). (**A**) PQLC2 (LL/AA) AlphaFold V2.0 model with arrows showing the positions deleted to make the Δ11 or the Δ29 PQLC2 (LL/AA) mutants. In addition, positions for a predicted disulfide bridge and a glycosylation site are also indicated by arrows, as well as the di-leucine motif at the C-terminal end. Membrane is depicted as a grey rectangle. (**B**) P3 membranes of Δ11 PQLC2 (LL/AA) (left panel) or Δ29 PQLC2 (LL/AA) (right panel) containing 5 mg/mL of total protein were solubilized with 2% (w/v) DDM/CHS, ultracentrifuged and injected into a Superose 6 increase 10/300 GL column equilibrated with FSEC buffer. GFP fluorescence was measured using excitation and emission wavelengths of 470 and 510 nm, respectively. Void volume, and Δ11 or Δ29 PQLC2 (LL/AA) elution peaks are indicated by arrows.

4.5.1.1 Purification of Δ11 PQLC2 (LL/AA)

We purified Δ11 PQLC2 (LL/AA) using the same strategy as for PQLC2 (LL/AA). Similarly as the previous purifications, Δ11 PQLC2 (LL/AA) was detected in SDS-PAGE at around 25 kDa and 50 kDa by Coomassie blue staining, corresponding to the apparent Mw of the monomer and the dimer, respectively (**Figure 42. A**). The eluted fraction of Δ11 PQLC2 (LL/AA) was concentrated up to 30 µM and analyzed by SEC. Δ11 PQLC2 (LL/AA) SEC's profile was highly polydispersed, very similar as the one obtained previously with PQLC2 (LL/AA) (**Figure 42. B upper panel**). The eluted fraction was collected and a Coomassie blue staining was performed, confirming the presence of Δ11 PQLC2 (LL/AA) between 14.5 and 16.5 mL (**Figure 42. B lower panel**). The second peak in the chromatogram at around 16.5 mL corresponds to empty DDM micelles. In conclusion, we have successfully purified Δ11 PQLC2 (LL/AA), but the SEC results indicate that this mutant is also unstable in DDM micelles; hence the sample is not suitable for further functional and structural characterization. We therefore adopted another approach to improve the protein's stability.

A.

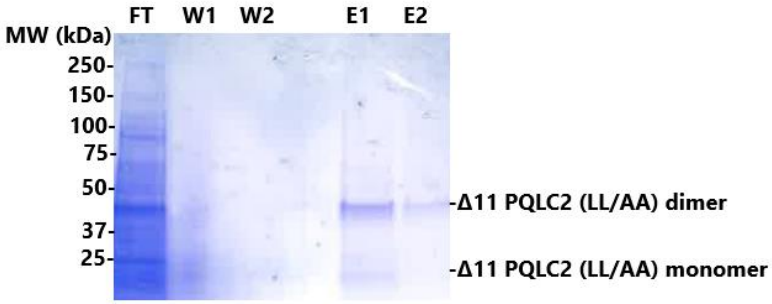

B.

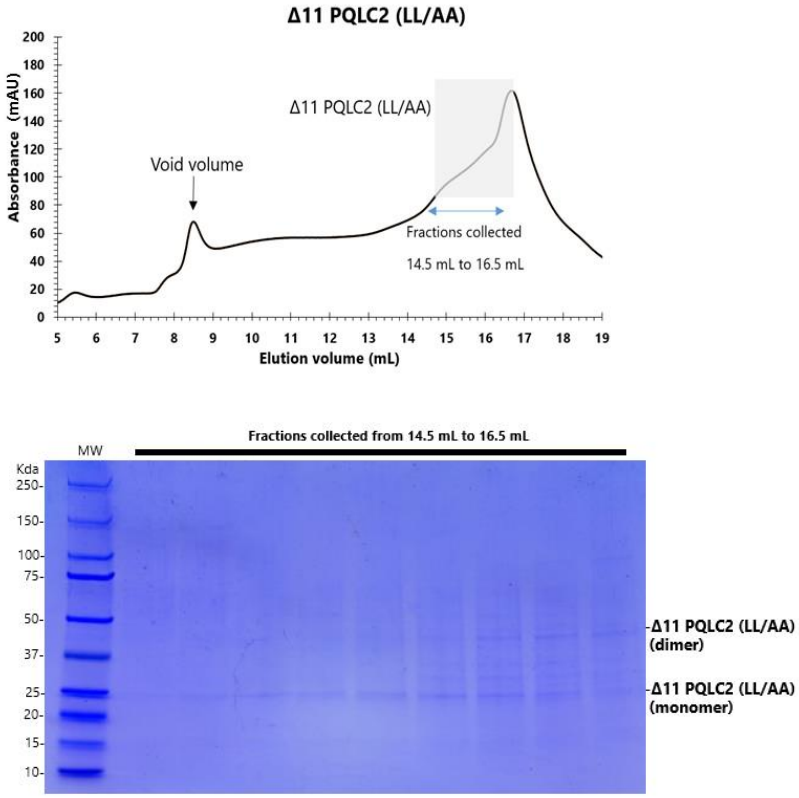

Figure 42. Purification Δ11 PQLC2 (LL/AA). (**A**) After Δ11 PQLC2 (LL/AA) purification, the different fractions were loaded into SDS-PAGE gel, followed by Coomassie Blue staining. FT : flowthrough (diluted 10x), W1 : wash 1, W2 : wash 2, E1 : elution 1, E2 : elution 2. Δ11 PQLC2 (LL/AA) was detected at around 25 and 50 kDa. (**B**) Upper panel: after purification, the elution fraction was concentrated, ultracentrifuged then injected into injected into a Superose 6 increase 10/300 GL column equilibrated with SEC buffer (containing 0.02% (w/v) DDM). The arrow indicates the void volume, and the gray rectangle the SEC fractions collected for SDS-PAGE analysis. (**B**) Lower panel: Collected SEC fractions (between 14.5 mL and 16.5 mL) were loaded into SDS-PAGE followed by Coomassie blue staining. Δ11 PQLC2 (LLAA) monomers and dimers are indicated.

4.5.2 Consensus-based mutagenesis of mammalian PQLC2 (LL/AA)

We decided to use a consensus-based mutagenesis approach to build stability of PQLC2 (LL/AA) in detergent micelles. This approach introduces the most prevalent amino acid residues at a given position based on a sequence alignment of PQLC2 homologs. Previous works have demonstrated the suitability of this approach to improve the thermostability (a way to measure the stability of the membrane protein in detergent micelles) of soluble and membrane transport proteins (Oda et al., 2020) (Canul-Tec et al., 2017). A consensus amino acid sequence was calculated from 22 aligned sequences of closed PQLC2 (LL/AA) homologs using JALVIEW (version 2.11.3.3) (**Figure 43**) (Cirri et al., 2018) (Waterhouse et al., 2009). The final sequence of PQLC2 (LL/AA) consensus was designed using the consensus sequence and the criteria used by Erica Cirri et al., 2018. An amino acid at a given position was replaced by the consensus one when the frequency of occurrence of the later is more than 20 %, and higher than 10 % than the corresponding amino acid in rat PQLC2 (LL/AA). We decided in this first sequence design to not replace residues in both the N- or the C-terminal end of PQLC2 as these regions are often the most variable ones in membrane proteins and sometimes, they are also be implicated on trafficking the protein to the final membrane destination. This consensus-based mutagenesis approach resulted in the PQLC2 (LL/AA) consensus with 19 mutations (**Figure 44**). These mutations are mainly located in predicted hydrophobic regions of PQLC2, and 10 of those 19 mutations involve conservative substitutions between residues (e.g. from valine to leucine).

ClustalW pairwise sequence alignment showed that PQLC2 (LL/AA) consensus shares amino acid 93 % identity with PQLC2 (LL/AA) (**Figure 45**).

Consensus-based mutagenesis approach has recently been successfully applied to other membrane transport proteins (Cirri et al., 2018) (Oda et al., 2020) (Canul-Tec et al., 2017). The AlphaFold V2.0 and docking models were used to ensure that we retained the predicted arginine (substrate)-binding sites (**Figure 46**) as well as the predicted aromatic amino acids that bind to the WDR41 protein (Talaia et al., 2021).

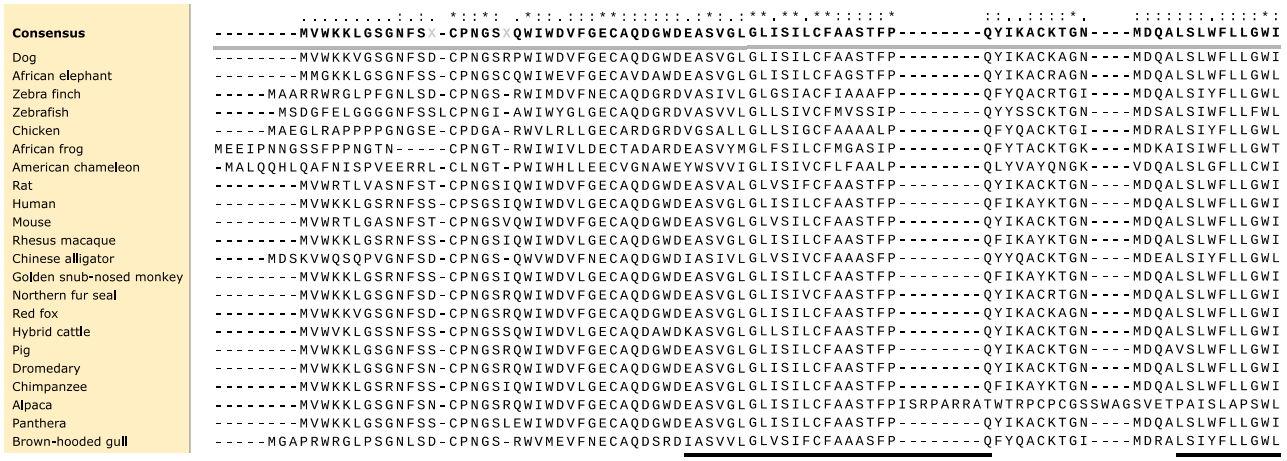
Consensus
Dog
African elephant
Zebra finch
Zebrafish
Chicken
African frog
American chameleon
Rat
Human
Mouse
Rhesus macaque
Chinese alligator
Golden snub-nosed monkey
Northern fur seal
Red fox
Hybrid cattle
Pig
Dromedary
Chimpanzee
Alpaca
Panthera
Brown-hooded gull
TM1
TM2

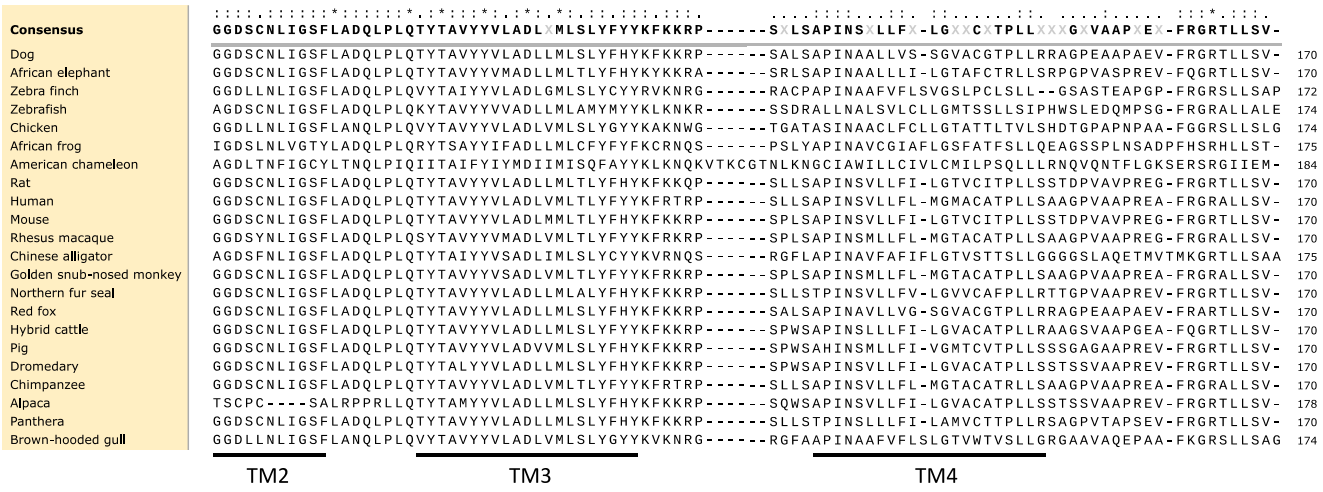
Consensus
Dog
African elephant
Zebra finch
Zebrafish
Chicken
African frog
American chameleon
Rat
Human
Mouse
Rhesus macaque
Chinese alligator
Golden snub-nosed monkey
Northern fur seal
Red fox
Hybrid cattle
Pig
Dromedary
Chimpanzee
Alpaca
Panthera
Brown-hooded gull
TM2
TM3
TM4

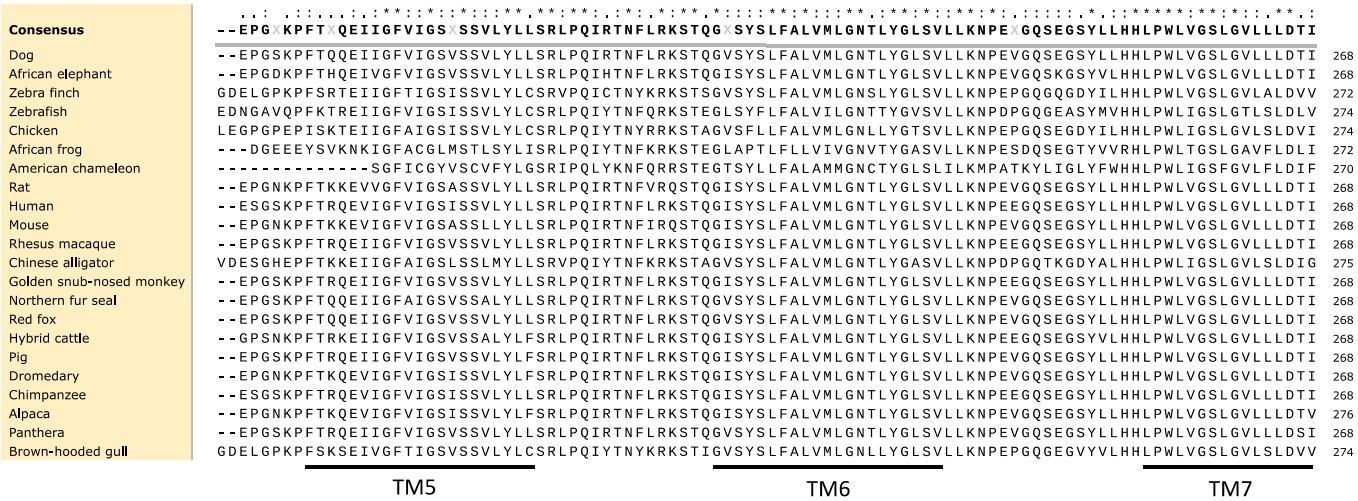
Consensus
Dog
African elephant
Zebra finch
Zebrafish
Chicken
African frog
American chameleon
Rat
Human
Mouse
Rhesus macaque
Chinese alligator
Golden snub-nosed monkey
Northern fur seal
Red fox
Hybrid cattle
Pig
Dromedary
Chimpanzee
Alpaca
Panthera
Brown-hooded gull
TM5
TM6
TM7

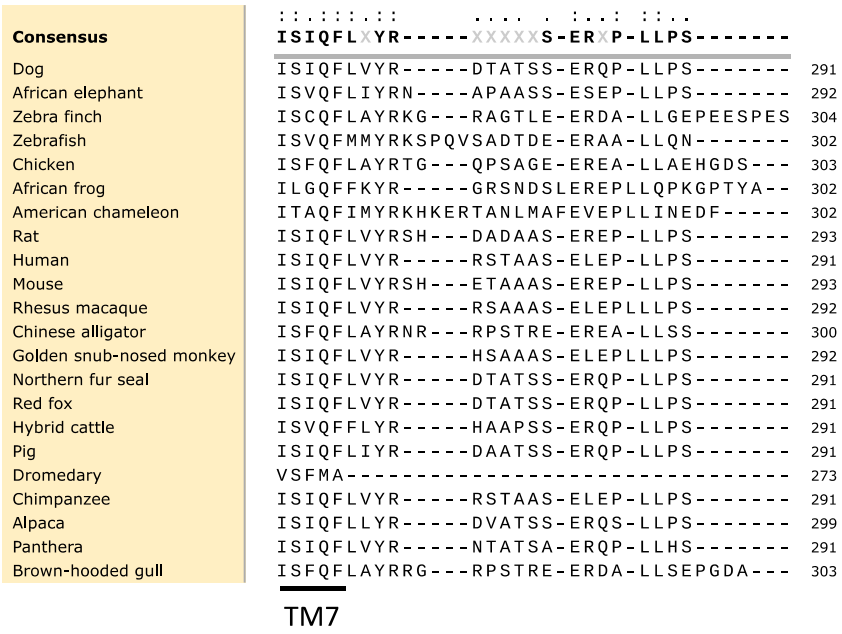

Figure 43. Multiple sequence alignement of PQLC2 (LL/AA) orthologs. The consensus sequence is indicated in bold at the top. The lines define the predicted transmembrane segments (TM) of rat PQLC2 (LL/AA) calculated using TOPCONS (https://topcons.cbr.su.se/).

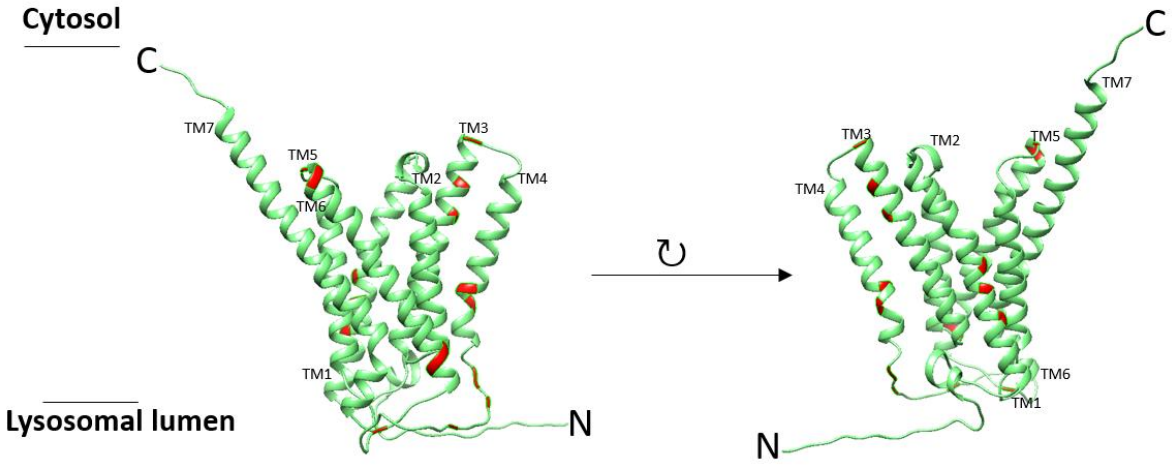

Figure 44. Residues exchanged in PQLC2 (LL/AA) to build the PQLC2 (LL/AA) consensus. Replaced amino acids are indicated in red colors in the AlpaFold V2.0 model of PQLC2 (LL/AA). Two views are shown (left and right panels) for clarity of display.

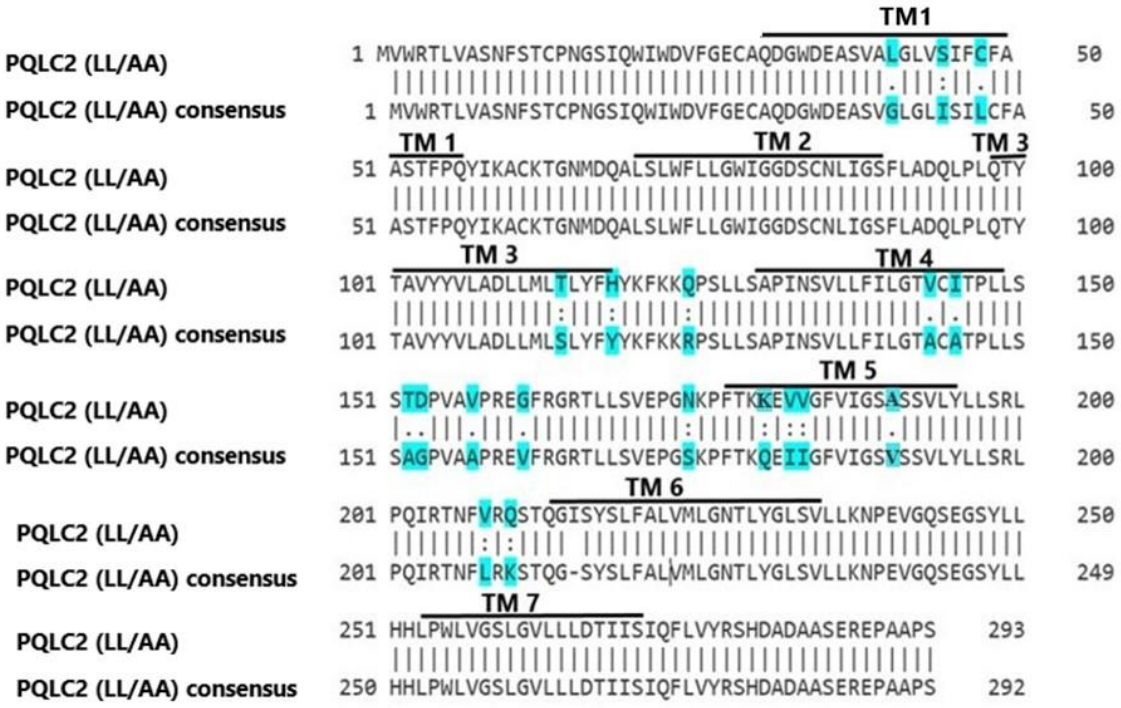

Figure 45. Pairwise sequence alignment of PQLC2 (LL/AA) and PQLC2 (LL/AA) consensus. The alignment was carried out by ClustalW. The percentage identity matrix of the pairwise sequence alignment is 93%. TMs were defined using the TOPCONS web server for combined membrane protein topology and signal peptide prediction (Tsirigos et al., 2015) (Bernsel et al., 2009).

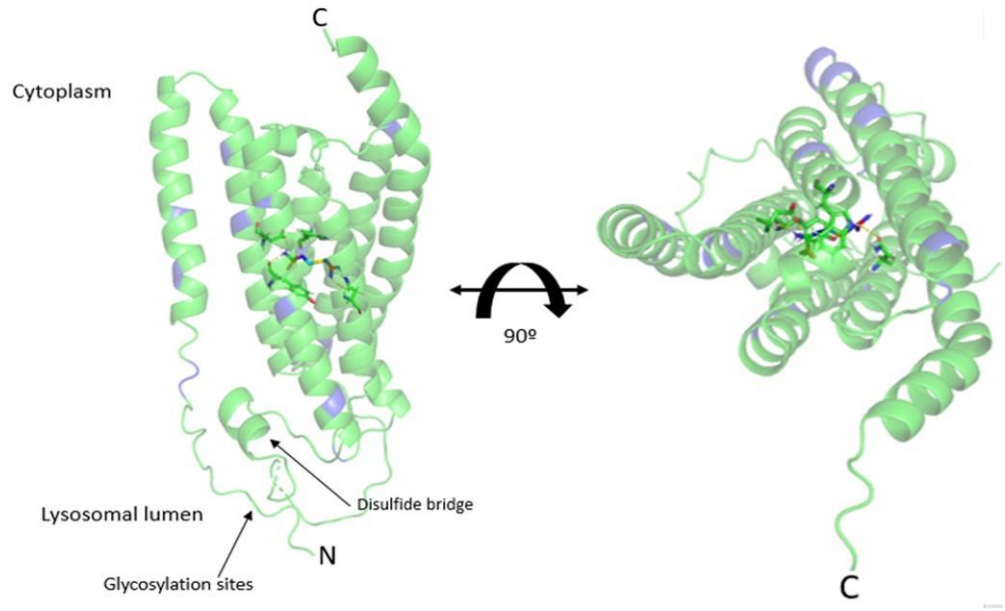

Figure 46. Docking of L-Arg into the AlphaFold V2.0 model of PQLC2. Docking was performed with AutoDock Vina using the CB-Dock web interface (http://clab.labshare.cn/cb-dock/). The figure shows the best docking pose according the AutoDock Vina docking score. Residues mutated in the PQLC2 (LL/AA) consensus version are colored in purple in the carton representation. Residues predicted to interact with L-Arg are represented by ball and stick (W78, Y105, D109 and N227).

Most importantly, PQLC2 (LL/AA) consensus was recently expressed in *Xenopus* oocytes by our collaborators Dr Bruno Gasnier and Dr Cécile Jouffret (U. Paris-Cité, Paris) and transport activity was measured by electrophysiological recording and by radioactive L-Arg accumulation. Notably the PQLC2 (LL/AA) consensus has a similar transport activity than PQLC2 (LL/AA).

4.5.2.1 Characterization of PQLC2 (LL/AA) consensus

4.5.2.1.1 Solubilization screening of PQLC2 (LL/AA) consensus-GFP in various detergents

As previously described, we analyzed by FSEC the monodispersity in solution of PQLC2 (LL/AA) consensus-GFP solubilized with three different detergents (DDM, DM and LMNG), each supplemented by a cholesterol derivative, cholesteryl hemisuccinate (CHS). The main elution peak corresponding to PQLC2 (LL/AA) consensus-GFP was

found in the expected region (**Figure 47. A, B and C**) ranging between 13.8 mL and 14.5 mL in all three detergent/CHS mixtures: DDM/CHS, LMNG/CHS, and DM/CHS. In all cases, the shape of the peak is fairly symmetrical, indicating good homogeneity. With the exception of DM/CHS, there is a small proportion of aggregated material eluting in the void volume at around 8 mL. As expected, the elution peak corresponding to PQLC (LL/AA) consensus-GFP is slightly displaced upon solubilization with different detergents (Oliver et al., 2013).

Interestingly, the LMNG/CHS chromatogram (**Figure 47. B**) shows a second peak at around 15 mL, which could indicate the co-existence of different oligomerization states of PQLC2 (LL/AA) consensus-GFP after solubilization with this detergent. As with PQLC2 (LL/AA), these chromatograms may also suggest that detergent-solubilized PQLC2 (LL/AA) consensus may also be a homooligomer.

By comparing both the fluorescence intensity of the main elution peak and the shape of the chromatograms, we concluded that DDM is the detergent with the best solubilization efficiency for PQLC2 (LL/AA) consensus-GFP membranes in terms of protein yield and homogeneity.

A.

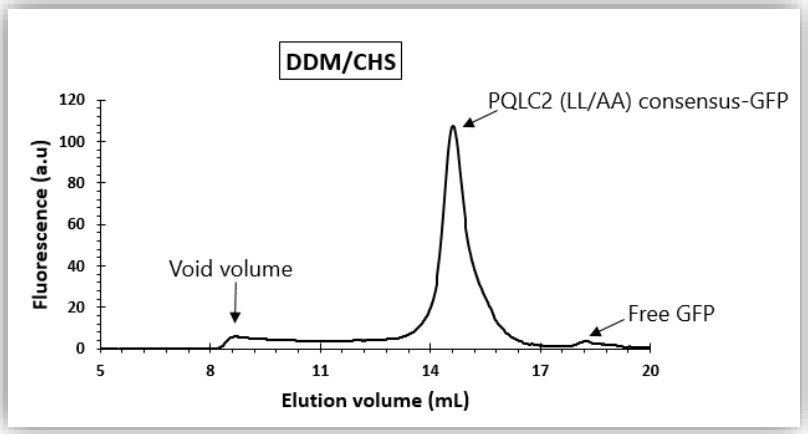
DDM/CHS
PQLC2 (LL/AA) consensus-GFP
Void volume
Free GFP
Fluorescence (a.u)
Elution volume (mL)
120
100
80
60
40
20
0
5
8
11
14
17
20

B.

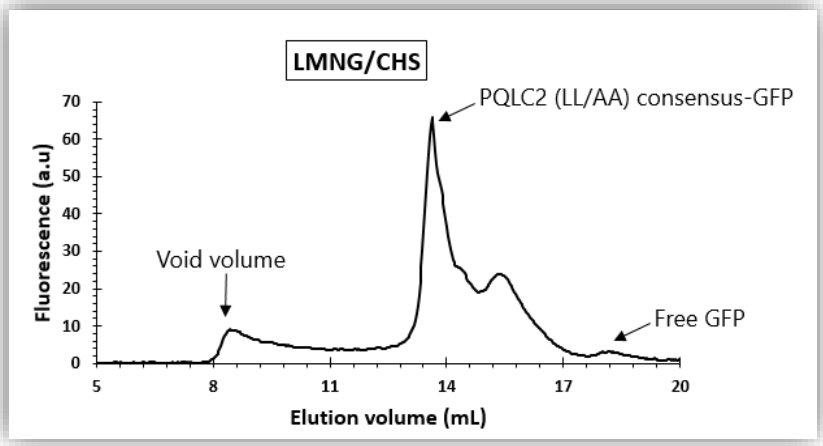
LMNG/CHS
PQLC2 (LL/AA) consensus-GFP
Void volume
Free GFP
Fluorescence (a.u)
Elution volume (mL)
70
60
50
40
30
20
10
0
5
8
11
14
17
20

C.

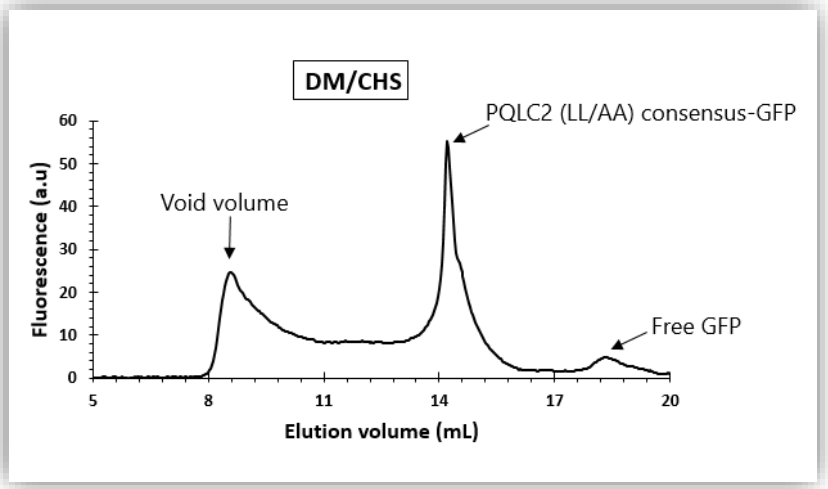

Figure 47. FSEC chromatograms of PQLC2 (LL/AA) consensus solubilized in various detergents. PQLC2 (LL/AA) consensus P3 membranes containing 5 mg/mL of total protein concentration were solubilized with 2% (w/v) of the following detergents DDM (**A**) or LMNG (**B**) or DM (**C**) (supplemented with 0.4 % (w/v) CHS) for 1h at 4°C. Next, the insoluble fraction was removed by ultracentrifugation and 400 µL of the detergent-solubilized supernatant was loaded into a Superose 6 increase 10/300 GL column equilibrated FSEC buffer. GFP fluorescence was measured using excitation and emission wavelengths of 470 and 510 nm, respectively. Void volume, free GFP and PQLC2 (LL/AA) consensus are indicated by arrows.

4.5.2.1.2 Thermostability of PQLC2 (LL/AA)-GFP and PQLC2 (LL/AA) consensus-GFP

To gain further insights into the stability of PQLC2 (LL/AA) and PQLC2 (LL/AA) consensus, we studied their thermal denaturation. Thermal denaturation is in general an irreversible process in detergent-solubilized membrane proteins (Cirri et al., 2018).

We solubilized PQLC2 (LL/AA) and PQLC2 (LL/AA) consensus P3 membranes at 4°C for 1 h. Then, we incubated the samples at increasing temperatures (45°C and 70°C). Then, we analyzed by FSEC the irreversible effect of temperature on protein solubility, aggregation, and oligomeric state. The higher protein's stability the more resistant to thermal denaturation.

At 4°C, PQLC2 (LL/AA)-GFP and PQLC2 (LL/AA) consensus-GFP eluted as a monodispersed peak at around 14.5 mL corresponding to the oligomeric state of the protein with the surrounding micelles (**Figure 48. A, B**). At a higher temperature of 45°C, the PQLC2 (LL/AA)-GFP peak slighly shifted to the left suggesting protein aggregation. Interestingly, almost no shift was observed in the PQLC2 (LL/AA)-consensus GFP at 45°C. At 70°C, the main elution peack of the two PQLC2 versions shifted to the right suggesting that the PQLC2 (LL/AA)-GFP oligomer dissociates towards a lower oligomerization (or even monomeric) state (**Figure 48. C**). In addition, the solubility decreased as shown by the higher proportion of aggregated proteins in the void volume and the area under the chromatograms at 45°C and 70°C compared with 4°C. In summary, the analysis of the thermal denaturation of the GFP-tagged version of PQLC2 by FSEC showed moderate changes, most particularly the protein aggregation at 45°C.

A.

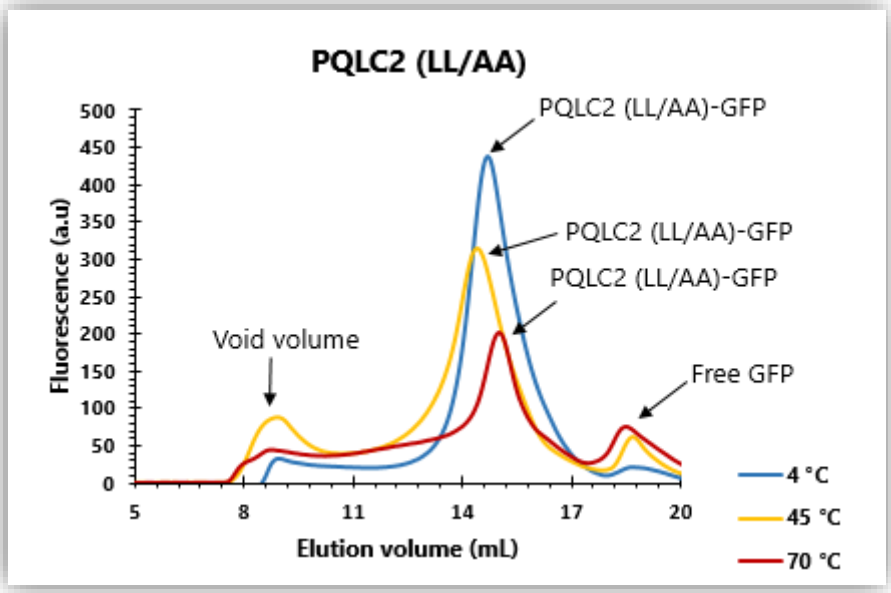
PQLC2 (LL/AA)
PQLC2 (LL/AA)-GFP
PQLC2 (LL/AA)-GFP
PQLC2 (LL/AA)-GFP
Void volume
Free GFP
Fluorescence (a.u)
Elution volume (mL)
4 °C
45 °C
70 °C

B.

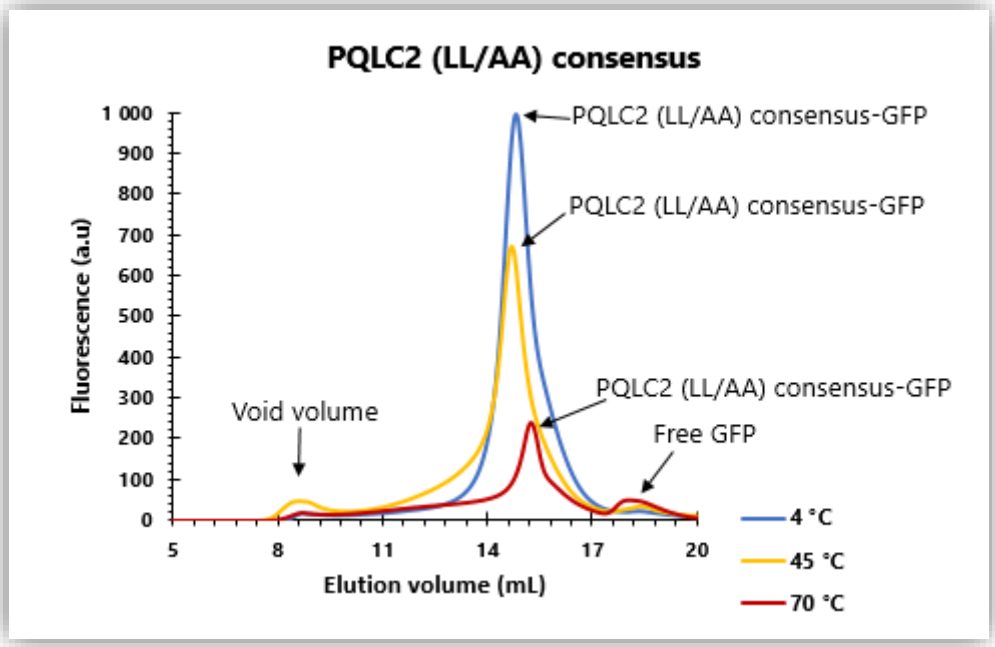
PQLC2 (LL/AA) consensus
PQLC2 (LL/AA) consensus-GFP
PQLC2 (LL/AA) consensus-GFP
PQLC2 (LL/AA) consensus-GFP
Void volume
Free GFP
Fluorescence (a.u)
Elution volume (mL)
4 °C
45 °C
70 °C

C.

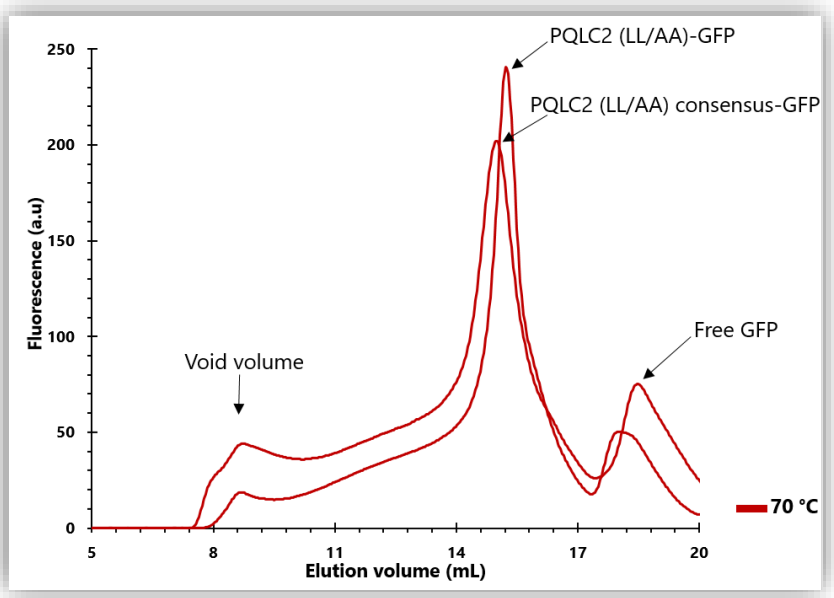

Figure 48. **Increased thermal stability of PQLC2 (LL/AA) consensus-GFP compared to PQLC2 (LL/AA).** (**A**) PQLC2 (LL/AA) or (**B**) PQLC2 (LL/AA) consensus P3 membranes containing 5 mg/mL of total protein concentration were solubilized with 2% (w/v) DDM/CHS for 1 h at 4°C. After solubilization, the samples were incubated at 4, 45 and 70°C for 1 h. Next, the insoluble fraction was removed by ultracentrifugation and 400 µL of the detergent-solubilized supernatant was loaded into a Superose 6 increase 10/300 GL column equilibrated with FSEC buffer. GFP fluorescence was measured using excitation and emission wavelengths of 470 and 510 nm, respectively. Void voulume, free GFP and PQLC2 (LL/AA) or PQLC2 (LL/AA) consensus are indicated by arrows. (**C**) Overlapped chromatograms (Figures A and B) from solubilization at 70°C for PQLC2 (LL/AA) and PQLC2 (LL/AA) consensus.

4.5.2.1.3 Thermostability of purified PQLC2 (LL/AA) and PQLC2 (LL/AA) consensus

We employed a recently developed high-throughput fluorescence-based thermal shift assay to investigate the stability of purified PQLC2 (LL/AA) and PQLC2 (LL/AA) consensus, both without the GFP tag. This was done to eliminate any potential influence of the GFP tag fused to PQLC2 on the protein's thermal stability, as the previous experiment was conducted with the GFP-tagged protein (**Figure 48**) (Sampson et al., 2021) (Crichton et al., 2015) (Majd et al., 2018). In this assay, the protein

is mixed with a fluorescent dye (CPM) and subjected to a gradual temperature increase. As the temperature rises, the protein begins to denature, causing the exposure of previously buried cysteine residues (Sampson et al., 2021). These cysteines then react with the CPM dye, leading to a measurable increase in fluorescence intensity. The temperature is ramped from 20°C to 70°C (**Figure 49**), and this process generates a characteristic melting transition, or "melt curve," which reflects the protein's thermal stability.

The melting temperature (*Tm*) is defined as the temperature at which the rate of protein unfolding is at its highest, providing a quantitative measure of the protein's stability under the experimental conditions (Sampson et al., 2021). The *Tm* of purified PQLC2 (LL/AA) consensus was approximately 70°C, higher than the *Tm* of purified PQLC2 (LL/AA) at around 61°C (**Figure 49**). This difference suggests that the consensus sequence enhances the thermal stability of PQLC2.

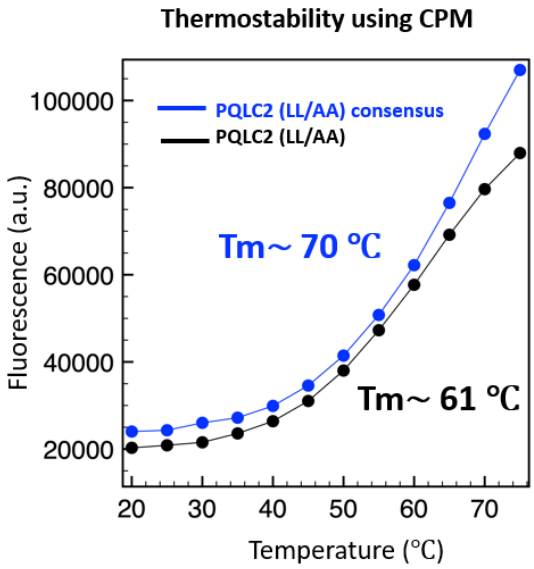

Figure 49. Increased thermal stability of purified PQLC2 (LL/AA) consensus compared to purified PQLC2 (LL/AA). The experiment was conducted in replicates. The blue line represents the melting curve of purified PQLC2 (LL/AA) consensus, while the black line represents the melting curve of purified PQLC2 (LL/AA). The Tm values for PQLC2 (LL/AA) consensus and PQLC2 (LL/AA) were calculated from the first derivative of the curve and corresponded to 70°C and 61°C, respectively. The excitation and emission wavelengths for CPM are 387 nm and 463 nm, respectively.

4.5.2.1.4 Mammalian PQLC2 (LL/AA) consensus, expressed in *S. cerevisiae*, is localized in enclosed vacuole-like organelles

As with PQLC2 (LL/AA), to study the localization of PQLC2 (LL/AA) consensus-GFP expressed in *S. cerevisiae*, we performed a small-scale culture expressing PQLC2 (LL/AA) consensus-GFP and observed the yeast cells under a fluorescence confocal microscope taking advantage of the GFP fused to PQLC2.

The fluorescent images (**Figure 50, upper panel)** revealed that PQLC2 (LL/AA) consensus-GFP is localized in the membrane of an intracellular organelle that resemble the yeast vacuole (Matile & Wiemken, 1967). These results are in agreement with those obtained for PQLC2 (LL/AA)-GFP (**Figure 33**, **lower panel**). This means that the

consensus design has not altered the membrane location of the transporter.

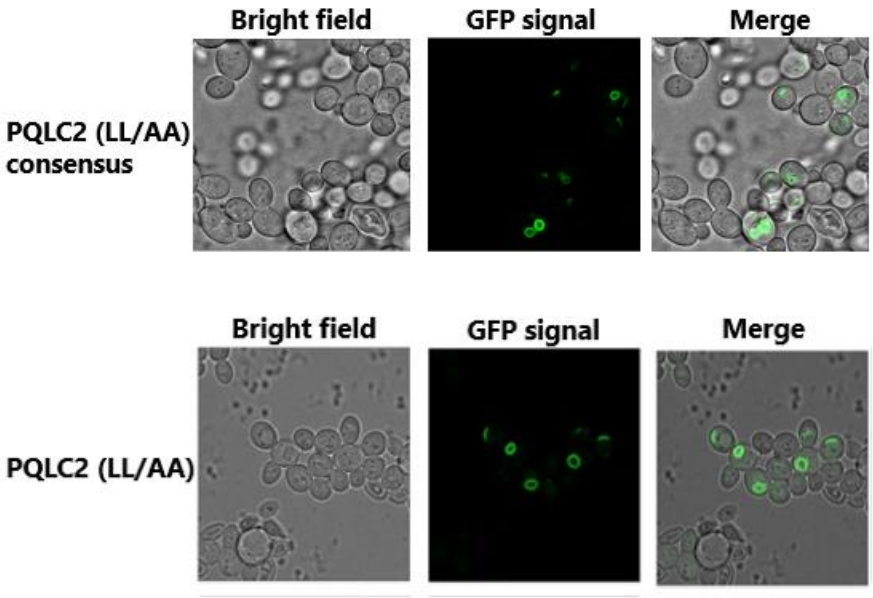

Figure 50. Expression of rat PQLC2 (LL/AA) consensus in *S. cerevisiae* strain W3031b Gal4-2. Fluorescent confocal microscopy of *S. cerevisiae* cells expressing PQLC2 (LL/AA) consensus-GFP. Images show that PQLC2 (LL/AA) consensus (upper panel) and PQLC2 (LL/AA) (lower panel) are located in the membranes of enclosed vacuole-like organelles. Images on left: bright field, middle: GFP signal and right: merge.

In addition, we performed a protein quantification assay in which we quantified the amount of PQLC2-GFP in membranes by quantifying the GFP fluorescence (see section **material and methods**). Our results shows that we have around 1.7 fold higher amount of PQLC2 (LL/AA) consensus-GFP compared to PQLC2 (LL/AA)-GFP (**Figure 51**).

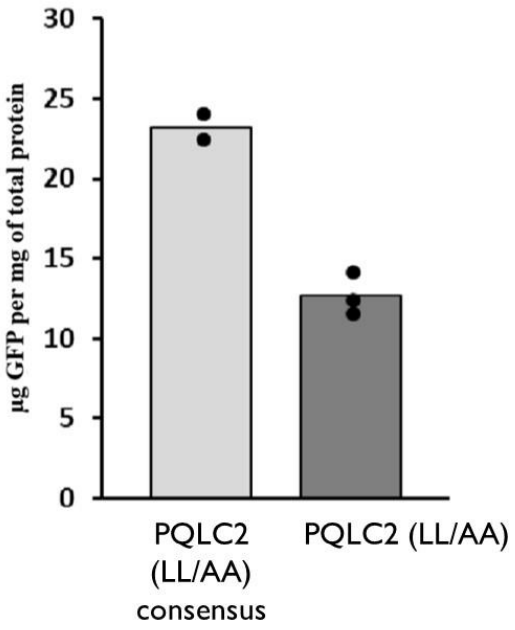

Figure 51. Total GFP quantification in P3 membranes expressing PQLC2 (LL/AA) or PQLC2 (LL/AA) consensus. The protein content in P3 membrane fractions of PQLC2 (LL/AA) or consensus was quantified by measuring fluorescence intensity, using purified GFP as a reference standard. The GFP fluorescence was used to generate a standard curve, allowing for the accurate determination of the protein concentration in each sample. Each data point shown represents an independent replicate to ensure the reliability of the measurements. Fluorescence was measured using an excitation wavelength of 485 nm and an emission wavelength of 535 nm.

4.5.2.2 Expression and purification of PQLC2 (LL/AA) consensus

We expressed and purified the PQLC2 (LL/AA) consensus as previously mentioned for PQLC2 (LL/AA). P3 membranes containing PQLC2 (LL/AA) consensus-GFP were solubilized in 2% (w/v) DDM/CHS and incubated with the GFP-Trap beads, then after a column washing steps, PQLC2 (LL/AA) consensus was eluted by incubating the column with hrv-3C protease O/N at 4°C, which cleaves between the C-terminal end of the transporter and the GFP, releasing only PQLC2 (LL/AA) consensus into the solution. The eluted fraction of PQLC2 (LL/AA) consensus was concentrated to around 50 µM and loaded into an SDS-PAGE gel and after Coomassie blue staining, 2 bands were detected corresponding to the monomer and dimer at around 25 kDa and 50 kDa, respectively.

(**Figure 52. A**). Excess of hrv-3C protease was also detected at around 50 kDa. Next, after concentrating the eluted fraction of PQLC2 (LL/AA) consensus, the protein was loaded into a Superose 6 column equilibrated with SEC buffer containing 0.02% (v/v) DDM. Remarkably, the chromatogram shows a relatively homogeneous peak corresponding to the PQLC2 (LL/AA) consensus with a main elution at around 15.5 mL, and the presence of empty DDM micelles and the hrv-3C between 16 and 16.5 mL (**Figure 52. B, upper panel**). To better characterize the SEC chromatogram, eluted fractions from 14.8 to 15.5 mL were collected, subjected to SDS-PAGE, and stained with Coomassie blue, showing PQLC2 (LL/AA) consensus at around 25 kDa and hrv-3C protease at around 50 kDa (**Figure 52. B, lower panel).** In conclusion, we have succeeded in expressing and purifying a consensus version of ratPQLC2 (LL/AA) with much better stability in DDM/CHS micelles than the wild-type LL/AA version. Unlike PQLC2 (LL/AA) (**Figure 39**), where the SEC peak of purified PQLC2 was asymmetric and non-homogeneous, the SEC profile of the PQLC2 (LL/AA) consensus is highly homogeneous and monodisperse, enabling us to perform functional and structural characterization.

A.

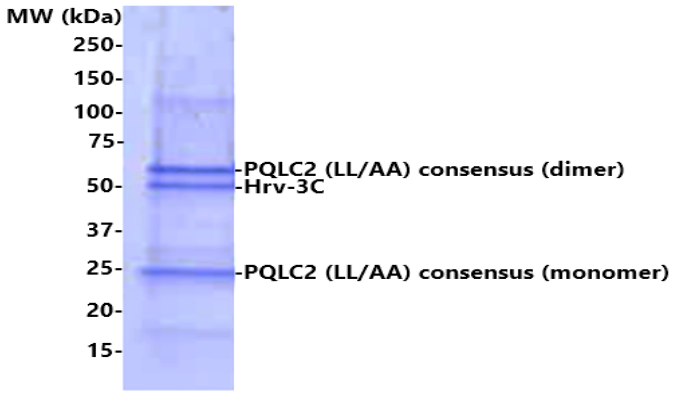

B.

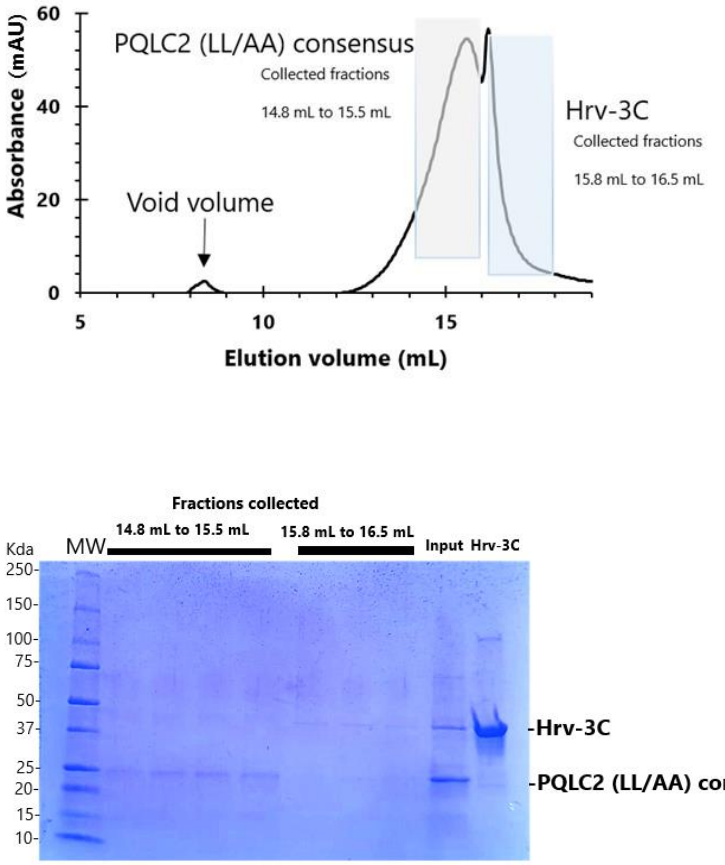

Figure 52. Purification and SEC characterization of PQLC2 (LL/AA) consensus. (**A**) The eluted purified PQLC2 (LL/AA) consensus was concentrated up to 50 µM and then loaded into SDS-PAGE gel, followed by Coomassie blue staining. Theoretical mass of PQLC2 is around 31 kDa. PQLC2 dimer and monomer were detected around 50 and 25 kDa, respectively. The Hrv-3C protease was detected around 50 kDa. (**B**) Upper panel: The concentrated PQLC2 (LL/AA) consensus was ultracentrifuged and 400 µL of supernatant was loaded onto a Superose 6 increase 10/300 GL column equilibrated with SEC buffer (containing 0.02% (v/v) DDM). Arrows indicate void volume, PQLC2, Hrv-3C and the collected fractions. (**B**) Lower panel: Collected fractions between 14.8 mL and 16.5 mL were loaded into SDS-PAGE gel followed by Coomassie blue staining. PQLC2 and hrv-3C proteins were detected at around 25 kDa and 37 kDa, respectively. Theoretical masses of: PQLC2 ≈ 31 kDa ; Hrv-3C protease ≈ 47.8 kDa.

4.5.2.3 Oligomerization state of PQLC2 (LL/AA) consensus

To investigate the oligomerization state of PQLC2 and its homogeneity in detergent micelles we carried out negative-staining electron microscopy studies (NS-EM) of the detergent-purified protein. Initial attempts of the non-consensus PQLC2 (LL/AA) version in DDM/CHS showed a significant background in the sample related to the detergent (DDM) and the CHS as well, previously reported in the literature (Gewering et al., 2018). We therefore decided to exchange detergents from DDM to LMNG taking into account the FSEC experiments (**Figure 47**). Attempts to exchange the detergent in the affinity column were unsuccessful since after equilibration with 0.015 % (v/v) LMNG in the GFP-Trap beads, either PQLC2 (LL/AA) or PQLC2 (LL/AA) consensus did not elute after Hrv-3C protease elution. We therefore decided to exchange the detergent in the SEC column. For this, we solubilized and purified PQLC2 (LL/AA) consensus in DDM and injected the purified (and concentrated) PQLC2 (LL/AA) consensus in the SEC column 0.015 % (v/v) LMNG.

As with DDM, the SEC profile in 0.015 % (v/v) LMNG shows a relatively homogenous peak corresponding to PQLC2 (LL/AA) consensus with a main elution at around 14.6 mL (**Figure 53. A**). We verified by SDS-PAGE gel followed by Coomassie blue staining the presence of PQLC2 as well as the presence of small amounts of the remaining Hrv-3C protease that was well separated from PQLC2 during the SEC (**Figure 53. B**). The freshly eluted sample at around 0.1 mg/mL was analyzed by NS-EM in our EM facility at the I2BC and also by our collaborators at the Instituto Biofisika (UPV/EHU, Spain). The experiments in Spain were done with freshly purified protein in their laboratory using our P3 membranes expressing PQLC2 (LL/AA) consensus-GFP and following our protocol. The particles observed in the micrographs obtained in both laboratories were very similar, although the micrographs taken in Spain show a better contrast and they are the ones presented in this thesis (**Figure 54**). The images reveal particles of relatively uniform size, with an average diameter of approximately 8 nm (**Figure 54. A**). This particle size is compatible with the size of the trimeric AlphaFold V2.0 model of

PQLC2 (**Figure 34. B**). The pLDDT or confident score of this model ranges between 80 and 90 in most of the residues of the PQLC2 predicted trimer with the exception of TM 4 and the loop connecting TMs 4 and 5. Interestingly, this model yielded an ipTM score of 0.83. ipTM measures the accuracy of the predicted relative positions of the subunits (or monomers) forming a protein complex. Values higher than 0.8 represent high confident predictions.

In conclusion, the use of PQLC2 (LL/AA) consensus has enabled us to obtain for the firSt time structural information of PQLC2. NE-EM studies of detergent purified PQLC2 (LL/AA) consensus suggest that this transporter oligomerizes, probably as a trimer.

A.

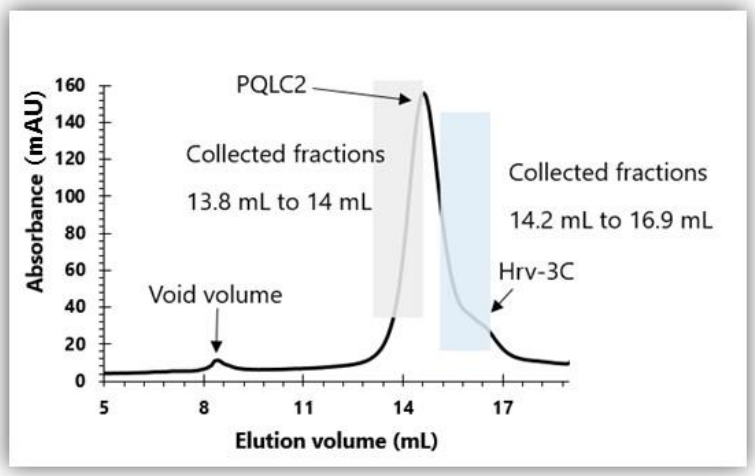

B.

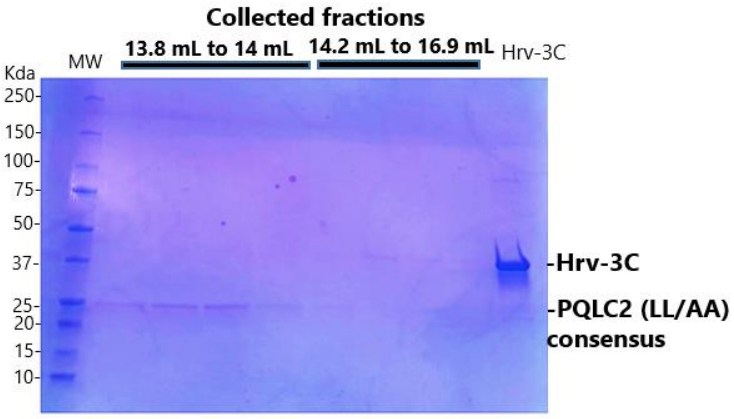

Figure 53. Purification of PQLC2 (LL/AA) consensus in DDM followed by detergent exchange to LMNG. (**A**) After purification in DDM, the eluted sample was concentrated to 2 mg/mL, then ultracentrifuged and 400 µL of supernatant was loaded onto a superose 6 increase 10/300 GL column equilibrated with SEC exchange buffer (containing 0.015% (v/v) LMNG). Void volume, hrv-3C and PQLC2 (LL/AA) consensus are indicated by arrows. (**B**) Collected fractions of 200 µL between 13.8 mL and 16.9 mL were analyzed by SDS-PAGE gel followed by Coomassie blue staining. PQLC2 (LL/AA) consensus and hrv-3C proteins were detected at around 25 kDa and 37 kDa, respectively.

A.

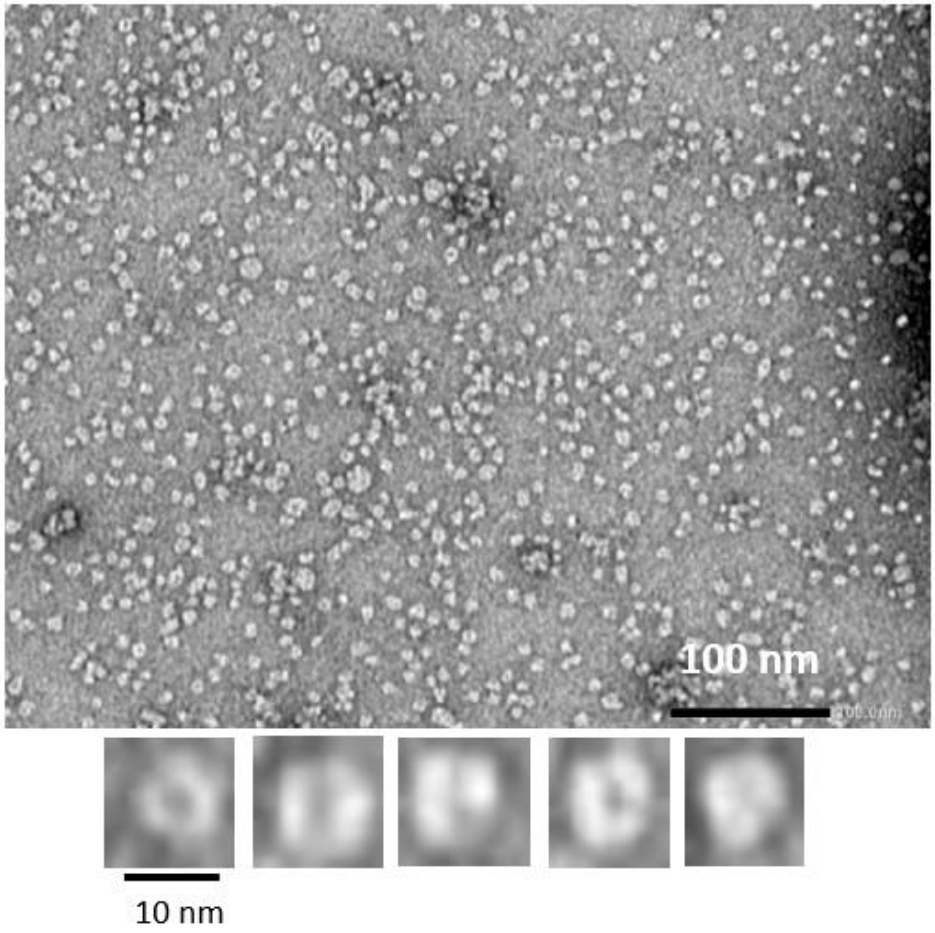

B.

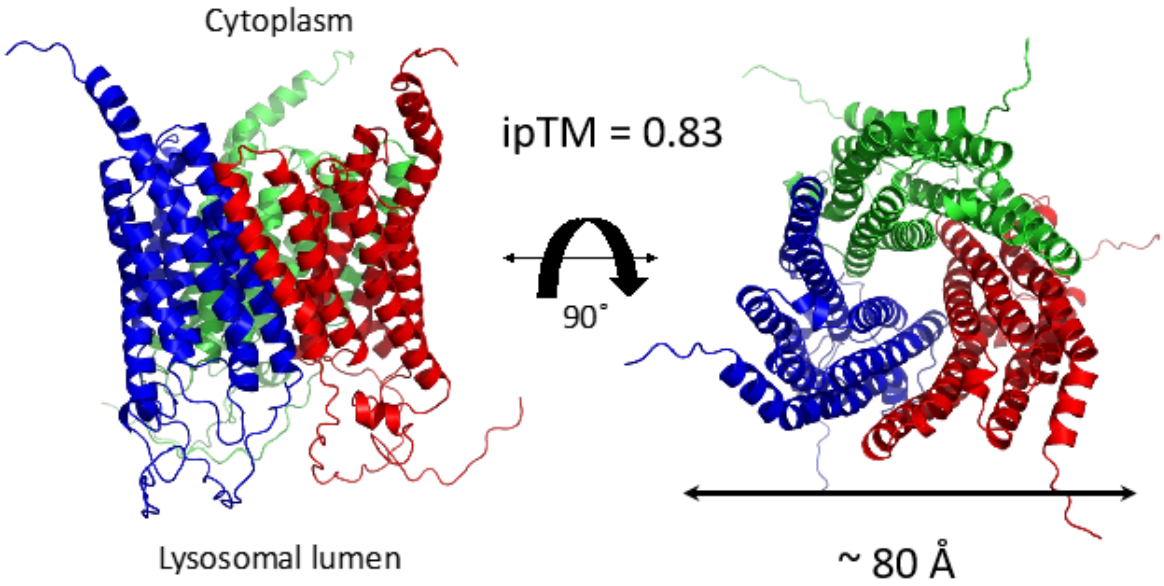

Figure 54. Oligomerization state of PQLC2 (LL/AA) consensus. (**A**) NS-EM Micrograph of PQLC2 (LL/AA) consensus obtained in 0.015 % (v/v) LMNG. After purification, the eluted fraction was concentrated to 2 mg/mL then ultracentrifuged (1h at 145,000 x g, 4°C). 400 µL of supernatant was loaded onto a Superose 6 increase 10/300 GL column equilibrated with SEC exchange buffer. The eluted peak corresponding to PQLC2 (LL/AA) consensus was then collected and NS-EM was carried out. NS-EM micrographs show PQLC2 particles of around 8-10 nm. For clarity, some particles were magnified and displayed at the bottom of the figure (**B**) Lateral and cytoplasmic-faced PQLC2 AlphaFold V2.0 trimeric model. Each monomer is represented by a different color.

4.6 PQLC2 (LL/AA) RECONSTITUTION IN LIPSOSOMES AND TRANSPORT ASSAY

Studies using recombinant rat PQLC2 (LL/AA) expressed in the *Xenopus* oocytes' plasma membrane have demonstrated that PQLC2 specifically accumulates [^{3}H]L-arginine, [^{3}H]L-lysine and [^{3}H]L-histidine in a time-dependent manner and that transport activity is not coupled with protons, although it is regulated by the pH (Leray et al., 2021). Another study based on whole cell transport assays in COS-7 cells overexpressing human PQLC2 (LL/AA) in the plasma membrane has also shown that PQLC2 selectively transport cationic amino acids (B. Liu et al., 2012).

However, PQLC2 has never been purified from a recombinant host or lysosome for functional or structural characterization. As these previous functional experiments of PQLC2 were performed in whole cells, the interaction of other transporters or mediators cannot be ruled out. Thus, one of the aims of this thesis was to study the transport activity of isolated PQLC2 reconstituted in proteoliposomes.

We reconstituted detergent-purified PQLC2 (LL/AA) or PQLC2 (LL/AA) consensus in liposomes composed of a phospholipid mixture of DOPC and DOPE (see **III. Material and methods**). Our protocol for detergent-purified PQLC2 (LL/AA) reconstitution proved to be successful since (i) Western blot analysis of the reconstituted proteoliposomes shows a band at 25 kDa corresponding to the PQLC2 protein that is not observed in empty liposomes (**Figure 55. A**); (ii) glycerol-based density gradient experiments of liposome-reconstituted PQLC2, showed that PQLC2 is successfully incorporated into the lipid bilayer in a non-aggregated form (**Figure 55. B**), and (iii) through Dynamic Light Scattering (DLS), we observed that the proteoliposomes exhibited a consistent size distribution with a low polydispersity index (PDI), confirming their homogeneity and uniformity in the prepared sample.

In the transport assay, we stablished a pH gradient across the lipid bilayer (acidic pH 5.5 outside and neutral pH 7.5 on its interior), mimicking in this way the lysosomal lumen and the cytosol, respectively (**Figure 32**). As shown in the literature, the

accumulation of cationic amino acids by PQLC2 in *Xenopus* oocytes is pH-dependent, with no transport activity observed at extracellular pH above 7 (compartment equivalent to the lysosomal lumen). We also generated during the transport experiments a transient transmembrane potential (negative at the interior) by establishing a gradient of K^+ across the artificial membrane and incubating the proteoliposomes with valinomycin (see **III. Material and methods**) (**Figure 31**). Arginine or Lysine uptake was initiated by mixing liposomes (control samples) or proteoliposomes with a transport buffer containing 50 to 100 µM cold L- Arg/L-Lys, 0.5 µCi [^{3}H]L-Arg or L-Lys. The quantification of the time-dependent amino acid accumulation in the liposomes at different times was carried out by stopping the reaction at pH 7.5 followed by rapid filtration and quantification of the accumulated radioactivity (see **methods section**). Experiment was done in sample replicates. **Figure 56. A** shows that, compared to empty liposomes, in these experimental system, PQLC2 is able to uptake a small amount of [^{3}H]L-Arg, although between 5 to 10 min the system reaches the equilibrium. Unfortunately, at time 0 we can see that there is [^{3}H]L-arg, this is due to experimental error resulting from the fact that the reaction was not stopped directly. Similar results were obtained using [^{3}H]L-Lys where liposome-reconstituted PQLC2 was able to accumulate a small amount of L-Lys. Again, between 5 and 10 min PQLC2-mediated and non-specific [^{3}H]L-Lys accumulation were similar (**Figure 56. B**). Unfortunately, these experiments were very poorly reproducible. The fact that the uptake of either [^{3}H]L-Arg or [^{3}H]L-Lys into proteoliposomes is fairly low might be due to different factors. One, perhaps, is the low activity of reconstituted detergent-purified PQLC2, a common problem of membrane transporters. On the other hand, PQLC2 has a reported low affinity for L-Arg as the apparent K_m of PQLC2 for L-Arg transport in *Xenopus* oocytes is in the order of 3.8 mM (Jézégou et al., 2012). This low affinity presents a significant challenge when using radiolabeled substrates in transport experiments, as the relatively high concentrations required for detectable transport lead to increased costs and potential security concerns related to handling radioactivity. Nevertheless, we tested increasing concentration of cold (up to 300 mM)

and tritiated substrates (up to 1 µCi), but unfortunately, the results remained highly variable and difficult to interpret.

It is worth mentioning that as a proof of concept of our transport assay we performed L-Arg transport in proteoliposomes reconstituted with the bacterial L-Arg/agmatine antiporter AdiC (Kowalczyk et al., 2011). This approach was chosen to optimize the assay conditions and to use a previously characterized functional transporter as a reference for validating the experimental setup.

A.

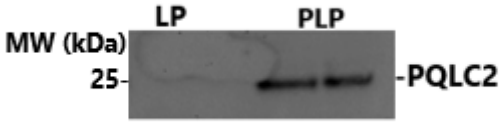

B.

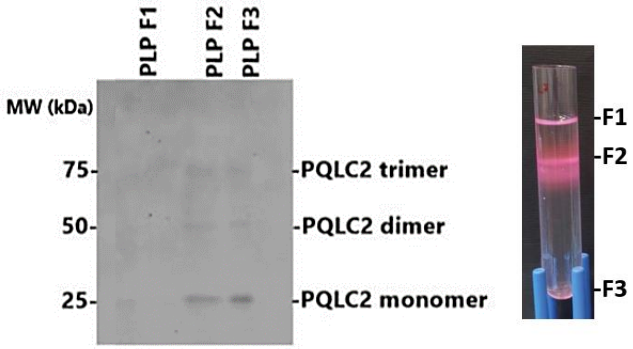

Figure 55. **PQLC2 (LL/AA) reconstitution in liposomes.** (**A**) Western blot essay of empty liposomes (LP) or reconstituted with PQLC2 (LL/AA) (PLP). PQLC2 (LL/AA) of around 25 kDa was detected. (**B**) Glycerol gradient tube showing the three fractions F1 (top), F2 (middle) and F3 (bottom) (right). Western blot of F1 and F2 shows the presence of PQLC2 as monomer, dimer and trimer in the PLPs of F1, 2 and 3. Rabbit anti-PQLC2 primary antibody targeting the cytoplasmic loop (1-8) was used for both Western blot assays.

A.

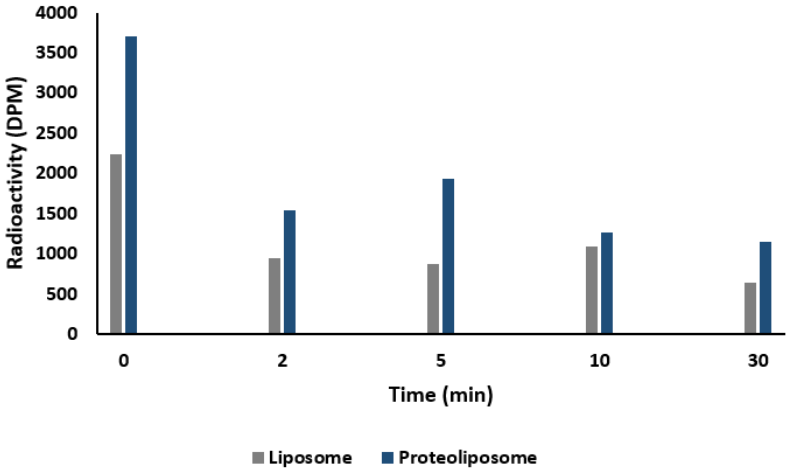

B.

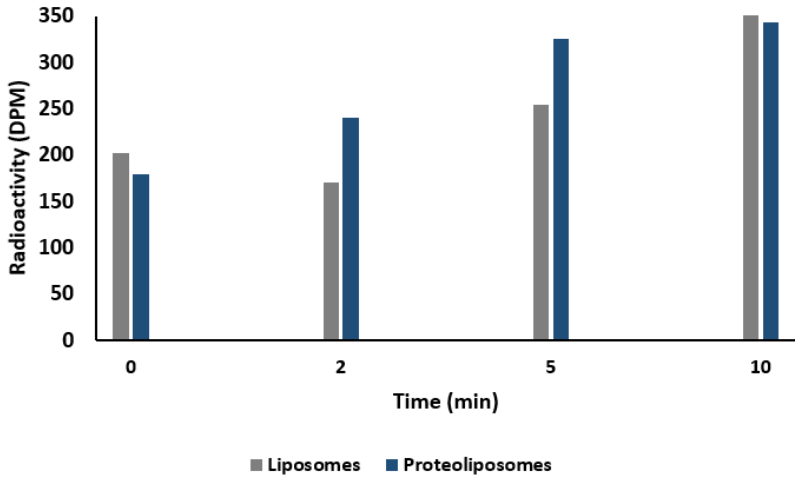

Figure 56. Radioactivity uptake of [^{3}H]L-Arg or proteoliposomes reconstituted with PQLC2 consensus. The uptake assay was initiated by adding 0.5 µCi of [^{3}H]L-Arg (50 µM L-Arg (cold)) to the system in panel (**A**), or 0.5 µCi of [^{3}H]L-Lys (100 µM Lys (cold)) in panel (**B**). Measured radioactivity (DPM) is plotted as a function of reaction time (min) under two conditions: in gray, empty liposomes (without PQLC2) or proteoliposomes (reconstituted with PQLC2) in blue. Experiment was carried out in replicates.

4.7 INTERACTION BETWEEN WDR41-7CD LOOP AND PURIFIED PQLC2 (LL/AA) CONSENSUS USING EPR

As mentioned previously (see **I. Introduction**), immunoprecipitation and pull-down assays using KO and mutated versions of WDR41 identified a 10-amino acid motif (TIP: TGFFNMWGFG) (**Figure 14**) within the WDR41-7CD loop as the necessary and sufficient motif for the recruitment of the CSW complex by PQLC2 to the lysosomal membrane (Talaia et al., 2021). In this chapter Electron Paramagnetic Resonance (EPR) spectroscopy was used to experimentally validate the direct interaction between WDR41-7CD loop and purified PQLC2 in the absence of other cellular components. To achieve this, we used purified PQLC2 (LL/AA) consensus and synthetic WDR41-7CD loop peptides composed of the TIP sequence and its flanking regions (see **III. Material and methods, B. Methods, part 21, Table 6**). Finally, to investigate the specificity of the TIP sequence, we used mutated versions of this peptide known to inhibit PQLC2/WDR41 interaction (see **I. introduction**).

4.7.1 Principles of EPR and SDSL

EPR is used to study paramagnetic centers, i.e. chemical species carrying unpaired electrons. EPR is a powerful technique for studying various aspects of proteins, such as protein dynamics, protein/protein interactions and protein structure (Roessler & Salvadori, 2018) (Torricella et al., 2021). EPR can be used to study proteins in complex environments which make it ideally suited to the study of membrane proteins, particularly in their native environment (Claxton et al., 2015) (Sahu & Lorigan, 2020a) (Möbius et al., 2005). The paramagnetic centers can be native to the macromolecule as in the case of metalloproteins carrying transition metal ions or proteins that hold organic radicals (Britt et al., 2004) (Calvo et al., 1990) (Bhattacharjee et al., 2011). Proteins lacking such centers, which is the case for PQLC2 and WDR41-7CD loop, can be studied by the specific introduction of paramagnetic species centers by site-directed spin labeling (SDSL) (Cornish et al., 1994). The basis of this approach is to chemically

link a spin label, typically a nitroxide radical, to the protein of interest via a cysteine residue that is present natively or introduced by standard site-directed mutagenesis (Lorigan, G. A., 2018) (Torricella et al., 2021). In our approach, a cysteine residue was introduced into chemically synthesized WDR41-7CD loop peptides at different positions, and a proxyl nitroxide spin label was linked to them using maleimide-cysteine chemistry (**Figure 57**) (see section **material and methods**).

The room temperature EPR of the nitroxide radical depends on its rotational correlational time (τ_c), this is the molecular re-orientation of the nitroxide with respect to the applied magnetic field. Therefore, the correlation time reflects the movement of the nitroxide which in turn provides information about the flexibility of its environment (Schweiger, A., 2007). To illustrate this, **Figure 58** shows how restricting the mobility of a free nitroxide radical by increasing the viscosity of the solution leads to EPR spectral changes. When the nitroxide is attached to the protein via a linker, its EPR spectral shape depends on the movement of the label relative to the protein backbone, the fluctuations in the α-carbon backbone, and the rotational movement of the protein as a whole (**Figure 59**) (Sahu & Lorigan, 2020). However, in practice, due to the slow movement of the protein or peptide, the EPR spectrum mostly reflects the degree of freedom of the bonds between the nitroxide spin label and the macromolecule (Smirnova & Smirnov, 2015). As a consequence, any specific interaction between the label and the protein can also be detected in the EPR spectrum. For example, the rotational correlation time of a spin label fixed in a unique position with respect to the protein, due to steric effects or specific interactions, will be similar to the correlation time of the protein itself. However, if the bonds that connect the spin label to the protein are free to rotate then the rotational time of the spin label will be faster than that of the protein to which it is attached.

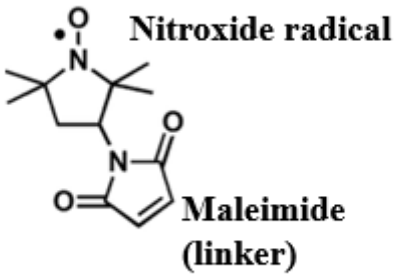

Figure 57. Structure of the 3-Maleimido-PROXYL nitroxide spin label used in SDSL to label the single and double cysteine WDR41-7CD loop peptides.

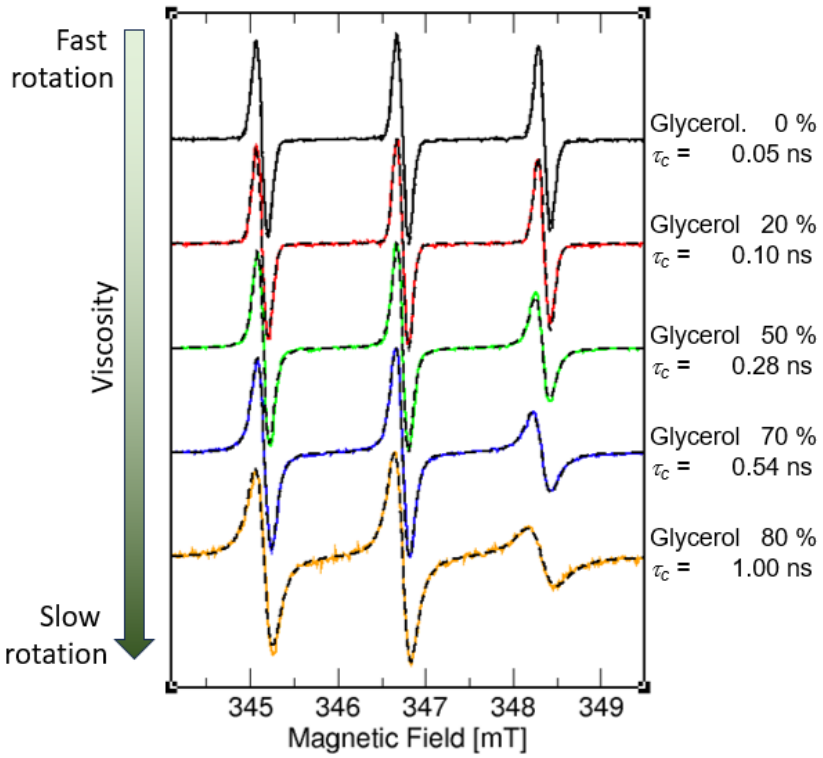

Figure 58. Increasing the viscosity of the solution leads to nitroxide EPR spectral changes. Using different glycerol concentrations (0%, 20%, 50%, 70% and 80% (w/v)), nitroxide spin label motility decreases, leading to different rotational correlational times (τc).

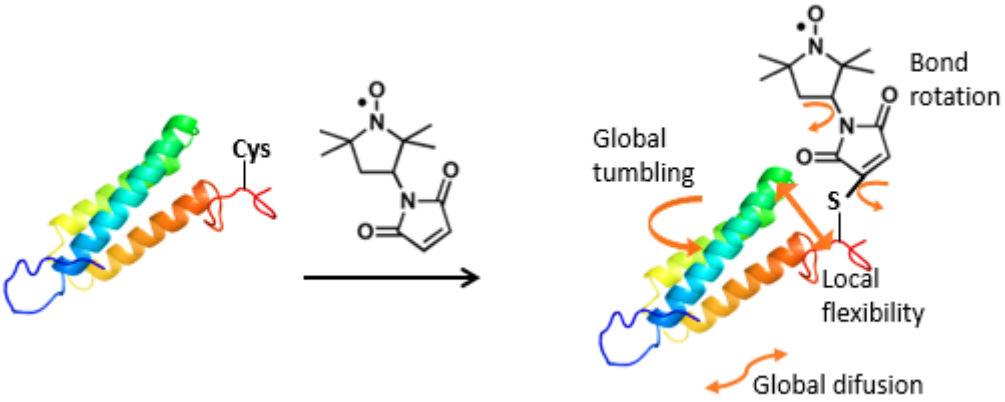

Figure 59. The correlation time of the protein-bound nitroxide group measured by EPR is the result of various effects.

Although the described effects are in general visible in the spectra, the spectra are often fitted to obtain the rotational correlation time and quantify the different components in cases where more than one species is present. The EPR spectrum of the free spin label moving rapidly through the solution is characterized by 3 equal resonances (top spectrum, **Figure 60)** (Sahu & Lorigan, 2020). Under these conditions, the rapid movement leads to an isotropic signal, which splits into three due to the interaction of the unpaired electron with the ^{14}N nucleus of the nitroxide, which has a nuclear spin of 1 (i.e it can adopt the -1, 0, and +1 states, splitting the resonance of the unpaired electron in three). As the motion of the nitroxide is impeded, the spectrum become anisotropic, this is the resonance of the unpaired electron depends on its orientation relative to the spectrometer's magnetic field. This results in a much broader signal (lowest spectrum, **Figure 60**) (Sahu & Lorigan, 2020). These spectral changes can be used to study the interaction of the nitroxide with nearby objects, for instance peptides or proteins. Narrow linewidth indicates that the spin label undergoes fewer interactions with surrounding molecules, suggesting greater mobility and fewer restrictions on movement. Whereas, wide linewidth indicates greater interactions, possibly due to conformational constraints, aggregation or a more rigid environment,

suggesting lower mobility (Claxton et al., 2015) (Klug, C. S., & & Feix, J. B., 2005) (**Figure 60**).

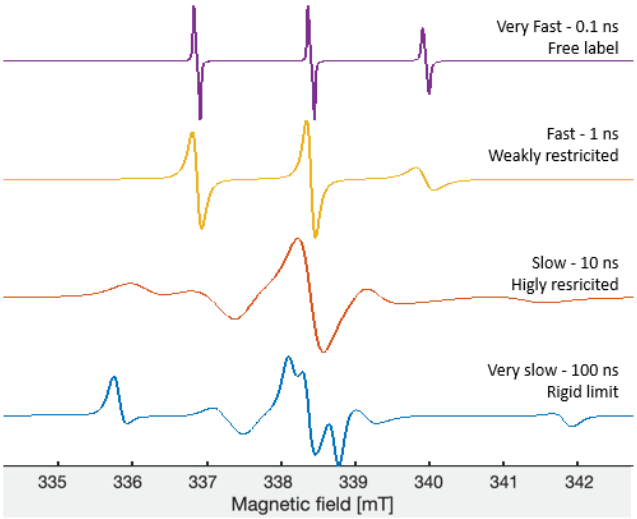

Figure 60. The binding properties of the protein/peptide and can be investigated by measuring the changes in spin-label mobility.

4.7.2 Binding of PQLC2 (LL/AA) consensus to WDR41-7CD loop

The EPR spectrum of a freely tumbling, unattached nitroxide radical typically exhibits a sharp triplet structure with equal intensities and narrow linewidth (0.1 ns in **Figure 60**). When a nitroxide radical is bound to a protein, its ability to move freely is restricted. This impeded movement leads to changes in the EPR spectrum as a result of a decrease on the nitroxide rotational correlation time. The two unequal triplet spectra shown in **Figure 61** demonstrate unequivocally that the nitroxides are bound to the synthetic peptide encoding WDR41-7CD loop via the introduced cysteines at positions 8 and 20 of the peptide. The spectra of **Figure 61** correspond to a rotational correlation time of about ~1 ns as the simulated one in **Figure 60**. The crucial first spin-labeling step was therefore successful.

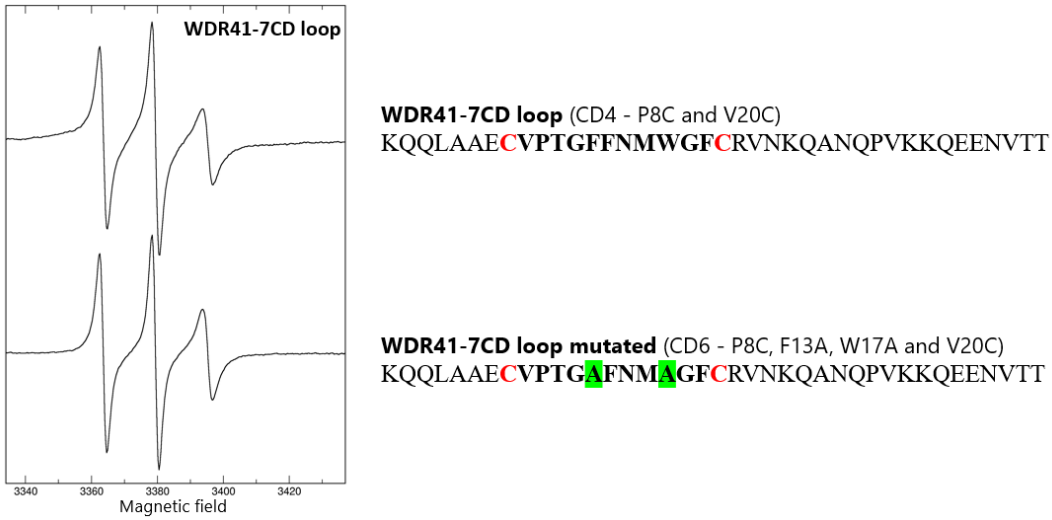

Figure 61. EPR spectra of the loop WDR41 (CD8 – P8C) and loop WDR41 (CD6 – P8C, F13A, W17A, V20C) labeled with the nitroxide group at around 31 µM.

Notably, the EPR spectrum of nitroxide bound to WDR41-7CD loop undergoes further changes in the presence of an equimolar quantity of purified PQLC2 (LL/AA) consensus (**Figure 62**). As observed in the **Figure 62**, a pronounced resonance was evident at the lower field end of the spectrum. This is indicative of a low mobility nitroxide (similar to the simulated 10 ns in **Figure 61**). In addition, in the same spectrum, a component resembling the free peptide was also present. In contrast, no changes were observed when adding purified PQLC2 (LL/AA) consensus to the mutated WDR41-7CD loop (upper panel versus lower panel, **Figure 62**). This mutated version, besides the cysteines at positions 8 and 20, where the nitroxide is bound, contains two other mutations as well: F13A and W17A. These single-point mutations within the WDR41-7CD loop, identified by Ferguson and colleagues (Talaia et al., 2021) in their pull-down assays, inhibit the interaction between the CSW complex and PQLC2 at the lysosomal membrane in cell culture experiments. Therefore, we can associate the low mobility component of the nitroxide labeled WDR41-7CD loop in the presence of purified PQLC2 (LL/AA) consensus with the binding of WDR41-7CD loop with the transporter since mutations known to disrupt this interaction (F13A and W17A) abolish this low mobility component in the nitroxide spectrum (**Figure 62**).

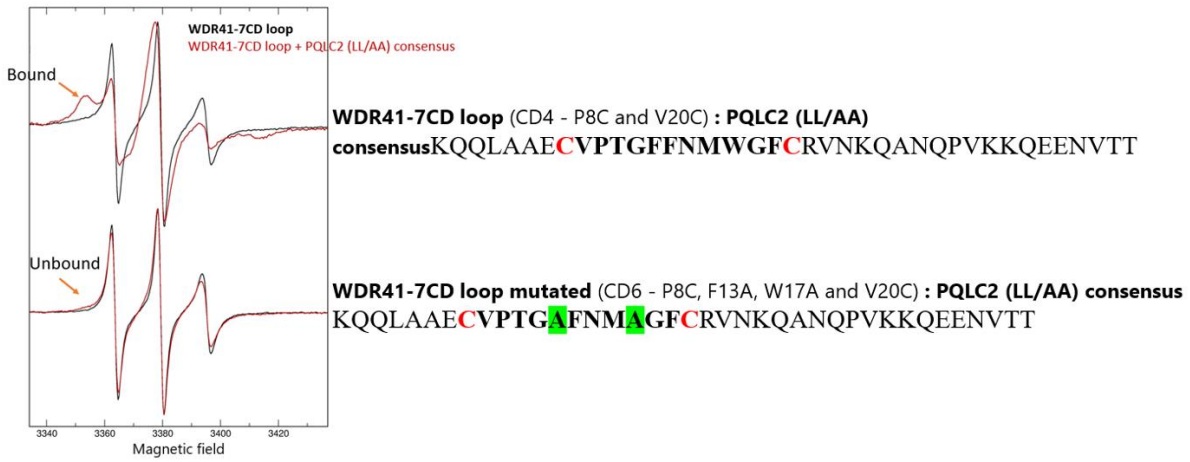

Figure 62. The EPR spectra of the nitroxide-labeled WDR41-7CD loop changes in the presence of purified PQLC2 (LL/AA) consensus. The bound (low mobility) and unbound (high mobility) fractions are indicated by arrows. The black line corresponds to the spectrum of WDR41-7CD loop (31 μM) alone whereas the red line is the spectrum in the presence of purified PQLC2 (LL/AA) consensus (35 μM). The upper spectrum corresponds to the WDR41-7CD loop labeled with the nitroxide at position 8 (CD8 - P8C), while the lower spectrum corresponds to the mutated WDR41-7CD loop (F13A, W17A), labeled with the nitroxide group at positions 8 and 20 (P8C, V20C).

4.7.3 The position of the spin label site in the WDR41-7CD loop affects its EPR spectrum upon PQLC2 (LL/AA) consensus binding

We further characterized the interaction between the WDR41-7CD loop and purified PQLC2 (LL/AA) consensus by investigating the EPR spectrum of the nitroxide group at different positions along the WDR41-7CD loop upon binding to purified PQLC2 (LL/AA) consensus. Modifications of the nitroxide EPR spectrum can reveal useful information about the local environment where this radical is located in the WDR41-7CD loop/PQLC2 bound state. Therefore, we can use this information to map the region of WDR41-7CD loop critical for PQLC2 interaction, where the mobility of the nitroxide group is more restricted. As predicted, the low mobility component of the nitroxide group in the presence of purified PQLC2 (LL/AA) consensus changed as a function of its position along the WDR41-7CD loop (**Figure 63**). In the EPR spectra of WDR41-7CD

loop peptides CD1 and CD7, the low mobility component was less pronounced compared to those of the CD2 and CD8 WDR41-7CD loop peptides (**Figure 63**). This can be explained by the fact that the spin label in CD1 and CD7 WDR41-7CD loop is positioned farther from the TIP region, compared to its position in CD2 and CD8 WDR41-7CD loop. We modeled the PQLC2/WDR41-7CD loop complex using with AlphaFold V2.0 and observed that, in this model, the spin label in the CD1 and CD7 WDR41-7CD loop peptides is more exposed to the solvent compared to the CD2 and CD8 WDR41-7CD loop peptides, where the nitroxide group is located deeper within the binding cavity of PQLC2 (**Figure 64**). Therefore, in CD2 and CD8, the movement of the label will be more restricted than for CD1 and CD7. Another possibility is to consider the slow and fast component as an equilibrium between the label exposed to the solvent, where the linker is free to rotate, and the label interacting with the protein, where its movement is restricted. Again, the closer the label is to the binding pocket, the higher the chances of interacting with PQLC2. In this way, in C1 and CD7, the equilibrium shifts toward the fast component, while in CD2 and CD8, it shifts toward the slow component.

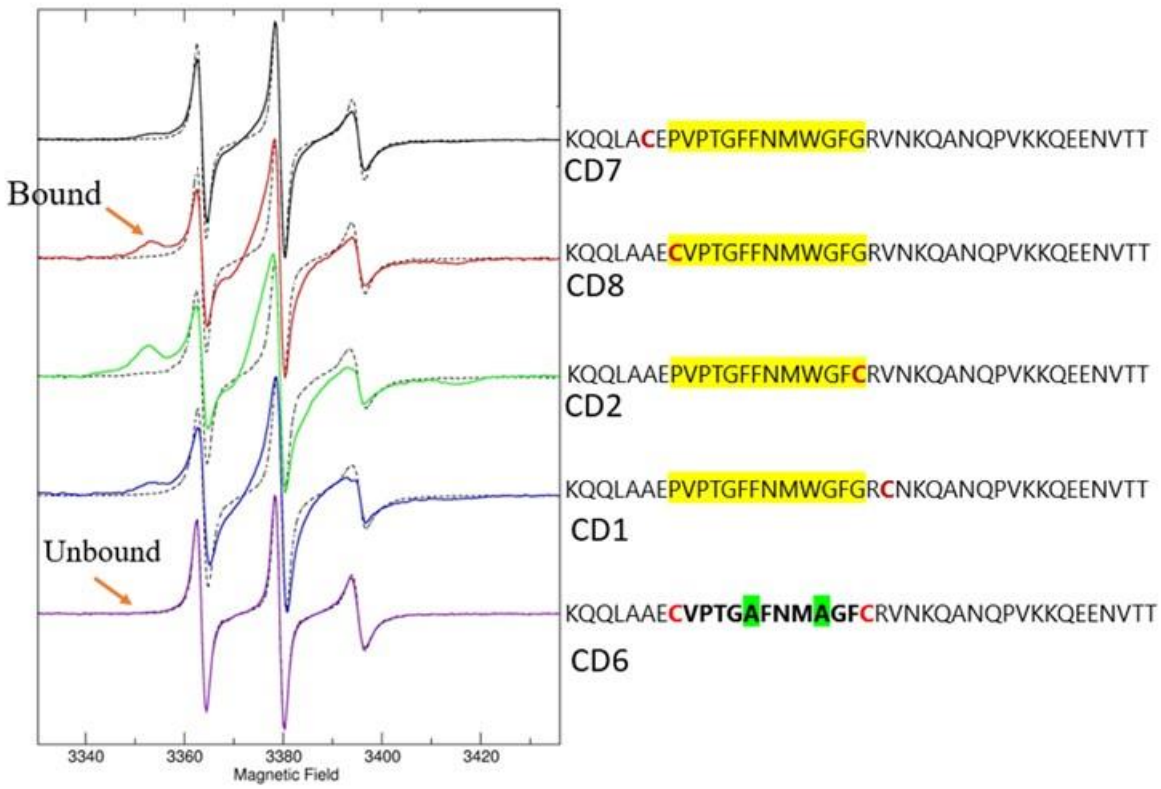

Figure 63. Mapping WDR41-7CD loop/PQLC2 interaction by monitoring changes of the nitroxide EPR spectrum at different positions of the WDR41-7CD loop peptide. Upon binding to purified PQLC2 (LL/AA) consensus (35 μM) the spectrum of the nitroxide group at different positions of WDR41-7CD loop (31 μM) changes reflecting different local mobility or solvent accessibility of the spin label along the peptide. Cysteine residues (in red) were introduced at different positions of WDR41-7CD loop for spin-labeling. The cysteines in CD1 and CD7 are located outside the TIP region of WDR41-7CD loop, whereas in the CD2 and CD8 peptide, the cysteine residues are in the TIP region. Mutated CD6 WDR41-7CD loop peptide (CD6 – P8C, F13A, W17A, V20C) in the TIP region was used as a control (lowest spectrum).

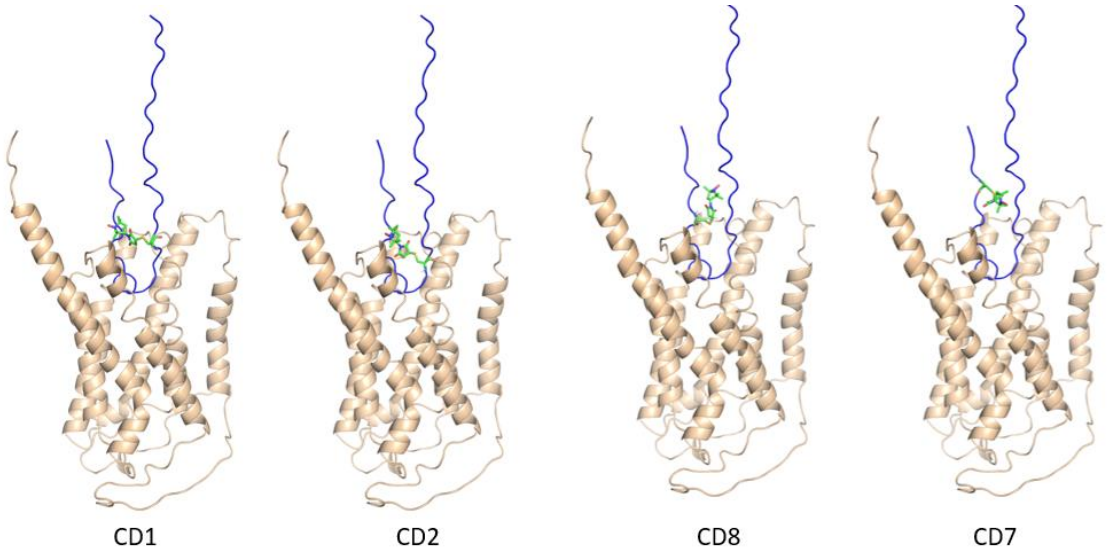

Figure 64. AlphaFold V2.0 model of WDR41-7CD loop/PQLC2 complex. AlphaFold V2.0 model of PQLC2 (in beige) and the WDR41-7CD loop (in blue). The spin labels were introduced on the AlphaFold V2.0 model using Pymol. In this model, the spin labels of CD1 and CD7, located outside the WDR41-7CD loop TIP region, are predicted to be more exposed to the solvent, whereas the spin labels of CD2 and CD8 are predicted to localize deeper within the central cavity of PQLC2.

4.7.4 Competition experiments with unlabeled WDR41-7CD loop

The subsequent objective was to determine whether the interaction between the labeled WDR41-7CD loop and purified PQLC2 (LL/AA) consensus is specific and not driven by the presence of the nitroxide group. By introducing an excess of unlabeled WDR41-7CD loop peptide, we assessed whether it could indeed compete with the labeled WDR41-7CD loop for the binding site in PQLC2. If the unlabeled peptide competes with the labeled peptide, we can expect a decrease in the low-mobility signal.

Figure 65 shows that the addition of the unlabeled WDR41-7CD loop alters the EPR spectrum, by decreasing the low-mobility resonance component of the spectrum (**Figure 65**, comparison of red and green spectra). This result implies that the unlabeled WDR41-7CD loop and labeled CD8 WDR41-7CD loop peptides compete for the same

binding site. The remaining low-mobility resonance (green line, **Figure 65**) can be explained by a residual binding of CD8 WDR41-7CD loop. If a similar affinity is assumed for both peptides, adding a 5-times excess of unlabeled WDR41-7CD loop leaves a residual of ~20% of CD8 WDR41-7CD loop still bound to PQLC2 (LL/AA) consensus. These results indicate that the interaction of PQLC2 (LL/AA) consensus with the labeled WDR41-7CD loop peptides is not driven by an unspecific interaction of the spin label.

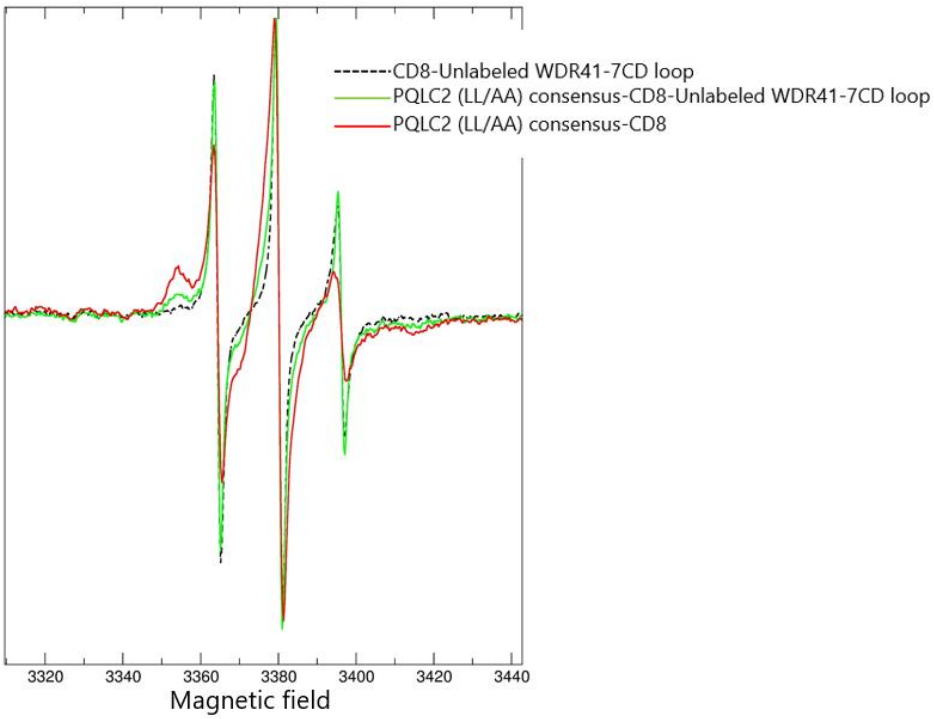

Figure 65. Competition binding assay between unlabeled and labeled WDR41-7CD loop peptides. The unlabeled WDR41-7CD loop peptide competes with the labeled WDR41-7CD loop peptide for the binding site on purified PQLC2 (LL/AA) consensus. The molar ratio of labeled WDR41-7CD loop/PQLC2/ unlabeled WDR41-7CD loop was 0.9 : 1 : 5. The black line represents the spectrum of CD8 with the unlabeled WDR41-7CD loop, the green line represents the spectrum after adding purified PQLC2 (LL/AA) consensus; the red line represents the spectrum of CD8 with PQLC2 (LL/AA) consensus.

4.7.5 WDR41-7CD loop might interact with PQLC2 (LL/AA) consensus in different poses

As described earlier, the binding of the labeled peptide to PQLC2 (LL/AA) consensus results in the clear appearance of a low mobility component superimposed to another component similar to that of the free peptide; however, the nature of this component seems to be more complex. This might reflect multi-conformational states of WDR41-7CD loop after binding to PQLC2 (LL/AA) consensus. To better understand the nature of this component, titration experiments were conducted by adding increasing concentrations of CD8 WDR41-7CD loop to the purified PQLC2 (LL/AA) consensus (**Figure 66**). To obtain a good fitting of these spectra three components were required (**Figure 67**): (i) a « free » component that represents the spin-labeled WDR41-7CD loop that is not bound to PQLC2 (LL/AA) consensus (ii) a « fast » component where the WDR41-7CD loop is bound to PQLC2 (LL/AA) consensus, but in a conformation that allows the nitroxide to rotate rapidly and (iii) a « slow » component in which the movement of the nitroxide is highly restricted due to its interaction with PQLC2 (LL/AA) consensus (**Figure 66**). As schematized in **Figure 68**, the “fast” and “slow" components of the nitroxide EPR spectrum can be interpreted as representing the different conformations that the WDR41-7CD loop might adopt within the binding site of PQLC2 (LL/AA) consensus. **Figure 67** shows the results of the fitting using these three components —slow, fast, and free— to assess their individual contributions in the CD8 titration experiment. This approach was employed to quantify the relative proportions of each component. As expected, the fraction of “free” peptide increases with increasing ratios of peptide: PQLC2 reaching ~30% at 1.6:1 ratio (**Figure 69**). At this ratio, the amount of bond peptide (slow+fast) was ~0.70, comparable with the expected 62% (1/1.6=0.62), indicating that the peptide binds to PQLC2 stoichiometrically. The equilibrium between the fast and slow components appeared to be independent on the peptide:PQLC2 ratio (**Figure 69**).

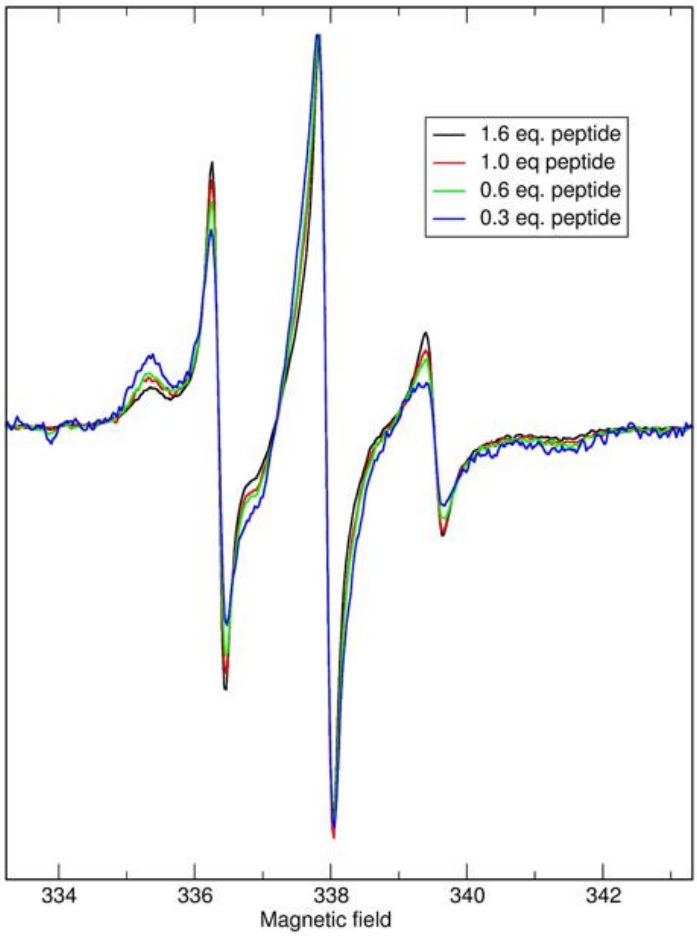

Figure 66. EPR spectra of the titration experiment of CD8 WDR41-7CD loop with purified PQLC2 (LL/AA) consensus. A titration experiment was performed by adding increasing concentrations of CD8 WDR41-7CD loop peptide to PQLC2 (LL/AA) consensus. The black, red, green, and blue lines in the resulting spectra correspond to the concentrations of 1.6, 1, 0.6, and 0.3 equivalents of the peptide, respectively, relative to PQLC2 (LL/AA) consensus. The CD8 WDR41-7CD loop peptide contains a single cysteine at position 8, where the nitroxide spin label binds within the TIP region.

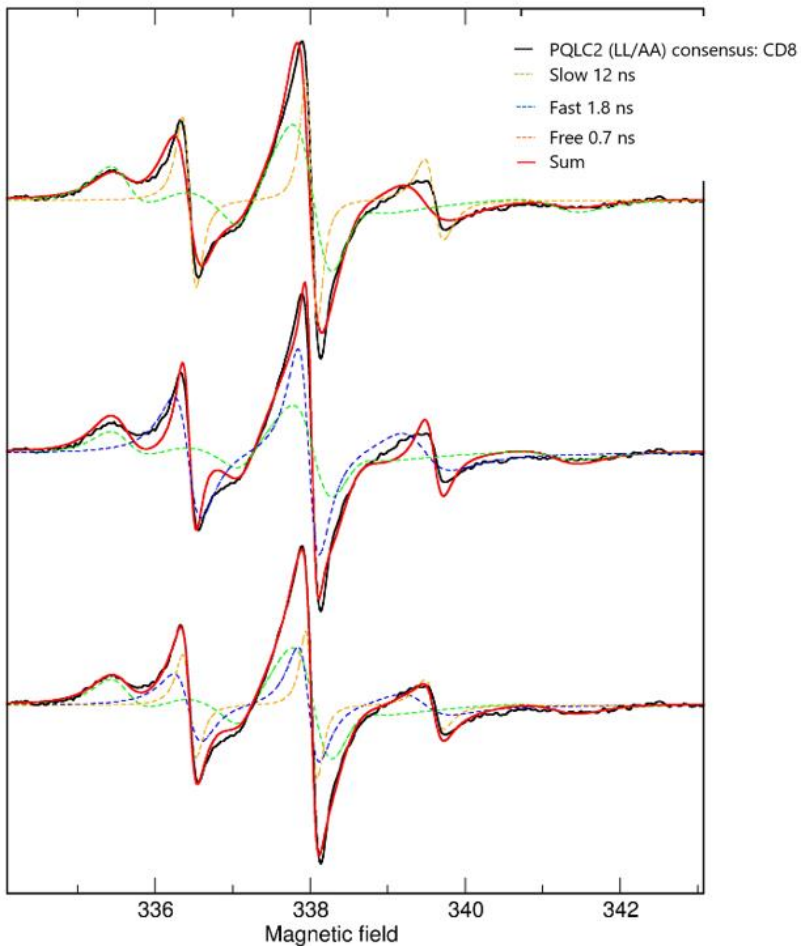

Figure 67. The fitting between PQLC2 (LL/AA) consensus and CD8 WDR41-7CD loop. The top spectrum shows the fit with only the slow and free components, the middle spectrum with the slow and fast components, and the bottom spectrum with all three: slow, fast, and free components. The best fit is obtained using all three components (shown in the bottom spectrum). The black line represents the PQLC2 (LL/AA) consensus spectrum with the CD8 WDR41-7CD loop, while the green, blue, and orange lines correspond to the slow (12 ns), fast (1.8 ns), and free (0.7 ns) components, respectively. The red line represents the sum of all components

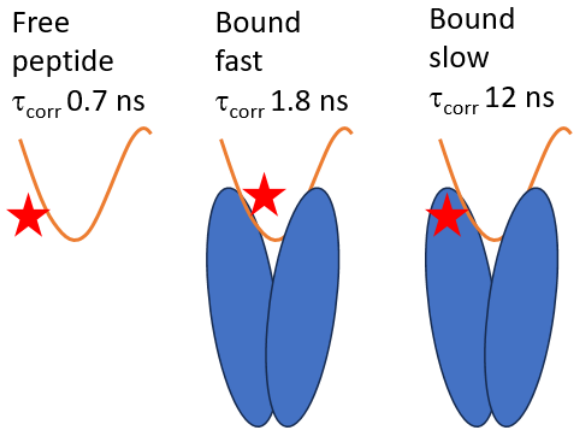

Figure 68. Schematic diagram showing the three components: the free peptide, the slow bond and the fast bond. The scheme (in blue) represents PQLC2, with the curved line (in orange) embedded in the central cavity indicating the WDR41-7CD loop. The spin label is shown as a red star.

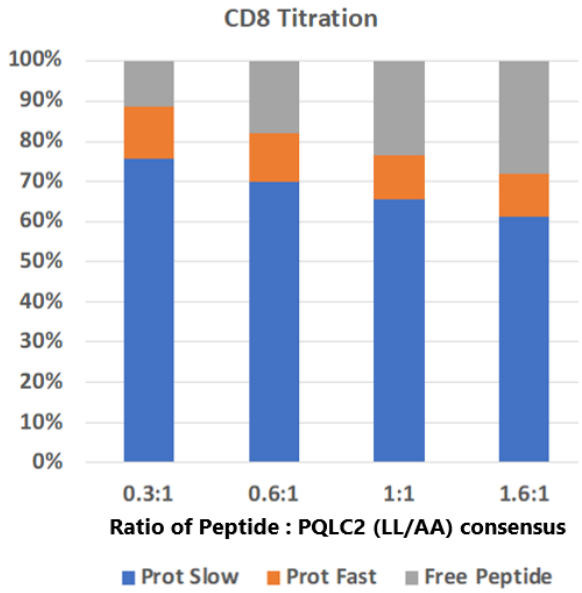

Figure 69. Stimulation was performed using the three components: slow, fast, and free. The molar ratios of CD8 WDR41-7CD loop peptide to PQLC2 (LL/AA) consensus are indicated at the bottom of each bar plot. The blue color represents the slow component, the orange represents the fast component, and the gray represents the free peptide.

4.7.6 L-Arginine displaces the binding of PQLC2 (LL/AA) consensus/WDR41-7CD loop

As discussed earlier, the recruitment of the CSW complex by PQLC2 occurs when cells are deprived of cationic amino acids, such as L-Arg, which are the substrates of PQLC2 (see **introduction, Figure 17**) (Amick et al., 2020) (Amick et al., 2018). However, this interaction is reversible, as reintroducing L-Arg into the cell culture media leads to the release of the CSW complex from the lysosomal membrane (Leray et al., 2021). Therefore, the presence of L-Arg seems to be displacing WDR41-7CD loop/PQLC2 interaction. AlphaFold V2.0 predictions and docking studies show that the PQLC2 binding sites of L-Arg and WDR41-7CD loop are overlapping within the central cavity of PQLC2, suggesting that both L-Arg and WDR41-7CD loop are competing for the same binding site. We tested the effect of the substrate (L-Arg) on PQLC2 (LL/AA) consensus/ WDR41-7CD loop binding using EPR spectroscopy. Remarkably, the presence of L-Arg suppresses almost completely the slow component of the nitroxide EPR spectra (**Figure 70**). The nitroxide EPR spectra of WDR41-7CD loop/ PQLC2 (LL/AA) consensus in the presence of L-Arg resembles the one of the free WDR41-7CD loop (**Figure 70**), indicating that L-Arg is able to disrupt WDR41-7CD loop-PQLC2 interaction. Although predicting models and docking studies suggest that L-Arg might displace WDR41-7CD loop-PQLC2 interaction by competing for the same binding site, other mechanisms could be also taking into account like for instance a possible L-Arg-induced PQLC2 conformational change that could release the WDR41-7CD loop from its binding site (**Figure 46**).

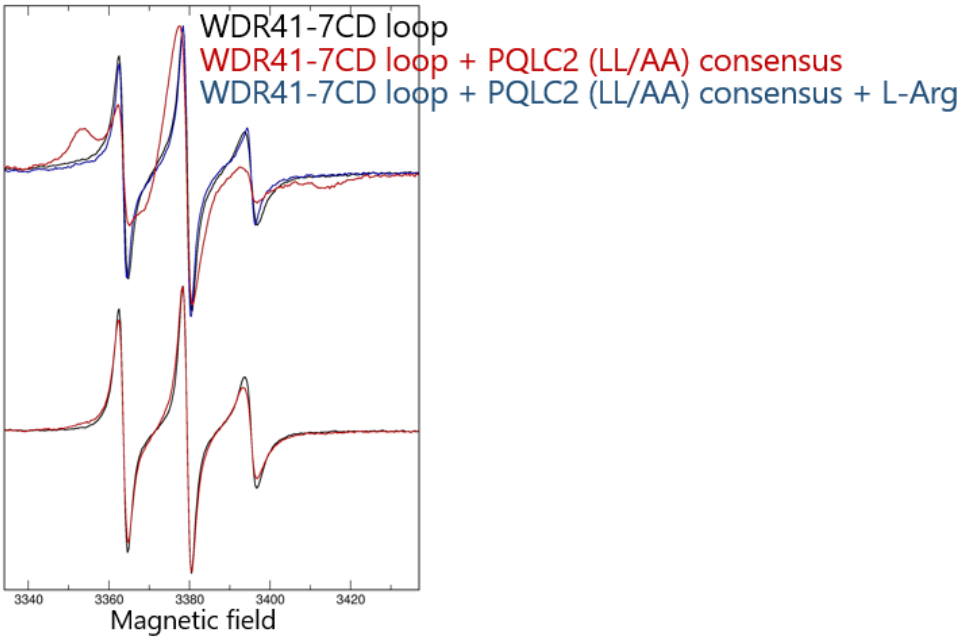

Figure 70. EPR spectra of PQLC2 (LL/AA) consensus/ WDR41-7CD loop in presence of L-Arg. The CD8 (upper spectra) and the WDR41-7CD loop mutant (CD6 – P8C, F13A, W17A, V20C) (lower spectra). The black line represents the spectrum of CD8 alone (31 μM), the red line represents the spectrum after adding purified PQLC2 (LL/AA) consensus (35 μM); the blue line represents the spectrum after adding 100 mM L-Arg.

In conclusion, we experimentally validated the specific interaction between the WDR41-7CD loop and purified PQLC2 (LL/AA) consensus. Our data also provided further insights into this interaction, suggesting that the WDR41-7CD loop adopts different poses within the central cavity of PQLC2 (LL/AA) consensus. Additionally, we obtained further evidence for the reversibility of this interaction, showing that the addition of L-Arg reduces or inhibits the binding of the WDR41-7CD loop to PQLC2 (LL/AA) consensus.

5 DISCUSSION

Living organisms must constantly adapt to changes in their environment, and this adaptation relies on cells' ability to sense and transduce a wide variety of signals- ranging from nutrients and energy levels to chemical messengers and waste products (Wengrod & Gardner, 2015) (Wellen & Thompson, 2010). These signals are detected by receptors located on the cell surface and within the cell, enabling coordinated cellular responses to environmental changes (Shpakov, 2023) (Belfiore et al., 2017) (Ho et al., 2017).

In this project, we have investigated a novel class of receptors involved in nutrient sens- ing and cell signalling, that do not fit into traditional categories. These receptors are integral membrane proteins that exhibit both transporter and receptor functions, and are referred as transceptors (Diallinas, 2017) (Rubio-Texeira et al., 2010) (Scalise et al., 2019) (Ozcan, 1998). A transceptor is a transporter that has evolved to interact with signaling proteins in a substrate-dependent manner, enabling it to not only transport molecules across the membrane but also to transduce extracellular and intracellular signals through these interactions (**Figure 71**) (Thevelein & Voordeckers, 2009) (Hundal & Taylor, 2009) (Forsberg & Ljungdahl, 2001).

In particular, this thesis focuses on PQLC2, a mammalian amino acid transceptor located in the lysosomal membrane. PQLC2 has two key roles: (*i*) it exports proteolysis- derived cationic amino acids from the lysosomal lumen to the cytosol (Jain & Zoncu, 2021), and (*ii*) it functions as an amino acid-gated receptor, interacting with a cytosolic protein complex (C9ORF72/SMCR8/WDR41 or CSW complex). Although the cellular response resulting from the lysosomal recruitment of the CSW complex is not yet fully understood, several studies support the idea that this recruitment is involved in a novel lysosomal-mediated signalling process. The lysosomal localization of the CSW complex is crucial for normal lysosomal function and may play a role in the regulation of mTORC1 (Sullivan et al., 2016) (Corrionero & Horvitz, 2018). *In vitro* studies have

demonstrated GTPase-activating protein (or GAP) for C9ORF72 and SMCR8, specifically targeting small GTPases (Corbier & Sellier, 2017) (Tang et al., 2020). Interestingly, congenital mutations in the gene encoding C9ORF72 are directly implicated in two neurodegenerative diseases (Jézégou et al., 2012) (Amick et al., 2020) (Corrionero & Horvitz, 2018).

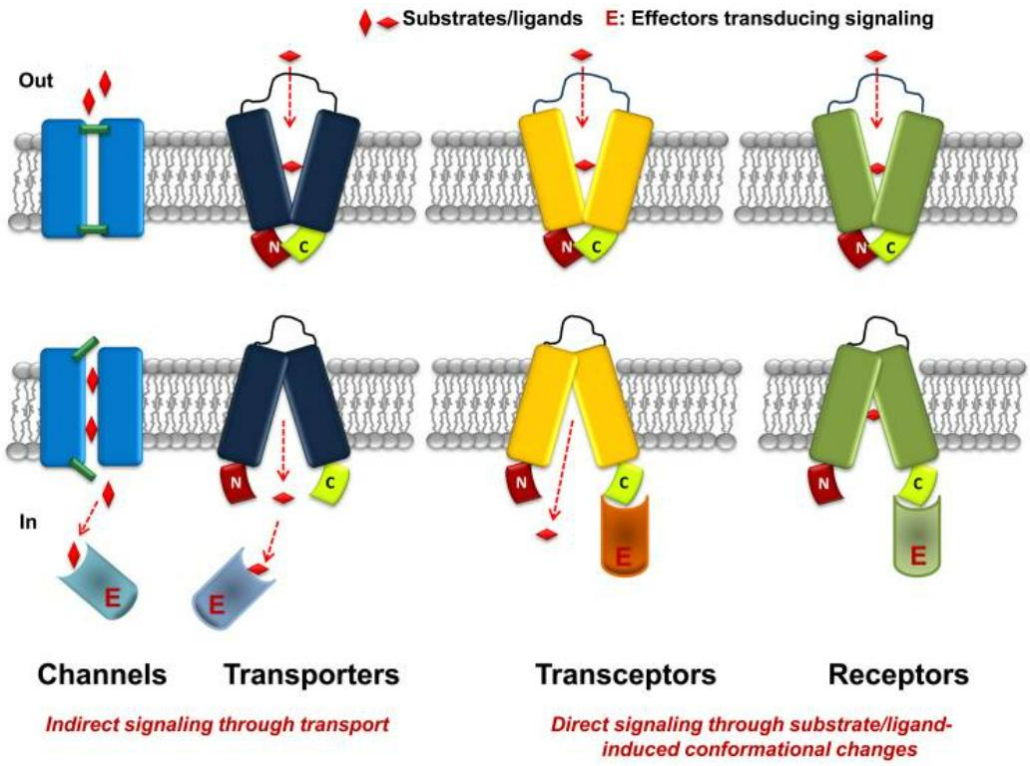

Figure 71. A scheme comparing transporters, channels, transceptors, and receptors illustrates their functional differences. Ion channels are regulated by the simultaneous opening and closing of gates (Drew & Boudker, 2016). In contrast, transporters, transceptors, and receptors undergo conformational changes, alternating between outward- and inward-facing states in response to ligand binding. The C-terminal domain of both receptors and transceptors is involved in recognizing and binding downstream effector proteins (E) when in the inward-facing conformation, thereby transducing the signal (Diallinas, 2017) (Hundal & Taylor, 2009) (Forrest et al., 2011). Adapted from (Diallinas, 2017).

Evidences of the tranceptor role of PQLC2 came recently from studies using

mammalian cell cultures demonstrated the recruitment of the CSW complex to lysosomes during amino acid starvation. Later, Fergunson and colleagues identified PQLC2 as the only known receptor of the CSW complex at the lysosomal membrane (Jézégou et al., 2012) (Amick et al., 2020) (Talaia et al., 2021). Under nutrient-rich conditions, PQLC2 transports cationic amino acids from the lysosomal lumen to the cytosol. However, during amino acid starvation, PQLC2 recruits the CSW complex to the lysosomal membrane (Amick et al., 2020) (Amick et al., 2016). Interestingly, this process is reversible since replenishment of cationic amino acids in the cell culture media releases the CSW complex from the lysosomal membrane, strongly indicating that CSW complex recruitment is cationic amino acid-dependent. This findings assigns to PQLC2 a role in amino acid sensing, which controls CSW recruitment (Leray et al., 2021). The localization of the CSW complex to the lysosome relies only in the interaction between WDR41 and PQLC2 (Talaia et al., 2021) (Amick et al., 2020). Moreover, Talaia et al., 2021 characterized the molecular basis governing PQLC2/WDR41 recognition. Using homology modeling and protein-protein docking simulations, they identified a flexible loop protruding from WDR41's blade 7 ('WDR41-7CD) as a critical region for this interaction. Immunoprecipitation and pulldown assays with mutant WDR41 constructs confirmed that a 10-amino acid motif, TIP (Transporter-Interacting Peptide: TGFFNMWGFG), within the WDR41-7CD loop is both necessary and sufficient for PQLC2 binding.

As mentioned earlier, the interaction between PQLC2 and the CSW complex, as well as the transport activity of PQLC2, has been studied in living cells and cell homogenates (Leray et al., 2021) (Amick et al., 2020) (Talaia et al., 2021) (Jézégou et al., 2012). However, in these studies, the involvement of other interacting proteins could not be ruled out. Therefore, to better understand the role of PQLC2 in amino acid sensing and cells signaling, in this thesis we aimed at characterizing the molecular mechanisms underlying the interaction between PQLC2 and WDR41 using purified proteins.

The first goal was to develop a robust protocol to obtain purified (stable) PQLC2 in

detergent micelles, enabling us to use various techniques to assess its structure and function *in vitro*. In fact, one of the main challenges in studying membrane proteins, especially for structural and functional characterization, is their production and purification (Junge et al., 2008). Unlike soluble proteins, membrane proteins are embedded in lipid bilayers, which makes them difficult to express, fold, and stabilize in an aqueous environment (Duquesne et al., 2016) (Lin & Guidotti, 2009). Often, for they study they must be extracted from their native lipid environment by detergents (Seddon et al., 2004) (Alberts B., et al., 2002). The process of selecting an appropriate detergent to effectively solubilize the protein in its functional state is often tedious (Banerjee et al., 1995) (Anandan & Vrielink, 2016) (Lenoir et al., 2018). We decided to clone and express PQLC2 in the yeast *S. cerevisiae*, a well-established and cost-effective system for the recombinant expression of eukaryotic membrane proteins. This system offers several advantages, including high expression yield and ease of handling (Carlesso et al., 2022) (King & Kunji, 2020) (Parker & Newstead, 2014). Moreover, our laboratory's extensive experience with membrane protein expression in *S. cerevisiae* provided a significant advantage in the successful expression and purification of PQLC2 (Lamy et al., 2021) (Lenoir et al., 2002). We chose to work with the rat ortholog of PQLC2 based on previous work that showed that yeast-expressed rat PQLC2 is functional since it was found to complement the growth phenotype of the yeast PQLC2 homolog, YPQ2 (Jézégou et al., 2012).

One key feature of PQLC2 is the dileucine motif at positions 290/291 on its C-terminal region, which it is crucial for its lysosomal sorting. This motif likely participates in a clathrin-dependent pathway that targets the transporter to the lysosome (Jézégou et al., 2012) (Braulke & Bonifacino, 2009). Previous studies in *Xenopus* oocytes showed that mutations of these residues to alanine (we refer this mutation as LL/AA) redirect the GFP-tagged PQLC2 from the lysosomal membrane to the plasma membrane (Jézégou et al., 2012). This mutation is a well-established strategy for redirecting lysosomal membrane transporters to the cytoplasmic membrane, providing a more

accessible environment for functional studies, as opposed to the complex lysosomal compartment (Kalatzis, 2001) (Jézégou et al., 2012) (Morin et al., 2004). We performed confocal fluorescence microscopy of yeast cells expressing a C-terminal GFP-tagged rat PQLC2 and found that PQLC2 produced in yeast was localized in the membrane of enclosed vacuole-like organelles (**Figures 33 and 50**). This is in agreement of a previous work (Jézégou et al., 2012). Interestingly, our results revealed that, irrespective of the presence or absence of the dileucine-based sorting motif, PQLC2 was always localized in the same vacuole-like membrane compartment (**Figure 33**). Interestingly, this result does not align with the findings of Llinares et al, who show that mutation of the dileucine motif in PQLC2 impairs its vacuolar sorting in yeast, most likely because the protein is no longer regonized by the alkaline phosphatase (ALP) trafficking pathway, which requires the AP-3 adaptor complex (Llinares et al., 2015). Given the importance of efficient purification for subsequent functional and structural studies, we employed a well-established protocol from our laboratory for affinity purification, utilizing the complex GFP/nanoGFP for the purification of membrane proteins (Lamy et al., 2021). This system capitalizes on the high-affinity interaction between nanoGFP and the GFP tag, allowing for efficient and specific purification of PQLC2 from *S. cerevisiae* membranes (Lamy et al., 2021) (Rothbauer et al., 2008) (Z. Zhang et al., 2020) (Whicher & MacKinnon, 2016) (Jojoa-Cruz et al., 2018).

To assess the best detergent for solubilizing PQLC2 we tested several detergents and found that DDM exhibited the most efficient solubilization, producing the highest protein yield and ensuring better homogeneity of the solubilized protein compared to the other detergents tested (**Figures 35 and 47**). Based on these results, we selected DDM as the detergent for both wild-type and LL/AA versions of PQLC2, and proceeded with purification using affinity chromatography. DDM-solubilized PQLC2-GFP (wild-type and LL/AA) was immobilized in agarose beads coupled to nanoGFP, and the protein was eluted by proteolytic cleavage of the linker between PQLC2 and GFP (**Figures 38, 40, 42 and 52**). SDS-PAGE, Western Blot and mass spectrometry analysis (**Figures 38, 40, 42 and 52**) confirmed the identity of our purified PQLC2 as well as the

purity of the sample. Thus, we successfully expressed and purified for the first time a mammalian PQLC2 using *S. cerevisiae* as a heterologous host. Unfortunately, both versions of purified PQLC2 (wild-type and LL/AA) showed poor stability in detergent as judged by SEC analysis (**Figure 39**). As wild-type PQLC2 began to precipite during concentration, we decided to focus our efforts on stabilizing the LL/AA version of PQLC2. As discussed earlier, in *Xenopus* oocytes the double LL/AA mutation does not impair the functional activity of PQLC2 (Jézégou et al., 2012). To enhance protein stability after purification, we decided to use protein-engineering tools (Rodríguez-Banqueri et al., 2016) (Rawlings, 2018). Based on our AlphaFold V2.0 model, the N-terminal region of PQLC2 (LL/AA) is highly charged and predicted to be disordered. This observation led us to hypothesize that removing this region could enhance the protein's stability, following a strategy similar to that employed by Lei et al. (2018) to obtain the crystal structure of the lysosomal amino acid transporter SLC38A9. To test this hypothesis, we generated two mutants, Δ11 and Δ29, by deleting the first 11 and 29 amino acids of the PQLC2 N-terminus, respectively (**Figure 41, upper panel**). However, contrary to our expectations, both mutants displayed reduced stability, with Δ29 showing the most pronounced instability (**Figure 41 and 42**). Nevertheless, these experiments highlighted the important role of the N-terminal region of PQLC2 (particularly residues 11 to 29) for maintaining the protein's stability when solubilized in detergent micelles. While the LL/AA sorting motif in the C-terminal region of PQLC2 directs the protein to the lysosomal membrane, the N-terminal region may also play a role on trafficking and folding in PQLC2, as is the case for other membrane transport proteins (Szczesna-Skorupa et al., 1995) (Okamoto et al., 2020) (Jézégou et al., 2012).

We then desided to use a completely different protein engineering approach to enhance PQLC2 stability in detergent micelles: the design of a consensus-based sequence. Several studies have employed this strategy with success to enhance the structural stability of membrane transporters (Cirri et al., 2018) (Cirri et al., 2018) (Canul-Tec et al., 2017) (Niggemann & Steipe, 2000) (Ohage et al., 1999) (Steipe, 2004) (Oda et al., 2020). This approach generates a sequence based on the most frequent amino

acid at each position, derived from the alignment of homologous protein sequences across multiple species (**Figure 43**) (see **results** for the criteria used) (Cirri et al., 2018). Based on this criteria, we generated a PQLC2 (LL/AA) consensus sequence by introducing a total of 19 mutations into the original PQLC2 sequence, achieving 93% sequence identity with the original PQLC2 (LL/AA) sequence (**Figures 44 and 45**).

To ensure that the key structural features were preserved in the PQLC2 (LL/AA) consensus sequence, we used AlphaFold and docking models to verify that the predicted arginine-binding sites, along with the aromatic amino acids potentially interacting with WDR41, were maintained (Talaia et al., 2021) (**Figure 46**). Furthermore, the functionality of the PQLC2 (LL/AA) consensus sequence was validated through transport assays in *Xenopus* oocytes, using both electrophysiological recordings and measurements of radioactive L-Arg accumulation. These experiments demonstrated robust arginine transport, which is consistent with previous studies on the PQLC2 (LL/AA) (experiments conducted by our by our collaborators Dr Bruno Gasnier and Dr Cécile Jouffret (U. Paris-Cité, Paris) (Jézégou et al., 2012).

PQLC2 consensus-GFP expresses approximately 1.7 times more than the PQLC2 (LL/AA) (**Figure 51**). Moreover, thermal stability assays of the purified proteins demonstrated that the PQLC2 (LL/AA) consensus exhibited enhanced thermal stability compared to the original PQLC2 (LL/AA) (**Figures 48 and 49**) (Cirri et al., 2018) (Oda et al., 2020). This increased heat tolerance suggests that the PQLC2 (LL/AA) consensus is more stable, with improved solubility and minimal aggregation. Indeed, that was the case, unlike PQLC2 (LL/AA), purified PQLC2 (LL/AA) consensus was able to be concentrated up to ~ 3-4 mg/mL in DDM, and SEC analysis yielded a fairly homogeneus elution profile (**Figure 52**), highlighting that the consensus sequence improves both protein yield and stability, which are necessary for further structural and functional characterization. In conclusion, we successfully expressed and purified the PQLC2 (LL/AA) consensus, which demonstrated greater stability than the PQLC2 (LL/AA), making it suitable for subsequent studies.The success of the consensus-based

mutagenesis approach is primarily based on experimental observations, which suggest that more frequently occurring amino acids at a given position in an amino acid sequence alignment have a greater stabilizing effect than less frequently occurring amino acids.

The success of the consensus-based mutagenesis approach relies on experimental observations, which suggest that amino acids that occur more frequently at a given position in a sequence have a stronger stabilizing effect than those that occur less frequently (Lehmann et al., 2000). For instance, studies on antibody stability have shown that consensus mutagenesis results in a significantly higher success rate (~60%) compared to random mutagenesis (Steipe et al., 1994). This approach has enabled the engineering of hyperstable immunoglobulin domains, which can be expressed as intrabodies (Ohage et al., 1999). Another recent example specifically applied to membrane transport proteins was the amino acid antiporter XCT, a transporter that mediates the import of L-cystine and the export of L-glutamate across the plasma membrane (Oda et al., 2020). This approach successfully improved the stability of the transporter, enabling its purification and subsequent cryo-EM analysis.

Next, we investigated the oligomerization state of PQLC2 in detergent micelles. Size exclusion chromatography of detergent-solubilized PQLC2(LL/AA) initially suggested that PQLC2 assembles into homotrimers (**Figure 39**). This trimeric arrangement was further confirmed by NS-EM of PQLC2 (LL/AA) consensus purified in DDM and exchanged to LMNG in the SEC column (**Figures 53 and 54**). The NS-EM micrographs revealed particles with an average diameter of approximately 8 nm, consistent with a homotrimeric model of PQLC2 (LL/AA) consensus predicted by AlphaFold (**Figure 54**). The pLDDT or confident score of our model ranges between 80 and 90 in most of the residues of the PQLC2 predicted trimer with the exception of TM 4 and the loop connecting TMs 4 and 5 (**Figure 54**). Interestingly, a similar homotrimeric organization has been observed in two other members of the PQ-loop family: the SWEET sugar transporter, (Tao et al., 2015) (Han et al., 2017), and the vitamin B3 transporter PnuC

(Jaehme et al., 2014). Interestingly, as for the PQLC2 closed homolog cystinosin, the Alphafold V2.0 model of PQLC2 aligns very well with the crystal structure of the plant sugar transporter SWEET (Tao et al., 2015) (**Figures 12 and 72**). The molecular architecture of PQ-loop transporters consists of two bundles of 3 TMs (TMs 1-2-3, and TMs 5-6-7) symmetrically related by a pseudo–two-fold axis, and connected by TM 4 (Tao et al., 2015) (Jaehme et al., 2014) (Guo et al., 2022) (Löbel et al., 2022) (Gerondopoulos et al., 2021) (**Figure 72**). The PQ motifs located in TMs 1 and 5 are thought to play critical roles in the conformational transitions made by the transporter during substrate transport (**Figure 6**) (Guo et al., 2022).

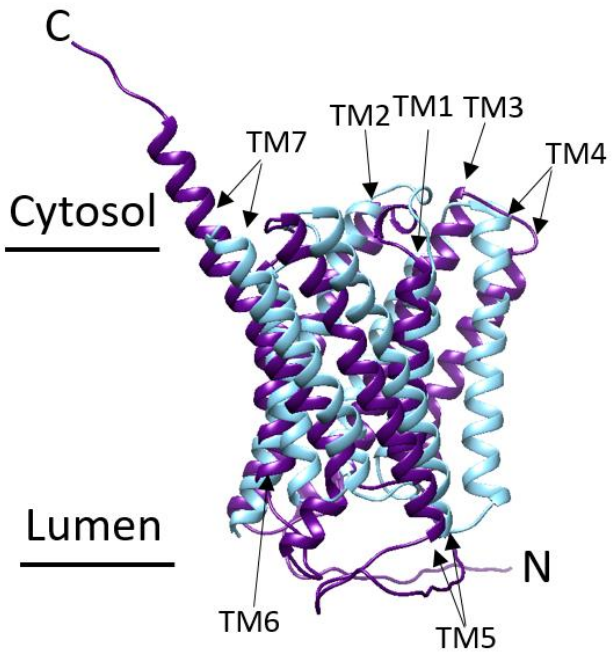

Figure 72. Overlay of the PQLC2 (LL/AA) AlphaFold V2.0 model (purple) with the 3D structure of the eukaryotic SWEET transporter (as monomer in blue). PDB ID of eukaryotic SWEET transporter : 5CTH (Tao et al., 2015).

In conclusion, the use of PQLC2 (LL/AA) consensus has enabled us to obtain for the first time structural information of PQLC2. NE-EM studies of detergent purified PQLC2 (LL/AA) consensus suggest that this transporter oligomerizes, probably as a trimer.

The second aim of this project was to investigate the functional properties of purified PQLC2 (LL/AA or consensus) after reconstituting into liposomes (**Figure 30**). Although PQLC2 (LL/AA or consensus) was efficiently reconstituted into liposomes where non-agregated protein reconstituted into the lipid bilayer was detected (**Figure 55**), transport assays in proteoliposomes showed limited accumulation of [^{3}H]L-Arg or [^{3}H]L-Lys (**Figure 56**). In addition, these results were poorly reproducible. One possible explanation of our results is the apparent low affinity of PQLC2 for either L-Arg or L-Lys, which is a limitation in transport assays when using radiolabeled ligands. In fact, experiments conducted in *Xenopus* oocytes, revealed a Michaelis–Menten kinetics constant (K_m) of 3.8 mM for L-Arg transport by PQLC2 (LL/AA) (Jézégou et al., 2012). Functional reconstitution of membrane transport protein into artificial lipid bilayers is always very challenging, as many proteins are inactivated during detergent extraction, and subsequent liposome reconstitution. Nevertheless, our results, though not entirely satisfactory, indicate that the PQLC2 (LL/AA) consensus reconstituted into liposomes displays some activity, which offers optimism for future work. In the future directions of this project, we aim at exploring alternative approaches to characterize the transport activity of PQLC2 (LL/AA) consensus reconstituted into liposomes like the use of methods based on fluorescence spectroscopy or measuring the activity of PQLC2 directly in isolated yeast vacuoles (Cools et al., 2020) (see **conclusions and perspectives**).The third objective of this project was to investigate the interaction between purified PQLC2 (LL/AA) consensus and WDR41 *in vitro* using purified proteins. To this end, we employed EPR spectroscopy, a powerful technique for probing molecular interactions and dynamics in solution (Sahu & Lorigan, 2020) (Klug & Feix, 2008). Unfortunately, initial attemps in our team to express WDR41 in yeast were unsuccessful (results not shown). We then decided to use a synthetic peptide encoding WDR41-7CD since immunoprecipitation and pull-down assays identified a 10 amino acid motif (TIP: TGFFNMWGFG) (**Figure 14**) within the WDR41-7CD loop of WDR41 as the necessary and sufficient motif for the recruitment by PQLC2 of the CSW complex to the lysosomal membrane (Talaia et al., 2021). We introduced cysteine residues at

various positions in the chemically synthesized WDR41-7CD loop peptides (**Table 6**), and a proxyl nitroxide spin label was attached to these peptides using a well-established maleimide-cysteine linker chemistry. EPR spectra confirmed that the nitroxides were successfully bound to the WDR41-7CD loop via the introduced cysteines (**Figure 61**). Our EPR data showed that the chemically synthesized WDR41-7CD loop interacts with purified PQLC2 (LL/AA) consensus, in agreement with the pull-down experiments done in cell extracts by Ferguson and colleagues (Talaia et al., 2021) (**Figure 62**). Moreover, EPR measurements using mutated versions of WDR41-7CD loop confirmed the essential role of two aromatic residues within the TIP region of WDR41-7CD loop for PQLC2/ WDR41-7CD loop interaction (**Figure 62**). It is important to note that these experiments were made possible thanks to the use of the consensus-based approach, which enhanced the stability of PQLC2 after purification and concentration. This was crucial, as EPR experiments require relatively high protein concentrations.

Modifying the spin label position along the WDR41-7CD loop provided insights into the molecular mechanism of WDR41-7CD loop/PQLC2 interaction (**Figure 63**). Positions within the WDR41-7CD loop flancking the TIP region appear to be more mobile or exposed to the solvent, whereas positions closer to the TIP display less mobility, according the EPR spectrum (**Figure 63**). Interestingly, these results agree with the proposed binding model of Ferguson and colleagues (Talaia et al., 2021) (**Figure 73**) and with our Alphafold V2.0 model where the TIP region is predicted to sit deeper inside the PQLC2 central cavity (**Figures 13 and 15**). Interestingly, the deconvolution of the EPR spectrum of the nitroxside-labeled WDR41-7CD loop in the presence of PQLC2 (LL/AA) consensus reveal three different correlation times. The fast associated with the spin-labeled WDR41-7CD loop not bound to PQLC2; and two slower components that might reflect two different conformational states of the WDR41-7CD loop after binding to PQLC2 in detergent micelles. It is well establish that membrane transporters exhibit considerable conformational flexibility in detergent micelles; thus,these

two components could represent an equilibrium of PQLC2 between different conformers after binding to the WDR41-7CD loop. In any case, further studies investigating the WDR41-7CD loop-induced conformational changes in PQLC2 will be necessary to fully understand our EPR data. Overall, EPR experiments confirmed the findings of Talaia et al. (2021) in cell extracts, demonstrating a direct interaction between purified PQLC2 (LL/AA) consensus and WDR41-7CD loop, including the key role of two aromatic residues in the TIP region of the WDR41-7CD loop to stablish this interaction (**Figures 62 and 73**).

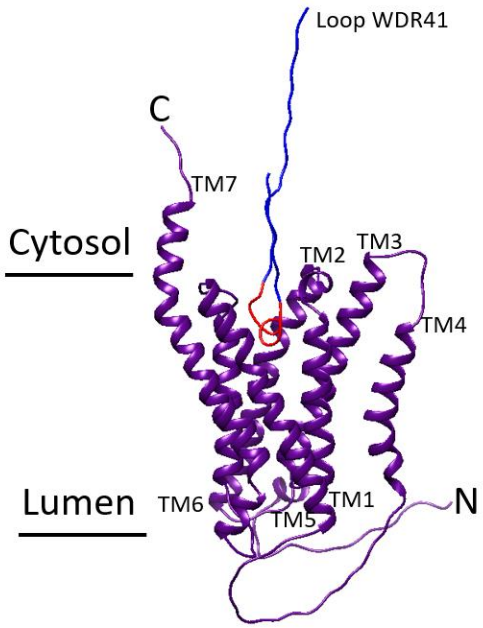

Figure 73. Representation of the interaction betwee WDR41-7CD loop and PQLC2 (LL/AA) consensus. AlphaFold model of PQLC2 (in purple) docked to the WDR41-7CD loop (in blue). The TIP region (in red) is inserted into the central cavity of PQLC2 (LL/AA) consensus.

Finally, EPR experiments also revealed the inhibitory effect of the PQLC2 substrate L-Arg on PQLC2/ WDR41-7CD loop interaction (**Figure 70**). Furthermore, the recruitment of the CSW complex by PQLC2 to the lysosomal membrane is completely reversed

when L-Arg and other cationic amino acids are reintroduced to the culture medium (Leray et al., 2021). Our results using purified protein in detergent micelles provide a direct proof that L-Arg directly inhibits PQLC2/WDR41-7CD loop interaction, a possible molecular explanation of how the presence of PQLC2 substrates induce the dissociation the PQLC2/WDR41 interaction at the lysosomal membrane. As 3D models predict that both L-Arg and WDR41-7CD loop share a similar binding pocket in PQLC2 (**Figure 46**), we can speculate that L-Arg inhibits PQLC2/ WDR41-7CD loop interaction by a simple competition mechanism. However, other mechanisms are also possible. For instance, binding of L-Arg to PQLC2 may induce a conformational change in PQLC2 that could disrupt its interaction with WDR41, highlighting the dynamic nature of this protein-protein interaction.

6 CONCLUSIONS AND PERSPECTIVES

According to the available literature, this thesis reports the first biochemical attempts to study PQLC2. Several key objectives were accomplished in this project:

(i) We successfully established a robust protocol for the purification of PQLC2, employing a well-established affinity purification strategy from our laboratory that utilizes the complex GFP/nanoGFP, specifically designed for efficient isolation of membrane proteins (Lamy et al., 2021) (Zhang et al., 2020) (Rothbauer et al., 2008). The success of this protocol ensures that we can obtain purified PQLC2 in sufficient quantities for downstream structural and functional studies, providing a strong foundation for future investigations into the properties and mechanisms of this transporter.

(ii) We generated a stable form of purified PQLC2 through a consensus-based mutagenesis approach, which not only enhanced the protein's stability but also allowed us to gain the first insights into the oligomerization state of PQLC2.

(iii) We established a successful protocol for the reconstitution of PQLC2 into liposomes for transport experiments using radioactive substrates. Nevertheless, our results, though not entirely satisfactory, indicate that the PQLC2 (LL/AA) consensus reconstituted into liposomes displays some activity, which offers optimism for future work.

(iv) Finally, we used both conventional EPR techniques and innovative approaches combining spin labeling and high magnetic fields developed in the laboratory of Leandro Tabares and Sun Un (I2BC) to study the *in vitro* interaction between the purified PQLC2 (LL/AA) consensus and the synthetic WDR41-7CD loop peptide.

In conclusion, previous studies on the CSW complex and its interactions with small GTPases have not included purified PQLC2, and molecular characterization of lysosomal transceptors remains limited. This is where the novelty of our project lies.

Future Directions:

In this project, several avenues for further exploration and refinement of PQLC2's structural and functional properties are already outlined. Building on our current findings, the following steps will be essential in deepening our understanding of this transporter:

1. Site-directed mutagenesis and functional analysis:
   to investigate the role of conserved aromatic residues within PQLC2's central cavity, site-directed mutagenesis will be performed. Specifically, we will target F49, W78, Y105, and Y195, which were previously identified in cell extracts (Talaia et al., 2021). These residues are hypothesized to play a critical role in the interaction between PQLC2 and the WDR41-7CD loop. By mutating these residues, we aim to elucidate their contribution to the protein's interaction dynamics and transport function.

2. Structural insights through cryo-EM:
   further structural studies will focus on resolving the 3D structure of PQLC2 using cryo-EM. Recent collaborative efforts with our colleagues in Spain have already yielded promising results, including 2D particle classifications that suggest the presence of PQLC2 dimers. These early results set the foundation for high-resolution cryo-EM data, which will provide deeper insights into the architectural organization of PQLC2. This structural data will be critical in understanding the conformational flexibility of the transporter.

3. EPR for conformational studies:
   To complement the cryo-EM data, high-field/high-frequency EPR techniques

will be employed to investigate the internal magnetic properties of paramagnetic centers in PQLC2. These EPR experiments will help measure long-range distances between magnetic centers, providing valuable information about the spatial arrangement and conformational changes within the protein. Together with cryo-EM, these structural techniques will offer complementary perspectives on the transporter's architecture and function.

4. Exploring the PQLC2/WDR41 interaction:
the interaction between PQLC2 and full-length WDR41 will be another key focus. Currently, the full-length WDR41 protein is being expressed in insect cells by Philémon Von Gaudecker, with purification assays underway. We will optimize experimental conditions for the PQLC2/WDR41 interaction, testing variables such as pH, the presence of PQLC2 substrates, and using PQLC2 mutants that do not associate with the CSW complex as negative controls (Talaia et al., 2021). This will help us define the key factors governing their interaction and the implications for the function of both proteins.

5. Transport studies using vacuoles from *S. cerevisiae*:
for transport assays, we will utilize purified vacuoles from *S. cerevisiae* expressing PQLC2, as an alternative to proteoliposomes. Previous studies by Bruno André's lab (Université Libre de Bruxelles, Belgium) have shown that PQLC2 expressed in S. cerevisiae is correctly targeted to the vacuolar membrane via the ALP pathway, where it retains transport activity after vacuole purification (Cools et al., 2020; Llinares et al., 2015). This system will allow for more reliable transport assays and facilitate the study of PQLC2's substrate interactions and transport mechanisms.

6. Fluorescence-based monitoring of PQLC2/WDR41 interaction: the dynamic interaction between PQLC2 and WDR41, both in peptide and full-length forms, will be monitored in membrane systems using fluorescence spectroscopy techniques, such as fluorescence anisotropy and Förster resonance energy transfer (FRET). In these experiments, the GFP tag fused to PQLC2 will serve as the donor fluorophore, while a Cy3 dye attached to WDR41 will act as the acceptor. This approach will allow for real-time monitoring of the interaction dynamics, shedding light on the affinity and nature of the PQLC2/WDR41 interaction in a membrane-like environment.

7. Stabilizing PQLC2 for structural and functional studies: to ensure the stability of PQLC2 for the above experiments, we will use membrane mimetic systems such as detergents, nanodiscs, and peptidiscs. These systems are particularly advantageous for preserving the native-like environment of membrane proteins. Nanodiscs and peptidiscs, in particular, offer enhanced stability over traditional detergents, ensuring that PQLC2 retains its functional properties when interacting with cationic amino acid substrates and WDR41. These mimetics will provide a more accurate representation of PQLC2's behavior in solution, allowing for better insight into its structure and function in the presence of substrates and interacting partners.

7 REFERENCES

Abu-Remaileh, M., Wyant, G. A., Kim, C., Laqtom, N. N., Abbasi, M., Chan, S. H., Freinkman, E., & Sabatini, D. M. (2017). Lysosomal metabolomics reveals V-ATPase- and mTOR-dependent regulation of amino acid efflux from lysosomes. *Science*, *358*(6364), 807-813. https://doi.org/10.1126/science.aan6298

Alberts B., Johnson A., & Lewis J.,. (2002). Membrane Proteins. *Molecular Biology of the Cell. . New York: Garland Science*, *4th edition*.

Amick, J., Roczniak-Ferguson, A., & Ferguson, S. M. (2016). C9orf72 binds SMCR8, localizes to lysosomes, and regulates mTORC1 signaling. *Molecular Biology of the Cell*, *27*(20), 3040-3051. https://doi.org/10.1091/mbc.e16-01-0003

Amick, J., Tharkeshwar, A. K., Amaya, C., & Ferguson, S. M. (2018). WDR41 supports lysosomal response to changes in amino acid availability. *Molecular Biology of the Cell*, *29*(18), 2213-2227. https://doi.org/10.1091/mbc.E17-12-0703

Amick, J., Tharkeshwar, A. K., Talaia, G., & Ferguson, S. M. (2020). PQLC2 recruits the C9orf72 complex to lysosomes in response to cationic amino acid starvation. *Journal of Cell Biology*, *219*(1), e201906076. https://doi.org/10.1083/jcb.201906076

Anaïs Lamy. Lipid Flippases from Plasmodium Parasites : From Heterologous Production towards Functional Characterization. Biochemistry, Molecular Biology. Université Paris-Saclay, 2018. English. ⟨NNT : 2018SACLS447⟩. ⟨tel-02426208⟩. (s. d.).

Anandan, A., & Vrielink, A. (2016). Detergents in Membrane Protein Purification and Crystallisation. In I. Moraes (Éd.), *The Next Generation in Membrane Protein Structure Determination* (Vol. 922, p. 13-28). Springer International Publishing. https://doi.org/10.1007/978-3-319-35072-1_2

Anandapadamanaban, M., Masson, G. R., Perisic, O., Berndt, A., Kaufman, J., Johnson, C. M., Santhanam, B., Rogala, K. B., Sabatini, D. M., & Williams, R. L. (2019). Architecture of human Rag

GTPase heterodimers and their complex with mTORC1. *Science*, *366*(6462), 203-210. https://doi.org/10.1126/science.aax3939

Anikster, Y., Shotelersuk, V., & Gahl, W. A. (1999). CTNS mutations in patients with cystinosis. *Human Mutation*, *14*(6), 454-458. https://doi.org/10.1002/(SICI)1098-1004(199912)14:6<454::AID-HUMU2>3.0.CO;2-H

Aylett, C. H. S., Sauer, E., Imseng, S., Boehringer, D., Hall, M. N., Ban, N., & Maier, T. (2016). Architecture of human mTOR complex 1. *Science*, *351*(6268), 48-52. https://doi.org/10.1126/science.aaa3870

Azouaoui, H., Montigny, C., Ash, M.-R., Fijalkowski, F., Jacquot, A., Grønberg, C., López-Marqués, R. L., Palmgren, M. G., Garrigos, M., Le Maire, M., Decottignies, P., Gourdon, P., Nissen, P., Champeil, P., & Lenoir, G. (2014). A High-Yield Co-Expression System for the Purification of an Intact Drs2p-Cdc50p Lipid Flippase Complex, Critically Dependent on and Stabilized by Phosphatidylinositol-4-Phosphate. *PLoS ONE*, *9*(11), e112176. https://doi.org/10.1371/journal.pone.0112176

Azouaoui, H., Montigny, C., Jacquot, A., Barry, R., Champeil, P., & Lenoir, G. (2016). Coordinated Overexpression in Yeast of a P4-ATPase and Its Associated Cdc50 Subunit : The Case of the Drs2p/Cdc50p Lipid Flippase Complex. In M. Bublitz (Éd.), *P-Type ATPases* (Vol. 1377, p. 37-55). Springer New York. https://doi.org/10.1007/978-1-4939-3179-8_6

Baba, M., Takeshige, K., Baba, N., & Ohsumi, Y. (1994). Ultrastructural analysis of the autophagic process in yeast : Detection of autophagosomes and their characterization. *The Journal of Cell Biology*, *124*(6), 903-913. https://doi.org/10.1083/jcb.124.6.903

Ballabio, A., & Bonifacino, J. S. (2020). Lysosomes as dynamic regulators of cell and organismal homeostasis. *Nature Reviews Molecular Cell Biology*, *21*(2), 101-118. https://doi.org/10.1038/s41580-019-0185-4

Ballabio, A., & Gieselmann, V. (2009). Lysosomal disorders : From storage to cellular damage. *Biochimica et Biophysica Acta (BBA) - Molecular Cell Research*, *1793*(4), 684-696. https://doi.org/10.1016/j.bbamcr.2008.12.001

Banerjee, P., Joo, J. B., Buse, J. T., & Dawson, G. (1995). Differential solubilization of lipids along with membrane proteins by different classes of detergents. *Chemistry and Physics of Lipids*, *77*(1), 65-78. https://doi.org/10.1016/0009-3084(95)02455-R

Bar-Peled, L., & Sabatini, D. M. (2014). Regulation of mTORC1 by amino acids. *Trends in Cell Biology*, *24*(7), 400-406. https://doi.org/10.1016/j.tcb.2014.03.003

Battaglioni, S., Benjamin, D., Wälchli, M., Maier, T., & Hall, M. N. (2022). mTOR substrate phosphorylation in growth control. *Cell*, *185*(11), 1814-1836. https://doi.org/10.1016/j.cell.2022.04.013

Beach, D. L., Salmon, E. D., & Bloom, K. (1999). Localization and anchoring of mRNA in budding yeast. *Current Biology*, *9*(11), 569-S1. https://doi.org/10.1016/S0960-9822(99)80260-7

Belfiore, A., Malaguarnera, R., Vella, V., Lawrence, M. C., Sciacca, L., Frasca, F., Morrione, A., & Vigneri, R. (2017). Insulin Receptor Isoforms in Physiology and Disease : An Updated View. *Endocrine Reviews*, *38*(5), 379-431. https://doi.org/10.1210/er.2017-00073

Bellaïche, Y., Gho, M., Kaltschmidt, J. A., Brand, A. H., & Schweisguth, F. (2001). Frizzled regulates localization of cell-fate determinants and mitotic spindle rotation during asymmetric cell division. *Nature Cell Biology*, *3*(1), 50-57. https://doi.org/10.1038/35050558

Bernsel, A., Viklund, H., Hennerdal, A., & Elofsson, A. (2009). TOPCONS : Consensus prediction of membrane protein topology. *Nucleic Acids Research*, *37*(Web Server), W465-W468. https://doi.org/10.1093/nar/gkp363

Bhat, P. J., & Murthy, T. V. S. (2001). Transcriptional control of the *GAL/MEL* regulon of yeast *Saccharomyces cerevisiae* : Mechanism of galactose-mediated signal transduction. *Molecular Microbiology*, *40*(5), 1059-1066. https://doi.org/10.1046/j.1365-2958.2001.02421.x

Bhattacharjee, S., Deterding, L. J., Chatterjee, S., Jiang, J., Ehrenshaft, M., Lardinois, O., Ramirez, D. C., Tomer, K. B., & Mason, R. P. (2011). Site-specific radical formation in DNA induced by

Cu(II)–H2O2 oxidizing system, using ESR, immuno-spin trapping, LC-MS, and MS/MS. *Free Radical Biology and Medicine*, *50*(11), 1536-1545. https://doi.org/10.1016/j.freeradbiomed.2011.02.034

Boivin, M., Pfister, V., Gaucherot, A., Ruffenach, F., Negroni, L., Sellier, C., & Charlet-Berguerand, N. (2020). Reduced autophagy upon C9ORF72 loss synergizes with dipeptide repeat protein toxicity in G4C2 repeat expansion disorders. *The EMBO Journal*, *39*(4), e100574. https://doi.org/10.15252/embj.2018100574

Braulke, T., & Bonifacino, J. S. (2009). Sorting of lysosomal proteins. *Biochimica et Biophysica Acta (BBA) - Molecular Cell Research*, *1793*(4), 605-614. https://doi.org/10.1016/j.bbamcr.2008.10.016

Britt, R. D., Campbell, K. A., Peloquin, J. M., Gilchrist, M. L., Aznar, C. P., Dicus, M. M., Robblee, J., & Messinger, J. (2004). Recent pulsed EPR studies of the Photosystem II oxygen-evolving complex : Implications as to water oxidation mechanisms. *Biochimica et Biophysica Acta (BBA) - Bioenergetics*, *1655*, 158-171. https://doi.org/10.1016/j.bbabio.2003.11.009

Butler, J. D., & Zatz, M. (1984). Pantethine and cystamine deplete cystine from cystinotic fibroblasts via efflux of cysteamine-cysteine mixed disulfide. *Journal of Clinical Investigation*, *74*(2), 411-416. https://doi.org/10.1172/JCI111436

Calvo, R., Passeggi, M. C., Isaacson, R. A., Okamura, M. Y., & Feher, G. (1990). Electron paramagnetic resonance investigation of photosynthetic reaction centers from Rhodobacter sphaeroides R-26 in which Fe2+ was replaced by Cu2+. Determination of hyperfine interactions and exchange and dipole-dipole interactions between Cu2+ and QA-. *Biophysical Journal*, *58*(1), 149-165. https://doi.org/10.1016/S0006-3495(90)82361-4

Canul-Tec, J. C., Assal, R., Cirri, E., Legrand, P., Brier, S., Chamot-Rooke, J., & Reyes, N. (2017). Structure and allosteric inhibition of excitatory amino acid transporter 1. *Nature*, *544*(7651), 446-451. https://doi.org/10.1038/nature22064

Carlesso, A., Delgado, R., Ruiz Isant, O., Uwangue, O., Valli, D., Bill, R. M., & Hedfalk, K. (2022). Yeast as a tool for membrane protein production and structure determination. *FEMS Yeast Research*, *22*(1), foac047. https://doi.org/10.1093/femsyr/foac047

Carpenter, E. P., Beis, K., Cameron, A. D., & Iwata, S. (2008). Overcoming the challenges of membrane protein crystallography. *Current Opinion in Structural Biology*, *18*(5), 581-586. https://doi.org/10.1016/j.sbi.2008.07.001

Casagrande, F., Ratera, M., Schenk, A. D., Chami, M., Valencia, E., Lopez, J. M., Torrents, D., Engel, A., Palacin, M., & Fotiadis, D. (2008). Projection Structure of a Member of the Amino Acid/Polyamine/Organocation Transporter Superfamily. *Journal of Biological Chemistry*, *283*(48), 33240-33248. https://doi.org/10.1074/jbc.M806917200

Castellano, B. M., Thelen, A. M., Moldavski, O., Feltes, M., Van Der Welle, R. E. N., Mydock-McGrane, L., Jiang, X., Van Eijkeren, R. J., Davis, O. B., Louie, S. M., Perera, R. M., Covey, D. F., Nomura, D. K., Ory, D. S., & Zoncu, R. (2017). Lysosomal cholesterol activates mTORC1 via an SLC38A9–Niemann-Pick C1 signaling complex. *Science*, *355*(6331), 1306-1311. https://doi.org/10.1126/science.aag1417

Chantranupong, L., Wolfson, R. L., & Sabatini, D. M. (2015). Nutrient-Sensing Mechanisms across Evolution. *Cell*, *161*(1), 67-83. https://doi.org/10.1016/j.cell.2015.02.041

Chapel, A., Kieffer-Jaquinod, S., Sagné, C., Verdon, Q., Ivaldi, C., Mellal, M., Thirion, J., Jadot, M., Bruley, C., Garin, J., Gasnier, B., & Journet, A. (2013). An Extended Proteome Map of the Lysosomal Membrane Reveals Novel Potential Transporters. *Molecular & Cellular Proteomics*, *12*(6), 1572-1588. https://doi.org/10.1074/mcp.M112.021980

Chaptal, V., Delolme, F., Kilburg, A., Magnard, S., Montigny, C., Picard, M., Prier, C., Monticelli, L., Bornert, O., Agez, M., Ravaud, S., Orelle, C., Wagner, R., Jawhari, A., Broutin, I., Pebay-Peyroula, E., Jault, J.-M., Kaback, H. R., Le Maire, M., & Falson, P. (2017). Quantification of Detergents Complexed with Membrane Proteins. *Scientific Reports*, *7*(1), 41751. https://doi.org/10.1038/srep41751

Cirri, E., Brier, S., Assal, R., Canul-Tec, J. C., Chamot-Rooke, J., & Reyes, N. (2018). Consensus designs and thermal stability determinants of a human glutamate transporter. *eLife*, *7*, e40110. https://doi.org/10.7554/eLife.40110

Claxton, D. P., Kazmier, K., Mishra, S., & Mchaourab, H. S. (2015). Navigating Membrane Protein Structure, Dynamics, and Energy Landscapes Using Spin Labeling and EPR Spectroscopy. In *Methods in Enzymology* (Vol. 564, p. 349-387). Elsevier. https://doi.org/10.1016/bs.mie.2015.07.026

Conner, S. D., & Schmid, S. L. (2003). Regulated portals of entry into the cell. *Nature*, *422*(6927), 37-44. https://doi.org/10.1038/nature01451

Cools, M., Lissoir, S., Bodo, E., Ulloa-Calzonzin, J., DeLuna, A., Georis, I., & André, B. (2020). Nitrogen coordinated import and export of arginine across the yeast vacuolar membrane. *PLOS Genetics*, *16*(8), e1008966. https://doi.org/10.1371/journal.pgen.1008966

Corbier, C., & Sellier, C. (2017). C9ORF72 is a GDP/GTP exchange factor for Rab8 and Rab39 and regulates autophagy. *Small GTPases*, *8*(3), 181-186. https://doi.org/10.1080/21541248.2016.1212688

Cornish, V. W., Benson, D. R., Altenbach, C. A., Hideg, K., Hubbell, W. L., & Schultz, P. G. (1994). Site-specific incorporation of biophysical probes into proteins. *Proceedings of the National Academy of Sciences*, *91*(8), 2910-2914. https://doi.org/10.1073/pnas.91.8.2910

Corrionero, A., & Horvitz, H. R. (2018). A C9orf72 ALS/FTD Ortholog Acts in Endolysosomal Degradation and Lysosomal Homeostasis. *Current Biology*, *28*(10), 1522-1535.e5. https://doi.org/10.1016/j.cub.2018.03.063

Crichton, P. G., Lee, Y., Ruprecht, J. J., Cerson, E., Thangaratnarajah, C., King, M. S., & Kunji, E. R. S. (2015). Trends in Thermostability Provide Information on the Nature of Substrate, Inhibitor, and Lipid Interactions with Mitochondrial Carriers. *Journal of Biological Chemistry*, *290*(13), 8206-8217. https://doi.org/10.1074/jbc.M114.616607

Cui, Z., Joiner, A. M. N., Jansen, R. M., & Hurley, J. H. (2023). Amino acid sensing and lysosomal signaling complexes. *Current Opinion in Structural Biology*, *79*, 102544. https://doi.org/10.1016/j.sbi.2023.102544

De Duve, C. (2005). The lysosome turns fifty. *Nature Cell Biology*, *7*(9), 847-849. https://doi.org/10.1038/ncb0905-847

DeJesus-Hernandez, M., Mackenzie, I. R., Boeve, B. F., Boxer, A. L., Baker, M., Rutherford, N. J., Nicholson, A. M., Finch, N. A., Flynn, H., Adamson, J., Kouri, N., Wojtas, A., Sengdy, P., Hsiung, G.-Y. R., Karydas, A., Seeley, W. W., Josephs, K. A., Coppola, G., Geschwind, D. H., … Rademakers, R. (2011). Expanded GGGGCC Hexanucleotide Repeat in Noncoding Region of C9ORF72 Causes Chromosome 9p-Linked FTD and ALS. *Neuron*, *72*(2), 245-256. https://doi.org/10.1016/j.neuron.2011.09.011

Della Valle, M. C., Sleat, D. E., Zheng, H., Moore, D. F., Jadot, M., & Lobel, P. (2011). Classification of Subcellular Location by Comparative Proteomic Analysis of Native and Density-shifted Lysosomes. *Molecular & Cellular Proteomics*, *10*(4), M110.006403. https://doi.org/10.1074/mcp.M110.006403

Deretic, V., & Levine, B. (2009). Autophagy, Immunity, and Microbial Adaptations. *Cell Host & Microbe*, *5*(6), 527-549. https://doi.org/10.1016/j.chom.2009.05.016

Di Fiore, P. P., & Von Zastrow, M. (2014). Endocytosis, Signaling, and Beyond. *Cold Spring Harbor Perspectives in Biology*, *6*(8), a016865-a016865. https://doi.org/10.1101/cshperspect.a016865

Diallinas, G. (2017). Transceptors as a functional link of transporters and receptors. *Microbial Cell*, *4*(3), 69-73. https://doi.org/10.15698/mic2017.03.560

Drew, D., & Boudker, O. (2016). Shared Molecular Mechanisms of Membrane Transporters. *Annual Review of Biochemistry*, *85*(1), 543-572. https://doi.org/10.1146/annurev-biochem-060815-014520

Duquesne, K., Prima, V., & Sturgis, J. N. (2016). Membrane Protein Solubilization and Composition of Protein Detergent Complexes. In I. Mus-Veteau (Éd.), *Heterologous Expression of Membrane Proteins* (Vol. 1432, p. 243-260). Springer New York. https://doi.org/10.1007/978-1-4939-3637-3_15

Elmonem, M. A., Veys, K. R., Soliman, N. A., Van Dyck, M., Van Den Heuvel, L. P., & Levtchenko, E. (2016). Cystinosis : A review. *Orphanet Journal of Rare Diseases*, *11*(1), 47. https://doi.org/10.1186/s13023-016-0426-y

Errasti-Murugarren, E., Bartoccioni, P., & Palacín, M. (2021). Membrane Protein Stabilization Strategies for Structural and Functional Studies. *Membranes*, *11*(2), 155. https://doi.org/10.3390/membranes11020155

Estes, P. S., Ho, G. L. Y., Narayanan, R., & Ramaswami, M. (2000). Synaptic Localization and Restricted Diffusion of a *Drosophila* Neuronal Synaptobrevin—Green Fluorescent Protein Chimera *in Vivo*. *Journal of Neurogenetics*, *13*(4), 233-255. https://doi.org/10.3109/01677060009084496

Eswar, N., Webb, B., Marti-Renom, M. A., Madhusudhan, M. S., Eramian, D., Shen, M., Pieper, U., & Sali, A. (2006). Comparative Protein Structure Modeling Using Modeller. *Current Protocols in Bioinformatics*, *15*(1). https://doi.org/10.1002/0471250953.bi0506s15

Farquhar, M. G., Bainton, D. F., Baggiolini, M., & De Duve, C. (1972). CYTOCHEMICAL LOCALIZATION OF ACID PHOSPHATASE ACTIVITY IN GRANULE FRACTIONS FROM RABBIT POLYMORPHONUCLEAR LEUKOCYTES. *The Journal of Cell Biology*, *54*(1), 141-156. https://doi.org/10.1083/jcb.54.1.141

Forgac, M. (2007). Vacuolar ATPases : Rotary proton pumps in physiology and pathophysiology. *Nature Reviews Molecular Cell Biology*, *8*(11), 917-929. https://doi.org/10.1038/nrm2272

Forrest, L. R., Krämer, R., & Ziegler, C. (2011). The structural basis of secondary active transport mechanisms. *Biochimica et Biophysica Acta (BBA) - Bioenergetics*, *1807*(2), 167-188. https://doi.org/10.1016/j.bbabio.2010.10.014

Forsberg, H., & Ljungdahl, P. (2001). Sensors of extracellular nutrients in Saccharomyces cerevisiae. *Current Genetics*, *40*(2), 91-109. https://doi.org/10.1007/s002940100244

Fredriksson, R., Nordström, K. J. V., Stephansson, O., Hägglund, M. G. A., & Schiöth, H. B. (2008). The solute carrier (SLC) complement of the human genome : Phylogenetic classification reveals four major families. *FEBS Letters*, *582*(27), 3811-3816. https://doi.org/10.1016/j.febslet.2008.10.016

Gahl, W. A., Thoene, J. G., & Schneider, J. A. (2002). Cystinosis. *New England Journal of Medicine*, *347*(2), 111-121. https://doi.org/10.1056/NEJMra020552

Gasnier, B. (2021). Plug-and-socket mechanisms in nutrient sensing by lysosomal amino acid transporters. *Proceedings of the National Academy of Sciences*, *118*(13), e2102173118. https://doi.org/10.1073/pnas.2102173118

Gerondopoulos, A., Bräuer, P., Sobajima, T., Wu, Z., Parker, J. L., Biggin, P. C., Barr, F. A., & Newstead, S. (2021). A signal capture and proofreading mechanism for the KDEL-receptor explains selectivity and dynamic range in ER retrieval. *eLife*, *10*, e68380. https://doi.org/10.7554/eLife.68380

Gewering, T., Januliene, D., Ries, A. B., & Moeller, A. (2018). Know your detergents : A case study on detergent background in negative stain electron microscopy. *Journal of Structural Biology*, *203*(3), 242-246. https://doi.org/10.1016/j.jsb.2018.05.008

Gibbons, J. J., Abraham, R. T., & Yu, K. (2009). Mammalian Target of Rapamycin : Discovery of Rapamycin Reveals a Signaling Pathway Important for Normal and Cancer Cell Growth. *Seminars in Oncology*, *36*, S3-S17. https://doi.org/10.1053/j.seminoncol.2009.10.011

Gietz, R. D., & Schiestl, R. H. (2007). High-efficiency yeast transformation using the LiAc/SS carrier DNA/PEG method. *Nature Protocols*, *2*(1), 31-34. https://doi.org/10.1038/nprot.2007.13

Gould, G. W., & Lippincott-Schwartz, J. (2009). New roles for endosomes : From vesicular carriers to multi-purpose platforms. *Nature Reviews Molecular Cell Biology*, *10*(4), 287-292. https://doi.org/10.1038/nrm2652

Guarente, L., Yocum, R. R., & Gifford, P. (1982). A GAL10-CYC1 hybrid yeast promoter identifies the GAL4 regulatory region as an upstream site. *Proceedings of the National Academy of Sciences*, *79*(23), 7410-7414. https://doi.org/10.1073/pnas.79.23.7410

Guertin, D. A., & Sabatini, D. M. (2007). Defining the Role of mTOR in Cancer. *Cancer Cell*, *12*(1), 9-22. https://doi.org/10.1016/j.ccr.2007.05.008

Guo, X., Schmiege, P., Assafa, T. E., Wang, R., Xu, Y., Donnelly, L., Fine, M., Ni, X., Jiang, J., Millhauser, G., Feng, L., & Li, X. (2022). Structure and mechanism of human cystine exporter cystinosin. *Cell*, *185*(20), 3739-3752.e18. https://doi.org/10.1016/j.cell.2022.08.020

Haeusler, A. R., Donnelly, C. J., Periz, G., Simko, E. A. J., Shaw, P. G., Kim, M.-S., Maragakis, N. J., Troncoso, J. C., Pandey, A., Sattler, R., Rothstein, J. D., & Wang, J. (2014). C9orf72 nucleotide repeat structures initiate molecular cascades of disease. *Nature*, *507*(7491), 195-200. https://doi.org/10.1038/nature13124

Han, L., Zhu, Y., Liu, M., Zhou, Y., Lu, G., Lan, L., Wang, X., Zhao, Y., & Zhang, X. C. (2017). Molecular mechanism of substrate recognition and transport by the AtSWEET13 sugar transporter. *Proceedings of the National Academy of Sciences*, *114*(38), 10089-10094. https://doi.org/10.1073/pnas.1709241114

Hay, N., & Sonenberg, N. (2004). Upstream and downstream of mTOR. *Genes & Development*, *18*(16), 1926-1945. https://doi.org/10.1101/gad.1212704

Heinz, L. X., Lee, J., Kapoor, U., Kartnig, F., Sedlyarov, V., Papakostas, K., César-Razquin, A., Essletzbichler, P., Goldmann, U., Stefanovic, A., Bigenzahn, J. W., Scorzoni, S., Pizzagalli, M. D., Bensimon, A., Müller, A. C., King, F. J., Li, J., Girardi, E., Mbow, M. L., … Superti-Furga, G. (2020). TASL is the SLC15A4-associated adaptor for IRF5 activation by TLR7–9. *Nature*, *581*(7808), 316-322. https://doi.org/10.1038/s41586-020-2282-0

Helenius, A., & Simons, K. (1975). Solubilization of membranes by detergents. *Biochimica et Biophysica Acta (BBA) - Reviews on Biomembranes*, *415*(1), 29-79. https://doi.org/10.1016/0304-4157(75)90016-7

Ho, J., Moyes, D. L., Tavassoli, M., & Naglik, J. R. (2017). The Role of ErbB Receptors in Infection. *Trends in Microbiology*, *25*(11), 942-952. https://doi.org/10.1016/j.tim.2017.04.009

Hundal, H. S., & Taylor, P. M. (2009). Amino acid transceptors : Gate keepers of nutrient exchange and regulators of nutrient signaling. *American Journal of Physiology-Endocrinology and Metabolism*, *296*(4), E603-E613. https://doi.org/10.1152/ajpendo.91002.2008

Ishida, Y., Nayak, S., Mindell, J. A., & Grabe, M. (2013). A model of lysosomal pH regulation. *Journal of General Physiology*, *141*(6), 705-720. https://doi.org/10.1085/jgp.201210930

Jacquot, A., Montigny, C., Hennrich, H., Barry, R., Le Maire, M., Jaxel, C., Holthuis, J., Champeil, P., & Lenoir, G. (2012). Phosphatidylserine Stimulation of Drs2p·Cdc50p Lipid Translocase Dephosphorylation Is Controlled by Phosphatidylinositol-4-phosphate. *Journal of Biological Chemistry*, *287*(16), 13249-13261. https://doi.org/10.1074/jbc.M111.313916

Jaehme, M., Guskov, A., & Slotboom, D. J. (2014). Crystal structure of the vitamin B3 transporter PnuC, a full-length SWEET homolog. *Nature Structural & Molecular Biology*, *21*(11), 1013-1015. https://doi.org/10.1038/nsmb.2909

Jain, A., & Zoncu, R. (2021). Picking the arginine lock on PQLC2 cycling. *Proceedings of the National Academy of Sciences*, *118*(35), e2112682118. https://doi.org/10.1073/pnas.2112682118

Jeyakumar, M., Dwek, R. A., Butters, T. D., & Platt, F. M. (2005). Storage solutions : Treating lysosomal disorders of the brain. *Nature Reviews Neuroscience*, *6*(9), 713-725. https://doi.org/10.1038/nrn1725

Jézégou, A., Llinares, E., Anne, C., Kieffer-Jaquinod, S., O'Regan, S., Aupetit, J., Chabli, A., Sagné, C., Debacker, C., Chadefaux-Vekemans, B., Journet, A., André, B., & Gasnier, B. (2012). Heptahelical protein PQLC2 is a lysosomal cationic amino acid exporter underlying the action of cysteamine in cystinosis therapy. *Proceedings of the National Academy of Sciences*, *109*(50). https://doi.org/10.1073/pnas.1211198109

Jin, B., Odongo, S., Radwanska, M., & Magez, S. (2023). NANOBODIES® : A Review of Diagnostic and Therapeutic Applications. *International Journal of Molecular Sciences*, *24*(6), 5994. https://doi.org/10.3390/ijms24065994

Johnston, M. (1999). Feasting, fasting and fermenting : Glucose sensing in yeast and other cells. *Trends in Genetics*, *15*(1), 29-33. https://doi.org/10.1016/S0168-9525(98)01637-0

Jojoa-Cruz, S., Saotome, K., Murthy, S. E., Tsui, C. C. A., Sansom, M. S., Patapoutian, A., & Ward, A. B. (2018). Cryo-EM structure of the mechanically activated ion channel OSCA1.2. *eLife*, *7*, e41845. https://doi.org/10.7554/eLife.41845

Jordá, T., & Puig, S. (2020). Regulation of Ergosterol Biosynthesis in Saccharomyces cerevisiae. *Genes*, *11*(7), 795. https://doi.org/10.3390/genes11070795

Jung, J., Genau, H. M., & Behrends, C. (2015). Amino Acid-Dependent mTORC1 Regulation by the Lysosomal Membrane Protein SLC38A9. *Molecular and Cellular Biology*, *35*(14), 2479-2494. https://doi.org/10.1128/MCB.00125-15

Junge, F., Schneider, B., Reckel, S., Schwarz, D., Dötsch, V., & Bernhard, F. (2008). Large-scale production of functional membrane proteins. *Cellular and Molecular Life Sciences*, *65*(11), 1729-1755. https://doi.org/10.1007/s00018-008-8067-5

Kalatzis, V. (2001). Cystinosin, the protein defective in cystinosis, is a H+-driven lysosomal cystine transporter. *The EMBO Journal*, *20*(21), 5940-5949. https://doi.org/10.1093/emboj/20.21.5940

Kalatzis, V. (2004). Molecular pathogenesis of cystinosis : Effect of CTNS mutations on the transport activity and subcellular localization of cystinosin. *Human Molecular Genetics*, *13*(13), 1361-1371. https://doi.org/10.1093/hmg/ddh152

Kaur, J., & Debnath, J. (2015). Autophagy at the crossroads of catabolism and anabolism. *Nature Reviews Molecular Cell Biology*, *16*(8), 461-472. https://doi.org/10.1038/nrm4024

Kawano-Kawada, M., Manabe, K., Ichimura, H., Kimura, T., Harada, Y., Ikeda, K., Tanaka, S., Kakinuma, Y., & Sekito, T. (2019). A PQ-loop protein Ypq2 is involved in the exchange of arginine and histidine across the vacuolar membrane of Saccharomyces cerevisiae. *Scientific Reports*, *9*(1), 15018. https://doi.org/10.1038/s41598-019-51531-z

Kawate, T., & Gouaux, E. (2006). Fluorescence-Detection Size-Exclusion Chromatography for Precrystallization Screening of Integral Membrane Proteins. *Structure*, *14*(4), 673-681. https://doi.org/10.1016/j.str.2006.01.013

Kim, E., Goraksha-Hicks, P., Li, L., Neufeld, T. P., & Guan, K.-L. (2008). Regulation of TORC1 by Rag GTPases in nutrient response. *Nature Cell Biology*, *10*(8), 935-945. https://doi.org/10.1038/ncb1753

King, M. S., & Kunji, E. R. S. (2020). Expression and Purification of Membrane Proteins in Saccharomyces cerevisiae. In C. Perez & T. Maier (Éds.), *Expression, Purification, and Structural Biology of Membrane Proteins* (Vol. 2127, p. 47-61). Springer US. https://doi.org/10.1007/978-1-0716-0373-4_4

Klug, C. S., & & Feix, J. B. (2005). SDSL: A survey of biological applications. In Biomedical EPR, Part B: Methodology, Instrumentation, and Dynamics. *Boston, MA: Springer US.*

Klug, C. S., & Feix, J. B. (2008). Methods and Applications of Site-Directed Spin Labeling EPR Spectroscopy. In *Methods in Cell Biology* (Vol. 84, p. 617-658). Elsevier. https://doi.org/10.1016/S0091-679X(07)84020-9

Klumperman, J., & Raposo, G. (2014). The Complex Ultrastructure of the Endolysosomal System. *Cold Spring Harbor Perspectives in Biology*, *6*(10), a016857-a016857. https://doi.org/10.1101/cshperspect.a016857

Korolchuk, V. I., Saiki, S., Lichtenberg, M., Siddiqi, F. H., Roberts, E. A., Imarisio, S., Jahreiss, L., Sarkar, S., Futter, M., Menzies, F. M., O'Kane, C. J., Deretic, V., & Rubinsztein, D. C. (2011). Lysosomal positioning coordinates cellular nutrient responses. *Nature Cell Biology*, *13*(4), 453-460. https://doi.org/10.1038/ncb2204

Kowalczyk, L., Ratera, M., Paladino, A., Bartoccioni, P., Errasti-Murugarren, E., Valencia, E., Portella, G., Bial, S., Zorzano, A., Fita, I., Orozco, M., Carpena, X., Vázquez-Ibar, J. L., & Palacín, M. (2011). Molecular basis of substrate-induced permeation by an amino acid antiporter. *Proceedings of the National Academy of Sciences*, *108*(10), 3935-3940. https://doi.org/10.1073/pnas.1018081108

Kubala, M. H., Kovtun, O., Alexandrov, K., & Collins, B. M. (2010). Structural and thermodynamic analysis of the GFP:GFP-nanobody complex. *Protein Science*, *19*(12), 2389-2401. https://doi.org/10.1002/pro.519

Kunji, E. R. S., Harding, M., Butler, P. J. G., & Akamine, P. (2008). Determination of the molecular mass and dimensions of membrane proteins by size exclusion chromatography. *Methods*, *46*(2), 62-72. https://doi.org/10.1016/j.ymeth.2008.10.020

Laemmli, U. K. (1970). Cleavage of Structural Proteins during the Assembly of the Head of Bacteriophage T4. *Nature*, *227*(5259), 680-685. https://doi.org/10.1038/227680a0

Lamy, A., Macarini-Bruzaferro, E., Dieudonné, T., Perálvarez-Marín, A., Lenoir, G., Montigny, C., Le Maire, M., & Vázquez-Ibar, J. L. (2021). ATP2, The essential P4-ATPase of malaria parasites, catalyzes lipid-stimulated ATP hydrolysis in complex with a Cdc50 β-subunit. *Emerging Microbes & Infections*, *10*(1), 132-147. https://doi.org/10.1080/22221751.2020.1870413

Lawrence, R. E., & Zoncu, R. (2019). The lysosome as a cellular centre for signalling, metabolism and quality control. *Nature Cell Biology*, *21*(2), 133-142. https://doi.org/10.1038/s41556-018-0244-7

Lee, Y., Nishizawa, T., Yamashita, K., Ishitani, R., & Nureki, O. (2015). Structural basis for the facilitative diffusion mechanism by SemiSWEET transporter. *Nature Communications*, *6*(1), 6112. https://doi.org/10.1038/ncomms7112

Lehmann, M., Pasamontes, L., Lassen, S. F., & Wyss, M. (2000). The consensus concept for thermostability engineering of proteins. *Biochimica et Biophysica Acta (BBA) - Protein Structure and Molecular Enzymology*, *1543*(2), 408-415. https://doi.org/10.1016/S0167-4838(00)00238-7

Lei, H.-T., Ma, J., Sanchez Martinez, S., & Gonen, T. (2018). Crystal structure of arginine-bound lysosomal transporter SLC38A9 in the cytosol-open state. *Nature Structural & Molecular Biology*, *25*(6), 522-527. https://doi.org/10.1038/s41594-018-0072-2

Lei, H.-T., Mu, X., Hattne, J., & Gonen, T. (2021). A conformational change in the N terminus of SLC38A9 signals mTORC1 activation. *Structure*, *29*(5), 426-432.e8. https://doi.org/10.1016/j.str.2020.11.014

Lenoir, G., Dieudonné, T., Lamy, A., Lejeune, M., Vazquez-Ibar, J., & Montigny, C. (2018). Screening of Detergents for Stabilization of Functional Membrane Proteins. *Current Protocols in Protein Science*, *93*(1), e59. https://doi.org/10.1002/cpps.59

Lenoir, G., Menguy, T., Corre, F., Montigny, C., Pedersen, P. A., Thinès, D., Le Maire, M., & Falson, P. (2002). Overproduction in yeast and rapid and efficient purification of the rabbit SERCA1a Ca2+-ATPase. *Biochimica et Biophysica Acta (BBA) - Biomembranes*, *1560*(1-2), 67-83. https://doi.org/10.1016/S0005-2736(01)00458-8

Leray, X., Conti, R., Li, Y., Debacker, C., Castelli, F., Fenaille, F., Zdebik, A. A., Pusch, M., & Gasnier, B. (2021). Arginine-selective modulation of the lysosomal transporter PQLC2 through a gate-tuning mechanism. *Proceedings of the National Academy of Sciences*, *118*(32), e2025315118. https://doi.org/10.1073/pnas.2025315118

Levine, T. P., Daniels, R. D., Gatta, A. T., Wong, L. H., & Hayes, M. J. (2013). The product of C9orf72, a gene strongly implicated in neurodegeneration, is structurally related to DENN Rab-GEFs. *Bioinformatics*, *29*(4), 499-503. https://doi.org/10.1093/bioinformatics/bts725

Lin, S.-H., & Guidotti, G. (2009). Chapter 35 Purification of Membrane Proteins. In *Methods in Enzymology* (Vol. 463, p. 619-629). Elsevier. https://doi.org/10.1016/S0076-6879(09)63035-4

Liu, B., Du, H., Rutkowski, R., Gartner, A., & Wang, X. (2012). LAAT-1 Is the Lysosomal Lysine/Arginine Transporter That Maintains Amino Acid Homeostasis. *Science*, *337*(6092), 351-354. https://doi.org/10.1126/science.1220281

Liu, G. Y., & Sabatini, D. M. (2020). mTOR at the nexus of nutrition, growth, ageing and disease. *Nature Reviews Molecular Cell Biology*, *21*(4), 183-203. https://doi.org/10.1038/s41580-019-0199-y

Llinares, E., Barry, A. O., & André, B. (2015). The AP-3 adaptor complex mediates sorting of yeast and mammalian PQ-loop-family basic amino acid transporters to the vacuolar/lysosomal membrane. *Scientific Reports*, *5*(1), 16665. https://doi.org/10.1038/srep16665

Löbel, M., Salphati, S. P., El Omari, K., Wagner, A., Tucker, S. J., Parker, J. L., & Newstead, S. (2022). Structural basis for proton coupled cystine transport by cystinosin. *Nature Communications*, *13*(1), 4845. https://doi.org/10.1038/s41467-022-32589-2

Majd, H., King, M. S., Palmer, S. M., Smith, A. C., Elbourne, L. D., Paulsen, I. T., Sharples, D., Henderson, P. J., & Kunji, E. R. (2018). Screening of candidate substrates and coupling ions of transporters by thermostability shift assays. *eLife*, *7*, e38821. https://doi.org/10.7554/eLife.38821

Majounie, E., Renton, A. E., Mok, K., Dopper, E. G., Waite, A., Rollinson, S., Chiò, A., Restagno, G., Nicolaou, N., Simon-Sanchez, J., Van Swieten, J. C., Abramzon, Y., Johnson, J. O., Sendtner, M., Pamphlett, R., Orrell, R. W., Mead, S., Sidle, K. C., Houlden, H., … Traynor, B. J. (2012). Frequency of the C9orf72 hexanucleotide repeat expansion in patients with amyotrophic lateral sclerosis and frontotemporal dementia : A cross-sectional study. *The Lancet Neurology*, *11*(4), 323-330. https://doi.org/10.1016/S1474-4422(12)70043-1

Matile, P., & Wiemken, A. (1967). The vacuole as the lysosome of the yeast cell. *Archiv F[illegible]r Mikrobiologie*, *56*(2), 148-155. https://doi.org/10.1007/BF00408765

Mazhab-Jafari, M. T., Rohou, A., Schmidt, C., Bueler, S. A., Benlekbir, S., Robinson, C. V., & Rubinstein, J. L. (2016). Atomic model for the membrane-embedded VO motor of a eukaryotic V-ATPase. *Nature*, *539*(7627), 118-122. https://doi.org/10.1038/nature19828

Meng, J., & Ferguson, S. M. (2018). GATOR1-dependent recruitment of FLCN–FNIP to lysosomes coordinates Rag GTPase heterodimer nucleotide status in response to amino acids. *Journal of Cell Biology*, *217*(8), 2765-2776. https://doi.org/10.1083/jcb.201712177

Mindell, J. A. (2012). Lysosomal Acidification Mechanisms. *Annual Review of Physiology*, *74*(1), 69-86. https://doi.org/10.1146/annurev-physiol-012110-142317

Möbius, K., Savitsky, A., Schnegg, A., Plato, M., & Fuchs, M. (2005). High-field EPR spectroscopy applied to biological systems : Characterization of molecular switches for electron and ion transfer. *Phys. Chem. Chem. Phys.*, *7*(1), 19-42. https://doi.org/10.1039/B412180E

Morin, P., Sagné, C., & Gasnier, B. (2004). Functional characterization of wild-type and mutant human sialin. *The EMBO Journal*, *23*(23), 4560-4570. https://doi.org/10.1038/sj.emboj.7600464

Nielsen, J. (2013). Production of biopharmaceutical proteins by yeast : Advances through metabolic engineering. *Bioengineered*, *4*(4), 207-211. https://doi.org/10.4161/bioe.22856

Niggemann, M., & Steipe, B. (2000). Exploring local and non-local interactions for protein stability by structural motif engineering 1 1Edited by A. R. Fersht. *Journal of Molecular Biology*, *296*(1), 181-195. https://doi.org/10.1006/jmbi.1999.3385

Nixon, R. A. (2013). The role of autophagy in neurodegenerative disease. *Nature Medicine*, *19*(8), 983-997. https://doi.org/10.1038/nm.3232

Nörpel, J., Cavadini, S., Schenk, A. D., Graff-Meyer, A., Hess, D., Seebacher, J., Chao, J. A., & Bhaskar, V. (2021). Structure of the human C9orf72-SMCR8 complex reveals a multivalent protein interaction architecture. *PLOS Biology*, *19*(7), e3001344. https://doi.org/10.1371/journal.pbio.3001344

NOVIKOFF, A., B., BEAUFAY, H., & & DE DUVE, C. (1956). Electron microscopy of lysosomerich fractions from rat liver. *The Journal of biophysical and biochemical cytology*, 179-184.

Oda, K., Lee, Y., Wiriyasermkul, P., Tanaka, Y., Takemoto, M., Yamashita, K., Nagamori, S., Nishizawa, T., & Nureki, O. (2020). Consensus mutagenesis approach improves the thermal stability of system x_c^- transporter, xCT , and enables CRYO-EM analyses. *Protein Science*, *29*(12), 2398-2407. https://doi.org/10.1002/pro.3966

Ohage, E. C., Wirtz, P., Barnikow, J., & Steipe, B. (1999). Intrabody construction and expression. II. A synthetic catalytic Fv fragment. *Journal of Molecular Biology*, *291*(5), 1129-1134. https://doi.org/10.1006/jmbi.1999.3020

Okamoto, S., Naito, T., Shigetomi, R., Kosugi, Y., Nakayama, K., Takatsu, H., & Shin, H.-W. (2020). The N- or C-terminal cytoplasmic regions of P4-ATPases determine their cellular localization. *Molecular Biology of the Cell*, *31*(19), 2115-2124. https://doi.org/10.1091/mbc.E20-04-0225

Oliver, R. C., Lipfert, J., Fox, D. A., Lo, R. H., Doniach, S., & Columbus, L. (2013). Dependence of Micelle Size and Shape on Detergent Alkyl Chain Length and Head Group. *PLoS ONE*, *8*(5), e62488. https://doi.org/10.1371/journal.pone.0062488

Omasits, U., Ahrens, C. H., Müller, S., & Wollscheid, B. (2014). Protter : Interactive protein feature visualization and integration with experimental proteomic data. *Bioinformatics*, *30*(6), 884-886. https://doi.org/10.1093/bioinformatics/btt607

Ozcan, S. (1998). Glucose sensing and signaling by two glucose receptors in the yeast Saccharomyces cerevisiae. *The EMBO Journal*, *17*(9), 2566-2573. https://doi.org/10.1093/emboj/17.9.2566

Pandey, A., Shin, K., Patterson, R. E., Liu, X.-Q., & Rainey, J. K. (2016). Current strategies for protein production and purification enabling membrane protein structural biology. *Biochemistry and Cell Biology*, *94*(6), 507-527. https://doi.org/10.1139/bcb-2015-0143

Pang, W., & Hu, F. (2021). Cellular and physiological functions of C9ORF72 and implications for ALS/FTD. *Journal of Neurochemistry*, *157*(3), 334-350. https://doi.org/10.1111/jnc.15255

Park, T., Baek, M., Lee, H., & Seok, C. (2019). GalaxyTongDock : Symmetric and asymmetric *ab initio* protein–protein docking web server with improved energy parameters. *Journal of Computational Chemistry*, *40*(27), 2413-2417. https://doi.org/10.1002/jcc.25874

Parker, J. L., & Newstead, S. (2014). Method to increase the yield of eukaryotic membrane protein expression in *SACCHAROMYCES CEREVISIAE* for structural and functional studies. *Protein Science*, *23*(9), 1309-1314. https://doi.org/10.1002/pro.2507

Pedersen, B. P., Kumar, H., Waight, A. B., Risenmay, A. J., Roe-Zurz, Z., Chau, B. H., Schlessinger, A., Bonomi, M., Harries, W., Sali, A., Johri, A. K., & Stroud, R. M. (2013). Crystal structure of a eukaryotic phosphate transporter. *Nature*, *496*(7446), 533-536. https://doi.org/10.1038/nature12042

Perera, R. M., & Zoncu, R. (2016). The Lysosome as a Regulatory Hub. *Annual Review of Cell and Developmental Biology*, *32*(1), 223-253. https://doi.org/10.1146/annurev-cellbio-111315-125125

Petit, C. S., Roczniak-Ferguson, A., & Ferguson, S. M. (2013). Recruitment of folliculin to lysosomes supports the amino acid–dependent activation of Rag GTPases. *Journal of Cell Biology*, *202*(7), 1107-1122. https://doi.org/10.1083/jcb.201307084

Pisoni, R. L., & Thoene, J. G. (1985). Detection and characterization of carrier-mediated cationic amino acid transport in lysosomes of normal and cystinotic human fibroblasts. Role in therapeutic cystine removal? *The Journal of biological chemistry*, 4791-4798.

Platt, F. M. (2018). Emptying the stores : Lysosomal diseases and therapeutic strategies. *Nature Reviews Drug Discovery*, *17*(2), 133-150. https://doi.org/10.1038/nrd.2017.214

Platt, F. M., d'Azzo, A., Davidson, B. L., Neufeld, E. F., & Tifft, C. J. (2018). Lysosomal storage diseases. *Nature Reviews Disease Primers*, *4*(1), 27. https://doi.org/10.1038/s41572-018-0025-4

Pompon, D., Louerat, B., Bronine, A., & Urban, P. (1996). [6] Yeast expression of animal and plant P450s in optimized redox environments. In *Methods in Enzymology* (Vol. 272, p. 51-64). Elsevier. https://doi.org/10.1016/S0076-6879(96)72008-6

Rath, A., Glibowicka, M., Nadeau, V. G., Chen, G., & Deber, C. M. (2009). Detergent binding explains anomalous SDS-PAGE migration of membrane proteins. *Proceedings of the National Academy of Sciences*, *106*(6), 1760-1765. https://doi.org/10.1073/pnas.0813167106

Rawlings, A. E. (2018). Membrane protein engineering to the rescue. *Biochemical Society Transactions*, *46*(6), 1541-1549. https://doi.org/10.1042/BST20180140

Rebsamen, M., Pochini, L., Stasyk, T., De Araújo, M. E. G., Galluccio, M., Kandasamy, R. K., Snijder, B., Fauster, A., Rudashevskaya, E. L., Bruckner, M., Scorzoni, S., Filipek, P. A., Huber, K. V. M., Bigenzahn, J. W., Heinz, L. X., Kraft, C., Bennett, K. L., Indiveri, C., Huber, L. A., & Superti-Furga, G. (2015). SLC38A9 is a component of the lysosomal amino acid sensing machinery that controls mTORC1. *Nature*, *519*(7544), 477-481. https://doi.org/10.1038/nature14107

Reig, N., Del Rio, C., Casagrande, F., Ratera, M., Gelpié, J. L., Torrents, D., Henderson, P. J. F., Xie, H., Baldwin, S. A., Zorzano, A., Fotiadis, D., & Palacién, M. (2007). Functional and Structural Characterization of the First Prokaryotic Member of the L-Amino Acid Transporter (LAT) Family. *Journal of Biological Chemistry*, *282*(18), 13270-13281. https://doi.org/10.1074/jbc.M610695200

Renton, A. E., Majounie, E., Waite, A., Simón-Sánchez, J., Rollinson, S., Gibbs, J. R., Schymick, J. C., Laaksovirta, H., van Swieten, J. C., Myllykangas, L., Kalimo, H., Paetau, A., Abramzon, Y., Remes, A. M., Kaganovich, A., Scholz, S. W., Duckworth, J., Ding, J., Harmer, D. W., … Traynor, B. J. (2011). A Hexanucleotide Repeat Expansion in C9ORF72 Is the Cause of Chromosome 9p21-Linked ALS-FTD. *Neuron*, *72*(2), 257-268. https://doi.org/10.1016/j.neuron.2011.09.010

Rodríguez-Banqueri, A., Errasti-Murugarren, E., Bartoccioni, P., Kowalczyk, L., Perálvarez-Marín, A., Palacín, M., & Vázquez-Ibar, J. L. (2016). Stabilization of a prokaryotic LAT transporter by random mutagenesis. *Journal of General Physiology*, *147*(4), 353-368. https://doi.org/10.1085/jgp.201511510

Roessler, M. M., & Salvadori, E. (2018). Principles and applications of EPR spectroscopy in the chemical sciences. *Chemical Society Reviews*, *47*(8), 2534-2553. https://doi.org/10.1039/C6CS00565A

Rothbauer, U., Zolghadr, K., Muyldermans, S., Schepers, A., Cardoso, M. C., & Leonhardt, H. (2008). A Versatile Nanotrap for Biochemical and Functional Studies with Fluorescent Fusion Proteins. *Molecular & Cellular Proteomics*, *7*(2), 282-289. https://doi.org/10.1074/mcp.M700342-MCP200

Rubinsztein, D. C. (2006). The roles of intracellular protein-degradation pathways in neurodegeneration. *Nature*, *443*(7113), 780-786. https://doi.org/10.1038/nature05291

Rubio-Texeira, M., Van Zeebroeck, G., Voordeckers, K., & Thevelein, J. M. (2010). *Saccharomyces cerevisiae* plasma membrane nutrient sensors and their role in PKA signaling. *FEMS Yeast Research*, *10*(2), 134-149. https://doi.org/10.1111/j.1567-1364.2009.00587.x

Rudnik, S., & Damme, M. (2021). The lysosomal membrane—Export of metabolites and beyond. *The FEBS Journal*, *288*(14), 4168-4182. https://doi.org/10.1111/febs.15602

Ruivo, R., Bellenchi, G. C., Chen, X., Zifarelli, G., Sagné, C., Debacker, C., Pusch, M., Supplisson, S., & Gasnier, B. (2012). Mechanism of proton/substrate coupling in the heptahelical lysosomal transporter cystinosin. *Proceedings of the National Academy of Sciences*, *109*(5). https://doi.org/10.1073/pnas.1115581109

Saftig, P., & Klumperman, J. (2009). Lysosome biogenesis and lysosomal membrane proteins : Trafficking meets function. *Nature Reviews Molecular Cell Biology*, *10*(9), 623-635. https://doi.org/10.1038/nrm2745

Sahu, I. D., & Lorigan, G. A. (2018). Site-Directed Spin Labeling EPR for Studying Membrane Proteins. *BioMed Research International*.

Sahu, I. D., & Lorigan, G. A. (2020). Electron Paramagnetic Resonance as a Tool for Studying Membrane Proteins. *Biomolecules*, *10*(5), 763. https://doi.org/10.3390/biom10050763

Sampson, C. D. D., Fàbregas Bellavista, C., Stewart, M. J., & Mulligan, C. (2021). Thermostability-based binding assays reveal complex interplay of cation, substrate and lipid binding in the bacterial DASS transporter, VcINDY. *Biochemical Journal*, *478*(21), 3847-3867. https://doi.org/10.1042/BCJ20210061

Sancak, Y., Bar-Peled, L., Zoncu, R., Markhard, A. L., Nada, S., & Sabatini, D. M. (2010). Ragulator-Rag Complex Targets mTORC1 to the Lysosomal Surface and Is Necessary for Its Activation by Amino Acids. *Cell*, *141*(2), 290-303. https://doi.org/10.1016/j.cell.2010.02.024

Sancak, Y., Peterson, T. R., Shaul, Y. D., Lindquist, R. A., Thoreen, C. C., Bar-Peled, L., & Sabatini, D. M. (2008). The Rag GTPases Bind Raptor and Mediate Amino Acid Signaling to mTORC1. *Science*, *320*(5882), 1496-1501. https://doi.org/10.1126/science.1157535

Saxton, R. A., & Sabatini, D. M. (2017). mTOR Signaling in Growth, Metabolism, and Disease. *Cell*, *168*(6), 960-976. https://doi.org/10.1016/j.cell.2017.02.004

Scalise, M., Galluccio, M., Pochini, L., Cosco, J., Trotta, M., Rebsamen, M., Superti-Furga, G., & Indiveri, C. (2019). Insights into the transport side of the human SLC38A9 transceptor. *Biochimica et Biophysica Acta (BBA) - Biomembranes*, *1861*(9), 1558-1567. https://doi.org/10.1016/j.bbamem.2019.07.006

Schmelzle, T., & Hall, M. N. (2000). TOR, a Central Controller of Cell Growth. *Cell*, *103*(2), 253-262. https://doi.org/10.1016/S0092-8674(00)00117-3

Schröder, B., Wrocklage, C., Pan, C., Jäger, R., Kösters, B., Schäfer, H., Elsässer, H., Mann, M., & Hasilik, A. (2007). Integral and Associated Lysosomal Membrane Proteins. *Traffic*, *8*(12), 1676-1686. https://doi.org/10.1111/j.1600-0854.2007.00643.x

Schultz, L. D., Hofmann, K. J., Mylin, L. M., Montgomery, D. L., Ellis, R. W., & Hopper, J. E. (1987). Regulated overproduction of the GAL4 gene product greatly increases expression from galactose-inducible promoters on multi-copy expression vectors in yeast. *Gene*, *61*(2), 123-133. https://doi.org/10.1016/0378-1119(87)90107-7

Seddon, A. M., Curnow, P., & Booth, P. J. (2004). Membrane proteins, lipids and detergents : Not just a soap opera. *Biochimica et Biophysica Acta (BBA) - Biomembranes*, *1666*(1-2), 105-117. https://doi.org/10.1016/j.bbamem.2004.04.011

Sellier, C., Campanari, M., Julie Corbier, C., Gaucherot, A., Kolb-Cheynel, I., Oulad-Abdelghani, M., Ruffenach, F., Page, A., Ciura, S., Kabashi, E., & Charlet-Berguerand, N. (2016). Loss of C9 ORF 72 impairs autophagy and synergizes with polyQ Ataxin-2 to induce motor neuron dysfunction and cell death. *The EMBO Journal*, *35*(12), 1276-1297. https://doi.org/10.15252/embj.201593350

Settembre, C., Zoncu, R., Medina, D. L., Vetrini, F., Erdin, S., Erdin, S., Huynh, T., Ferron, M., Karsenty, G., Vellard, M. C., Facchinetti, V., Sabatini, D. M., & Ballabio, A. (2012). A lysosome-to-nucleus signalling mechanism senses and regulates the lysosome via mTOR and TFEB : Self-regulation of the lysosome via mTOR and TFEB. *The EMBO Journal*, *31*(5), 1095-1108. https://doi.org/10.1038/emboj.2012.32

Shen, K., Rogala, K. B., Chou, H.-T., Huang, R. K., Yu, Z., & Sabatini, D. M. (2019). Cryo-EM Structure of the Human FLCN-FNIP2-Rag-Ragulator Complex. *Cell*, *179*(6), 1319-1329.e8. https://doi.org/10.1016/j.cell.2019.10.036

Shimobayashi, M., & Hall, M. N. (2016). Multiple amino acid sensing inputs to mTORC1. *Cell Research*, *26*(1), 7-20. https://doi.org/10.1038/cr.2015.146

Shpakov, A. O. (2023). Allosteric Regulation of G-Protein-Coupled Receptors : From Diversity of Molecular Mechanisms to Multiple Allosteric Sites and Their Ligands. *International Journal of Molecular Sciences*, *24*(7), 6187. https://doi.org/10.3390/ijms24076187

Slager, R. E., Newton, T. L., Vlangos, C. N., Finucane, B., & Elsea, S. H. (2003). Mutations in RAI1 associated with Smith–Magenis syndrome. *Nature Genetics*, *33*(4), 466-468. https://doi.org/10.1038/ng1126

Smirnova, T. I., & Smirnov, A. I. (2015). Peptide–Membrane Interactions by Spin-Labeling EPR. In *Methods in Enzymology* (Vol. 564, p. 219-258). Elsevier. https://doi.org/10.1016/bs.mie.2015.08.018

Smith, P. K., Krohn, R. I., Hermanson, G. T., Mallia, A. K., Gartner, F. H., Provenzano, M. D., Fujimoto, E. K., Goeke, N. M., Olson, B. J., & Klenk, D. C. (1985). Measurement of protein using bicinchoninic acid. *Analytical Biochemistry*, *150*(1), 76-85. https://doi.org/10.1016/0003-2697(85)90442-7

Smith, S. M. (2011). Strategies for the Purification of Membrane Proteins. In D. Walls & S. T. Loughran (Éds.), *Protein Chromatography* (Vol. 681, p. 485-496). Humana Press. https://doi.org/10.1007/978-1-60761-913-0_29

Sonoda, Y., Cameron, A., Newstead, S., Omote, H., Moriyama, Y., Kasahara, M., Iwata, S., & Drew, D. (2010). Tricks of the trade used to accelerate high-resolution structure determination of membrane proteins. *FEBS Letters*, *584*(12), 2539-2547. https://doi.org/10.1016/j.febslet.2010.04.015

Sorkin, A., & Von Zastrow, M. (2009). Endocytosis and signalling : Intertwining molecular networks. *Nature Reviews Molecular Cell Biology*, *10*(9), 609-622. https://doi.org/10.1038/nrm2748

Soulié, S., Møller, J. V., Falson, P., & Le Maire, M. (1996). Urea Reduces the Aggregation of Membrane Proteins on Sodium Dodecyl Sulfate–Polyacrylamide Gel Electrophoresis. *Analytical Biochemistry*, *236*(2), 363-364. https://doi.org/10.1006/abio.1996.0183

Steipe, B. (2004). Consensus-Based Engineering of Protein Stability : From Intrabodies to Thermostable Enzymes. In *Methods in Enzymology* (Vol. 388, p. 176-186). Elsevier. https://doi.org/10.1016/S0076-6879(04)88016-9

Steipe, B., Schiller, B., Plückthun, A., & Steinbacher, S. (1994). Sequence Statistics Reliably Predict Stabilizing Mutations in a Protein Domain. *Journal of Molecular Biology*, *240*(3), 188-192. https://doi.org/10.1006/jmbi.1994.1434

Stoll, S., & Schweiger, A. (2006). EasySpin, a comprehensive software package for spectral simulation and analysis in EPR. *Journal of Magnetic Resonance*, *178*(1), 42-55. https://doi.org/10.1016/j.jmr.2005.08.013

Stoll, S., & Schweiger, A. (2007). EasySpin : Simulating cw ESR spectra. *ESR spectroscopy in membrane biophysics*, 299-321.

Straight, A. F., Belmont, A. S., Robinett, C. C., & Murray, A. W. (1996). GFP tagging of budding yeast chromosomes reveals that protein–protein interactions can mediate sister chromatid cohesion. *Current Biology*, *6*(12), 1599-1608. https://doi.org/10.1016/S0960-9822(02)70783-5

Su, M.-Y., Fromm, S. A., Zoncu, R., & Hurley, J. H. (2020). Structure of the C9orf72 ARF GAP complex that is haploinsufficient in ALS and FTD. *Nature*, *585*(7824), 251-255. https://doi.org/10.1038/s41586-020-2633-x

Sullivan, P. M., Zhou, X., Robins, A. M., Paushter, D. H., Kim, D., Smolka, M. B., & Hu, F. (2016). The ALS/FTLD associated protein C9orf72 associates with SMCR8 and WDR41 to regulate the autophagy-lysosome pathway. *Acta Neuropathologica Communications*, *4*(1), 51. https://doi.org/10.1186/s40478-016-0324-5

Szczesna-Skorupa, E., Ahn, K., Chen, C.-D., Doray, B., & Kemper, B. (1995). The Cytoplasmic and N-terminal Transmembrane Domains of Cytochrome P450 Contain Independent Signals for Retention in the Endoplasmic Reticulum. *Journal of Biological Chemistry*, *270*(41), 24327-24333. https://doi.org/10.1074/jbc.270.41.24327

Talaia, G., Amick, J., & Ferguson, S. M. (2021). Receptor-like role for PQLC2 amino acid transporter in the lysosomal sensing of cationic amino acids. *Proceedings of the National Academy of Sciences*, *118*(8), e2014941118. https://doi.org/10.1073/pnas.2014941118

Tang, D., Sheng, J., Xu, L., Zhan, X., Liu, J., Jiang, H., Shu, X., Liu, X., Zhang, T., Jiang, L., Zhou, C., Li, W., Cheng, W., Li, Z., Wang, K., Lu, K., Yan, C., & Qi, S. (2020). Cryo-EM structure of C9ORF72–SMCR8–WDR41 reveals the role as a GAP for Rab8a and Rab11a. *Proceedings of the National Academy of Sciences*, *117*(18), 9876-9883. https://doi.org/10.1073/pnas.2002110117

Tao, Y., Cheung, L. S., Li, S., Eom, J.-S., Chen, L.-Q., Xu, Y., Perry, K., Frommer, W. B., & Feng, L. (2015). Structure of a eukaryotic SWEET transporter in a homotrimeric complex. *Nature*, *527*(7577), 259-263. https://doi.org/10.1038/nature15391

Thevelein, J. M., & Voordeckers, K. (2009). Functioning and Evolutionary Significance of Nutrient Transceptors. *Molecular Biology and Evolution*, *26*(11), 2407-2414. https://doi.org/10.1093/molbev/msp168

Torricella, F., Pierro, A., Mileo, E., Belle, V., & Bonucci, A. (2021). Nitroxide spin labels and EPR spectroscopy : A powerful association for protein dynamics studies. *Biochimica et Biophysica Acta*

(BBA) - Proteins and Proteomics, *1869*(7), 140653. https://doi.org/10.1016/j.bbapap.2021.140653

Tsirigos, K. D., Peters, C., Shu, N., Käll, L., & Elofsson, A. (2015). The TOPCONS web server for consensus prediction of membrane protein topology and signal peptides. *Nucleic Acids Research*, *43*(W1), W401-W407. https://doi.org/10.1093/nar/gkv485

Tsun, Z.-Y., Bar-Peled, L., Chantranupong, L., Zoncu, R., Wang, T., Kim, C., Spooner, E., & Sabatini, D. M. (2013). The Folliculin Tumor Suppressor Is a GAP for the RagC/D GTPases That Signal Amino Acid Levels to mTORC1. *Molecular Cell*, *52*(4), 495-505. https://doi.org/10.1016/j.molcel.2013.09.016

Veen, S., Martin, S., Schuermans, M., & Vangheluwe, P. (2021). Polyamine Transport Assay Using Reconstituted Yeast Membranes. *BIO-PROTOCOL*, *11*(2). https://doi.org/10.21769/BioProtoc.3888

Verchère, A., Dezi, M., Broutin, I., & Picard, M. (2014). In vitro Investigation of the MexAB Efflux Pump From Pseudomonas aeruginosa. *Journal of Visualized Experiments*, *84*, 50894. https://doi.org/10.3791/50894

Wang, S., Tsun, Z.-Y., Wolfson, R. L., Shen, K., Wyant, G. A., Plovanich, M. E., Yuan, E. D., Jones, T. D., Chantranupong, L., Comb, W., Wang, T., Bar-Peled, L., Zoncu, R., Straub, C., Kim, C., Park, J., Sabatini, B. L., & Sabatini, D. M. (2015). Lysosomal amino acid transporter SLC38A9 signals arginine sufficiency to mTORC1. *Science*, *347*(6218), 188-194. https://doi.org/10.1126/science.1257132

Wang, Y., Hu, X.-J., Zou, X.-D., Wu, X.-H., Ye, Z.-Q., & Wu, Y.-D. (2015). WDSPdb : A database for WD40-repeat proteins. *Nucleic Acids Research*, *43*(D1), D339-D344. https://doi.org/10.1093/nar/gku1023

Waterhouse, A. M., Procter, J. B., Martin, D. M. A., Clamp, M., & Barton, G. J. (2009). Jalview Version 2—A multiple sequence alignment editor and analysis workbench. *Bioinformatics*, *25*(9), 1189-1191. https://doi.org/10.1093/bioinformatics/btp033

Wellen, K. E., & Thompson, C. B. (2010). Cellular Metabolic Stress : Considering How Cells Respond to Nutrient Excess. *Molecular Cell*, *40*(2), 323-332. https://doi.org/10.1016/j.molcel.2010.10.004

Wengrod, J. C., & Gardner, L. B. (2015). Cellular adaptation to nutrient deprivation : Crosstalk between the mTORC1 and eIF2α signaling pathways and implications for autophagy. *Cell Cycle*, *14*(16), 2571-2577. https://doi.org/10.1080/15384101.2015.1056947

Whicher, J. R., & MacKinnon, R. (2016). Structure of the voltage-gated K^+ channel Eag1 reveals an alternative voltage sensing mechanism. *Science*, *353*(6300), 664-669. https://doi.org/10.1126/science.aaf8070

Wiederhold, E., Gandhi, T., Permentier, H. P., Breitling, R., Poolman, B., & Slotboom, D. J. (2009). The Yeast Vacuolar Membrane Proteome. *Molecular & Cellular Proteomics*, *8*(2), 380-392. https://doi.org/10.1074/mcp.M800372-MCP200

Winkelmann, I., Matsuoka, R., Meier, P. F., Shutin, D., Zhang, C., Orellana, L., Sexton, R., Landreh, M., Robinson, C. V., Beckstein, O., & Drew, D. (2020). Structure and elevator mechanism of the mammalian sodium/proton exchanger NHE9. *The EMBO Journal*, *39*(24), 4541-4559. https://doi.org/10.15252/embj.2020105908

Wolfson, R. L., & Sabatini, D. M. (2017). The Dawn of the Age of Amino Acid Sensors for the mTORC1 Pathway. *Cell Metabolism*, *26*(2), 301-309. https://doi.org/10.1016/j.cmet.2017.07.001

Wyant, G. A., Abu-Remaileh, M., Wolfson, R. L., Chen, W. W., Freinkman, E., Danai, L. V., Vander Heiden, M. G., & Sabatini, D. M. (2017). mTORC1 Activator SLC38A9 Is Required to Efflux Essential Amino Acids from Lysosomes and Use Protein as a Nutrient. *Cell*, *171*(3), 642-654.e12. https://doi.org/10.1016/j.cell.2017.09.046

Xiong, J., & Zhu, M. X. (2016). Regulation of lysosomal ion homeostasis by channels and transporters. *Science China Life Sciences*, *59*(8), 777-791. https://doi.org/10.1007/s11427-016-5090-x

Xu, H., & Ren, D. (2015). Lysosomal Physiology. *Annual Review of Physiology*, *77*(1), 57-80. https://doi.org/10.1146/annurev-physiol-021014-071649

Yang, M., Liang, C., Swaminathan, K., Herrlinger, S., Lai, F., Shiekhattar, R., & Chen, J.-F. (2016). A C9ORF72/SMCR8-containing complex regulates ULK1 and plays a dual role in autophagy. *Science Advances*, *2*(9), e1601167. https://doi.org/10.1126/sciadv.1601167

Zhang, D., Iyer, L. M., He, F., & Aravind, L. (2012). Discovery of Novel DENN Proteins : Implications for the Evolution of Eukaryotic Intracellular Membrane Structures and Human Disease. *Frontiers in Genetics*, *3*. https://doi.org/10.3389/fgene.2012.00283

Zhang, Z., Wang, Y., Ding, Y., & Hattori, M. (2020). Structure-based engineering of anti-GFP nanobody tandems as ultra-high-affinity reagents for purification. *Scientific Reports*, *10*(1), 6239. https://doi.org/10.1038/s41598-020-62606-7

Zheng, H.-Z., Liu, H.-H., Chen, S.-X., Lu, Z.-X., Zhang, Z.-L., Pang, D.-W., Xie, Z.-X., & Shen, P. (2005). Yeast Transformation Process Studied by Fluorescence Labeling Technique. *Bioconjugate Chemistry*, *16*(2), 250-254. https://doi.org/10.1021/bc049833v

Zoncu, R., Bar-Peled, L., Efeyan, A., Wang, S., Sancak, Y., & Sabatini, D. M. (2011). mTORC1 Senses Lysosomal Amino Acids Through an Inside-Out Mechanism That Requires the Vacuolar H^+-ATPase. *Science*, *334*(6056), 678-683. https://doi.org/10.1126/science.1207056

8 RÉSUMÉ EN FRANÇAIS

Le lysosome a longtemps été considéré comme un organite statique dédié au recyclage des déchets cellulaires. Cependant, de nouvelles découvertes ont démontré le rôle du lysosome dans les voies de signalisation cellulaire médiées par la région cytosolique du lysosome. Un exemple particulier est le transporteur lysosomal d'acides aminés SLC38A9, qui est capable de détecter le contenu en acides aminés de la cellule, ce qui entraîne le recrutement de mTORC1 (mechanistic target of rapamycin complex 1) à la surface du lysosome et son activation. En outre, des études récentes ont montré qu'un autre transporteur lysosomal d'acides aminés, la PQLC2 (protéine 2 contenant des répétitions de boucles de proline-glutamine), est probablement impliqué dans une nouvelle voie de signalisation cellulaire médiée par le lysosome. PQLC2 appartient à une famille de protéines de transport membranaire caractérisées par une topologie membranaire à sept hélices et deux motifs proline-glutamine. La PQLC2 est localisée dans la membrane lysosomale des cellules de mammifères, et des études utilisant la PQLC2 recombinante exprimée dans des ovocytes de *Xenopus* ont démontré que la PQLC2 est un uniporteur qui transporte spécifiquement des acides aminés cationiques. Cependant, sa structure atomique 3D n'a pas encore été déterminée. En plus d'être un transporteur, la PQLC2 est également un récepteur membranaire. Lorsque la cellule est privée d'acides aminés cationiques, PQLC2 recrute à la surface du lysosome un complexe de trois protéines (appelé CSW) : les protéines activatrices de GTPase C9ORF72 et SMCR8, et WDR41, l'ancre entre CSW et PQLC2. La localisation lysosomique de CSW est associée à des processus cellulaires tels que l'autophagie, la biogenèse des lysosomes ou la régulation à la baisse des récepteurs de type Toll. En outre, des mutations congénitales du gène codant pour C9ORF72 sont directement associées à deux maladies neurodégénératives. Des essais de pull-down dans des extraits cellulaires ont démontré que l'interaction d'un court motif peptidique de 10 acides aminés provenant d'une boucle saillante de WDR41 (boucle WDR41-7CD) avec PQLC2 est suffisante pour le recrutement lysosomal de CSW.

Dans cette thèse, nous avons cherché à mieux comprendre la structure et le mécanisme de transport de

la PQLC2 ainsi qu'à caractériser les éléments moléculaires qui définissent l'interaction PQLC2-WDR41. Pour cela, nous avons exprimé une PQLC2 mammalienne dans la levure *Saccharomyces cerevisiae*, et établi un protocole de purification par affinité de la PQLC2 basé sur la reconnaissance spécifique d'un nanocorps anti-GFP et de la GFP fusionnée à la PQLC2. Pour assurer la stabilité de la PQLC2 purifiée par détergent, nous avons utilisé une approche de mutagenèse par consensus dans laquelle nous avons introduit des mutations spécifiques dans la séquence de la PQLC2 sans altérer son activité de transport. La microscopie électronique à coloration négative du consensus de la PQLC2 purifiée au détergent suggère un arrangement homotrimérique de ce transporteur, précédemment observé dans d'autres membres de la même famille. Enfin, nous avons exploité la spectroscopie de résonance paramagnétique électronique (RPE) pour évaluer l'interaction directe entre le consensus PQLC2 et un peptide synthétique boucle WDR41-7CD marqué avec une seule étiquette de spin nitroxyde à différentes positions. Ces expériences ont mis en évidence la spécificité de certains résidus boucle WDR41-7CD nécessaires à la liaison de la PQLC2, ainsi que le rôle des substrats de la PQLC2 dans la reconnaissance de la PQLC2/boucle WDR41-7CD.

Ainsi, nous avons amélioré la stabilité de la PQLC2 par mutagenèse basée sur le consensus, où nous avons établi un protocole d'expression et de purification aboutissant à un rendement suffisant de PQLC2 qui nous a permis d'étudier l'état d'oligomérisation et de valider l'interaction de la PQLC avec la boucle WDR41 in vitro. Les perspectives de ce projet sont de résoudre la structure 3D de la PQLC2 par cryo-microscopie électronique et de comprendre le mécanisme de transport et la régulation de la PQLC2.